

AD-A110 276

BROOKHAVEN NATIONAL LAB UPTON NY DEPT OF ENERGY AND --ETC F/6 13/2
SULFURIC ACID SPILL CHARACTERISTICS UNDER MARITIME ACCIDENT CON--ETC(U)
NOV 81 I N TANG, W T WONG, H R MUNKELWITZ MIPR-2-70099-7-75117A

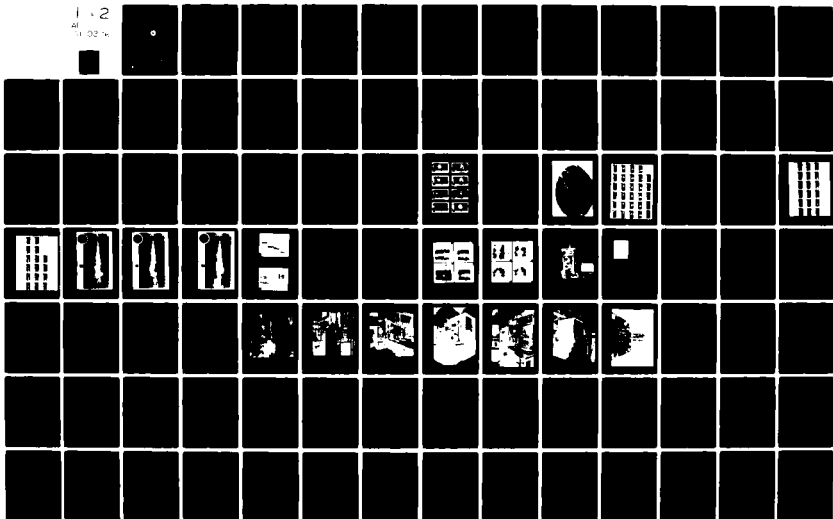
UNCLASSIFIED

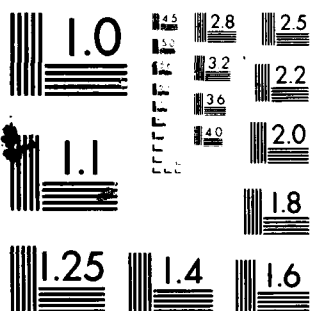
USCG-D-73-81

NL.

1 - 2

41
1 02 14





MICROCOPY RESOLUTION TEST CHART
NATIONAL BUREAU OF STANDARDS-1963-A

Report No. CG-D-73-81

LEVEL *TH*

(12)

SULFURIC ACID SPILL CHARACTERISTICS UNDER
MARITIME ACCIDENT CONDITIONS

AD A110276



FINAL REPORT

DTIC
ELECTE
S FEB 2 1982 D
A

Document is available to the public through the
National Technical Information Service,
Springfield, Virginia 22161

NOVEMBER 1981

Prepared for

DEPARTMENT OF TRANSPORTATION
UNITED STATES COAST GUARD

Office of Research and Development
Washington, D.C. 20593

FILE COPY

New
412758

82 02 01 132

NOTICE

This document is disseminated under the sponsorship of the Department of Transportation in the interest of information exchange. The United States Government assumes no liability for its contents or use thereof.

The contents of this report do not necessarily reflect the official view or policy of the Coast Guard; and they do not constitute a standard, specification, or regulation.

This report, or portions thereof may not be used for advertising or sales promotion purposes. Citation of trade names and manufacturers does not constitute endorsement or approval of such products.

Technical Report Documentation Page

1. Report No. CG-D-73-81	2. Government Accession No. AD-A110 276	3. Recipient's Catalog No.	
4. Title and Subtitle Sulfuric Acid Spill Characteristics Under Maritime Accident Conditions		5. Report Date NOVEMBER 1981	6. Performing Organization Code
		8. Performing Organization Report No.	
7. Author(s) I. N. Tang, W. T. Wang, H. R. Munkelwitz & G.S. Smith		10. Work Unit No. (TRAIS)	
9. Performing Organization Name and Address Department of Energy and Environment Brookhaven National Laboratory Upton, N.Y. 11973		11. Contract or Grant No. MIPR-2-70099-7-75117A	
		13. Type of Report and Period Covered FINAL REPORT	
12. Sponsoring Agency Name and Address U. S. Coast Guard Office of Research and Development Washington, D. C. 20593		14. Sponsoring Agency Code G-DMT-1/54	
15. Supplementary Notes Project Officer: DR. M. F. FLESSNER			
16. Abstract SULFURIC ACID SPILL CHARACTERISTICS UNDER MARITIME ACCIDENT CONDITIONS Concentrated sulfuric acid and oleum are among the most potentially hazardous chemicals routinely transported in bulk quantities on U.S. and international waterways. Conceivably, during a marine mishap, tons of sulfuric acid could abruptly be released into the water, and the consequences of such a spill accident could be detrimental to man and the environment. In the present report, several acid spill accidents are summarized. It is shown that the convective mixing of concentrated sulfuric acid with water can adequately be described by the variation of the buoyancy force arising from changes in acid concentration and released heat of dilution. Mathematic models are presented for the cases of both instantaneous and continuous releases. For oleum spills in which acid aerosol formation is a potential safety hazard, a conservative estimate of less than one-tenth of a percent is obtained for the amount of acid which might become airborne under most accident conditions. The fraction of airborne acid, however, decreases very rapidly with increasing release depth below water surfaces. The acid aerosols exhibit a well-defined log-normal particle-size distribution with peak diameter varying from 0.1 to 0.6 μ m (at 70% R.H.) depending upon release depths. This is well within the respirable particle size range.			
17. Key Words Sulfuric Acid, Marine Spill, Acid Aerosol		18. Distribution Statement Document available through National Technical Information Service, Springfield, Virginia 22161	
19. Security Classif. (of this report) Unclassified	20. Security Classif. (of this page) Unclassified	21. No. of Pages 109	22. Price

SULFURIC ACID SPILL CHARACTERISTICS UNDER
MARITIME ACCIDENT CONDITIONS

A Final Report

prepared for

United States Coast Guard
Department of Transportation

by

I.N. Tang, W.T. Wong
H.R. Munkelwitz and G.S. Smith
Department of Energy and Environment
Brookhaven National Laboratory
Upton, New York 11973

SEARCHED	
SERIALIZED	
INDEXED	
FILED	
JAN 11 1974	
FBI - NEW YORK	

A



This work was performed under the auspices of the United States Coast Guard
under Contract No. MIPR-2-70099-7-75117A.

CONTENTS

Introduction	1
Sulfuric Acid Spill Scenarios	2
Class I Accidents: Convective Mixing of Acid with Water	4
1. Instantaneous Releases	4
(i) Theoretical Considerations	4
(ii) Experimental Results and Discussions	8
2. Continuous Releases	11
(i) Theoretical Considerations	11
(ii) Experimental Results and Discussions	18
Class II Accidents: Acid Aerosol Formation	21
Conclusion	26
References	27
Appendix 1. Computer Program for Instantaneous Releases	29
Appendix 2. Photographs of the BNL Acid Spill Facility	30
Appendix 3. Evaluation of the Integrals in Eq. (15) to (18)	31
Appendix 4. Computer Program for Continuous Releases	32
Appendix 5. A Non-linear Iterative Algorithm for Inverting Diffusion Battery Data	33

INTRODUCTION

Concentrated sulfuric acid and oleum are among the most potentially hazardous chemicals routinely transported in bulk quantities on U.S. and international waterways. Although these chemicals are normally contained in cargo compartments sealed against gas and water leakage, the rupture of one or more of these compartments during a marine accident could conceivably bring about the abrupt release of tons of acid into water. The large amount of heat generated from acid-water mixing could cause both water and the absorbed sulfur trioxide in oleum to vaporize, thus forming an acid mist in the atmosphere. This acid mist would pose an immediate danger to anyone directly involved in the accident and, under adverse meteorological conditions, even threaten the safety of the nearby public as well. Furthermore, depending upon the magnitude and location of a specific spill, the water temperature and acidity could be significantly altered long enough to destroy marine life in the release vicinity.

There have been, in the past, several documented marine accidents involving sulfuric acid cargo vessels. The most recent acid spill accident, known as the case of the MT Big Mama [1], occurred at dawn on August 18, 1976. A tank barge loaded with approximately 1,060 tons of 20% oleum capsized while being towed in the lower Chesapeake Bay. All of the cargo was lost into the Bay during a time period of 30 to 60 min. The towboat personnel later recalled that they observed a tremendous reaction under the capsized barge, which produced great quantities of steam and vapor. In fact, it was noted that the barge itself was lifted 4 feet upward in the water for an estimated 30 minutes before sinking. Fortunately, the accident took place in a remote deep-water region of the Bay and no apparent damage was reported except for a rather extensive but

localized fish kill sighted by the first Coast Guard boatcrew arriving on the scene.

In view of the potential hazard associated with a probable sulfuric acid spill, the United States Coast Guard (USCG) initiated a safety analysis program and contracted the Brookhaven National Laboratory to carry out laboratory experiments designed specifically for investigating (a) the mechanisms by which sulfuric acid aerosols may be formed from oleum spills on water, and (b) the mixing processes which take place in water within the proximity of a release source. The results of the study are reported here, together with mathematical models developed during the course of investigation for predicting acid dispersion in water. The quantitative information presented here provides a data base for USCG to set up emergency response procedures and/or make environmental impact statements in case of a sulfuric acid spill accident.

SULFURIC ACID SPILL SCENARIOS

For simplicity in describing the acid spill scenarios, the following two broad classes of accidents are considered: Class I, accidents during which no appreciable amount of acid aerosols are produced and Class II, accidents in which the major safety hazards are associated with acid aerosol formation. In all cases, of course, a large amount of heat is liberated from acid-water mixing, especially during the very early stage of the spill.

Thus, the Class I accidents involve only the convective mixing of acid with water, resulting from either a quick discharge of concentrated sulfuric acid into deep water, such as might be the case of a capsized barge with all hatches blown open, or a gradual leak through a hole of finite size developed, say, in a minor collision mishap. The third possibility is the spill of an oleum cargo well underwater as in the case of the MT Big Mama described above.

In all cases, the released acid mass tends to sink quickly in water because of its high density. Vigorous turbulent mixing takes place over the advancing front, resulting in entrainment of the ambient fluid. The acid-containing region initially grows extremely fast by this entrainment process. As the volume becomes larger and the density difference smaller, the advancing speed of the acid mass as a whole slows down accordingly.

The Class II accidents include spills of oleum over water surfaces or into shallow water. The heat generated in the reaction dissipates via two different processes: raising the temperature of the mixing mass and providing latent heat for sulfur trioxide and water vaporization. The evolution of SO_3 is expected to occur only very briefly until enough water is entrained to dilute the oleum down to essentially 100% H_2SO_4 . At this point, the "free" SO_3 is all consumed and vaporization of the H_2SO_4 is unlikely because of its extremely low volatility. The initially vaporized SO_3 reacts quickly with water vapor to form sulfuric acid, which will then nucleate and grow into an acid mist. The acid mist will then be carried aloft either by the hot buoyant air or dispersed by the prevailing wind.

It should be recognized, however, that accident conditions are neither predictable nor controllable, and that the spill scenarios described above are nothing more than hypothetical cases in which each stage of an accident may be clearly defined. The purpose is to delineate the complex phenomena with several individual processes which are reasonably decoupled for the convenience of laboratory investigation over a variety of conditions. Since no accident may be regarded as being typical, the emphases are then placed on those extreme conditions whose outcomes provide a conservative estimate for most other cases.

Class I Accidents: Convective Mixing of Acid with Water

1. Instantaneous Releases

(1) Theoretical Considerations

The motion of an acid mass, suddenly released in water as the result of a spill, has some features in common with that of a thermal rising through stagnant air. In both cases, the essential driving force originates from the presence of a buoyancy source due to the density difference between the moving fluid and the ambient fluid. The physics of thermals has been studied rather extensively since the 1950s by many investigators including among others, Batchelor [2], Scorer [3], Turner [4], Csanady [5], and Tsang [6]. In the present study, the simple model of Morton et al. [7] is adapted for the case of acid-water mixing. An important modification of the model is the incorporation of an energy equation to account for the simultaneous dilution and heat generation. The released heat tends to induce further turbulence by creating temperature inhomogeneities in addition to concentration inhomogeneities arising from entrainment processes.

Consider a lump of concentrated sulfuric acid discharged instantaneously into still water. A sequence of the event is shown photographically in Fig. 1. As seen in these pictures, the boundary of the acid mass is highly irregular due to the turbulent motion both within and adjacent to the settling mass. However, an equivalent sphere, with radius $b'(t')$ which is a function of time, t' , may be defined at any instant to envelop the bulk of the acid mass. Let $x'(t')$ represent the position of the center of the sphere relative to the point of release and $u'(t')$ the mean velocity of the center. Hereafter, the primed notation refers to quantities expressed in the c.g.s. units, whereas the unprimed notation refers to dimensionless quantities to be defined as they appear.

The key assumption of the model is that the rate of entrainment is proportional to $u'(t')$. The governing equations of motion may then be written as follows:

Mass balance:

$$\frac{d}{dt'} \left(\frac{4}{3} \pi b'^3 \rho' \right) = 4 \pi b'^2 \alpha u' \rho'_w \quad (1)$$

Momentum balance:

$$\frac{d}{dt'} \left(\frac{4}{3} \pi b'^3 \rho' u' \right) = \frac{4}{3} \pi b'^3 g (\rho' - \rho'_w) \quad (2)$$

Energy balance:

$$\frac{d}{dt'} \left(\frac{4}{3} \pi b'^3 \rho' C'_p T' \right) = \frac{4}{3} \pi b'^3 \rho' \left(\frac{dy}{dt'} \right) \left(\frac{\partial \Delta H'}{\partial y} \right) \quad (3)$$

Acid balance:

$$\frac{d}{dt'} \left(\frac{4}{3} \pi b'^3 \rho' y \right) = 0 \quad (4)$$

Center-of-mass velocity:

$$\frac{dx'}{dt'} = u' \quad (5)$$

where ρ' and ρ'_w are the density of the acid sphere and ambient fluid, respectively, $y(t')$ the average H_2SO_4 mass fraction of the solution in the sphere, C'_p the specific heat at concentration y , $\Delta H'$ the heat of dilution per unit mass of the solution at concentration y , $T'(t')$ the excess temperature of the sphere over the ambient fluid, and g the gravitational constant. Eq. (1) expresses the conservation of total mass (or equivalently, the mass balance) as the acid sphere expands. Eq. (2) is the conservation of momentum. Eq. (3) is the conservation of energy. Eq. (4) is the conservation of the total H_2SO_4 content. Eq. (5) is simply the definition of the velocity, u' , at the center of the acid sphere.

It is a common practice in hydrodynamic formulations to make free use of the so-called Boussinesq approximation, namely, the density difference between the bouyant fluid and the ambient fluid is assumed negligible except in the buoyancy term. Since the initial density of the 96% sulfuric acid is 1.836 gm/cm^3 at room temperature, it can hardly be regarded as being close to the ambient water density. Thus, in the present case the Boussinesq approximation is not justifiable especially in the early stage of the motion. We have therefore retained the density of the acid mass on the left hand sides of Eqs. (1) - (4). The resulting governing equations are more complicated than would be the case if the Boussinesq approximation had been applied, because ρ is a function of y and T' and hence Eqs. (1), (3), and (4) are coupled. Clearly, the effect of finite density difference between the acid mass and ambient fluid is particularly important in the momentum and energy equations.

For the case where the acid mass is released with zero initial momentum, the initial conditions are,

$$x' = 0, u' = 0, T' = T'_0, y = y_0, b' = b'_0 \quad (6)$$

where b'_0 and y_0 are the equivalent radius and H_2SO_4 mass fraction of the starting sample, respectively. Since in all experiments the concentrated sulphuric acid is usually warmer than the ambient water temperature, T'_0 is taken to be 5°C throughout the study.

The specific heat data as a function of acid composition at 20°C were taken from Perry and Chilton [8]. Since literature data [9-11] indicate only a very small temperature dependence for the specific heat of sulfuric acid, the rather comprehensive room temperature data of Reference [8] were therefore used in the calculation:

$$C_p'(y) = \begin{cases} 1 - 0.791y & 0 \leq y \leq 0.6625 \\ 0.603 - 0.192y & 0.6625 < y \leq 0.8448 \\ 1.109 - 0.791y & 0.8448 < y \end{cases}$$

The density and heat of dilution data were computed from the empirical relationships given by Azarniouch et al. (12) as follows:

$$\frac{\rho' - \rho'_a}{\rho'_a} = \phi(\xi)f(T') - 1$$

$$-20^\circ\text{C} \leq T' \leq 80^\circ\text{C},$$

$$\text{where } \phi(\xi) = 1.0 + 3.0943\xi - 4.0834\xi^2 + 1.9032\xi^3$$

$$\xi = \frac{y}{5.444 - 4.444y}$$

$$f(T') = 1.0 - 0.000536 T'$$

and

$$\left(\frac{\partial \Delta H'}{\partial y}\right) = - (A - By + Cy^2), \text{ cal/g}$$

where $A = 492.7$, $B = 987.9$ and $C = 558.3$. Again, the effect of temperature on heat of dilution is neglected here.

To facilitate numerical integration of Eq. (1) through (5), the variables x' , b' , u' , y and T' were first grouped as follows:

$$V' = b'^3, M' = b'^3 u', W' = C_p' b'^3 T', N' = b'^3 y.$$

These were then converted into the dimensionless groups:

$$V' = V'_0 V, \quad M' = (g^{1/2} V'_0)^{7/6} M, \quad W' = (A V'_0 y_0) W,$$

$$N' = (y_0 V'_0) N, \quad x' = V'_0^{1/3} x, \quad t' = (g^{-1/2} V'_0)^{1/6} t$$

where $V'_0 = b'_0{}^3$. By changing variables accordingly, incorporating the empirical expressions for C'_p , ρ' and $\partial \Delta H' / \partial y$, and rearranging, Eq. (1) through (5) were transformed into dimensionless forms suitable for simultaneous integration.

The corresponding dimensionless differential equations are as follows:

$$\frac{dV}{dt} = 3\alpha \frac{M}{\phi f V^{1/3}} - \frac{V}{\phi f} \frac{d}{dt} (\phi f) \quad (7)$$

$$\frac{dM}{dt} = V \frac{\phi f - 1}{\phi f} - \frac{M}{\phi f} \frac{d}{dt} (\phi f) \quad (8)$$

$$\frac{dW}{dt} = -N \frac{d}{dt} \left(\frac{N}{V} \right) [1 - \lambda_1 \frac{N}{V} + \lambda_2 \left(\frac{N}{V} \right)^2] - \frac{W}{\phi f} \frac{d}{dt} (\phi f) \quad (9)$$

$$\frac{dN}{dt} = -\frac{N}{\phi f} \frac{d}{dt} (\phi f) \quad (10)$$

$$\frac{dx}{dt} = \frac{M}{V} \quad (11)$$

where $\lambda_1 = By_0/A$ and $\lambda_2 = Cy_0^2/A$.

The numerical integration of Eqs. (7) through (11) were carried out on a CDC 6600, using the fourth-order Runge-Kutta numerical algorithm. The initial conditions are:

$$V = 1, M = 0, W = \frac{C'_p(y_0)T'_0}{Ay_0}, N = 1, x = 0$$

A print-out of the computer program for instantaneous release calculations is given in Appendix 1.

(11) Experimental Results

Experiments designed to study both acid-water mixing and acid aerosol formation under simulated accident conditions were carried out in the Acid Spill Facility, which is shown schematically in Fig. 2. Basically, the apparatus

consists of a 4' x 4' x 8' stainless steel tank, equipped with various acid release devices, temperature probes, and an aerosol sampling system. One side of the tank was constructed entirely of a transparent Lexon panel for photographic purposes. A smaller 2' x 2' x 4' lucite tank was used initially in the study. Some photographs of the Acid Spill Facility are given in Appendix 2.

Several different types of acid release devices were used in the experiments. In the first series of experiments, hemispherical glass cups (shown in Fig. 3), designed to pivot about a horizontal axis fixed along its diameter, were used to study the instantaneous release of conc. sulfuric acid in water. Attached to the cup was a glass lever with a float on one end, which when placed in water together with the cup, served to stabilize the cup before inverting it. In a typical experiment, the cup was filled with a known amount of acid to the level of the ambient water. It was then rapidly inverted by a specially designed mechanical device to release the acid mass without any vertical impulse. After dumping, the cup quickly reverted to its original position, thereby eliminating the problem of post-dripping. By properly illuminating the water tank with an intense tungsten lamp, the motion of the acid mass was readily observable because of the refractive index difference between the two fluids. Shadowgraphical pictures of the settling acid mass were taken against a Scotchcal film background at various times after release by a camera equipped with an automatic shutter release and film advance device. Fig. 4 shows a series of shadowgraphs taken at various stages of mixing for a 500 g acid dump. Several selected blow-ups, shown earlier in Fig. 1, clearly indicate that the acid mass retains a reasonably spherical shape throughout the course of its motion, thus somewhat lending support to the equivalent sphere assumption used in the mathematical model.

In experiments carried out to study the dispersion of concentrated sulfuric acid (96% by wt.) in water, four different initial sample sizes spanning two orders of magnitude in weight were employed. These were 4.6, 22, 130 and 500 gm. Several runs were made for each sample size and the results from all experiments are shown in Fig. 5, in which the dimensionless frontal distance of the settling acid mass given by $(x' + b')/b'_0$ is plotted vs. the dimensionless time, $t'\sqrt{g/b'_0}$, for any given initial sample size b'_0 . It is evident from Fig. 5 that all data points gather around a single curve regardless of the initial sample size used. The solid curve in Fig. 5 represents the "best fit" results calculated from the mathematical model with $\alpha = 0.21$. Morton et al. (7) have conducted similar experiments by suddenly releasing a puff of light fluid in a stably stratified salt solution which is denser than the rising fluid. They found that the values of α lie between the limits 0.27 and 0.34, which are certainly larger than the 0.21 value obtained in the present study for the turbulent mixing of sulfuric acid and water. The difference can perhaps be attributed to the heat of dilution that is accompanying the mixing process in the present case and to the non-Boussinesq behaviour.

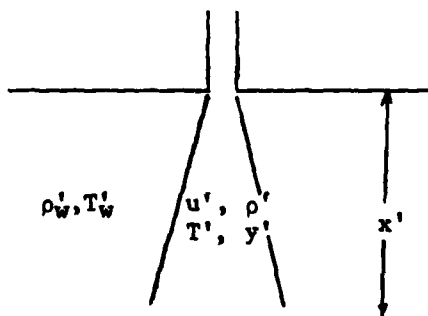
It is of interest to know how the average temperature of the acid mass varies with time. Attempts were made to measure local temperatures with fast-response (0.03 sec time resolution) miniature thermocouples placed at different locations through which the settling acid mass was expected to pass. Due to the turbulent nature of the dispersing acid mass, however, large local temperature fluctuations were observed from run to run, and it was extremely difficult to interpret the measured temperature data. Instead, the characteristic excess temperatures, T' , as a function of dimensionless time were calculated using the mathematical model, and Fig. 6 shows the results obtained with $\alpha = 0.21$. It

is seen that the excess temperature rises to a maximum very shortly after release and then decays rather rapidly with time. The calculated temperature variation with time was qualitatively confirmed with measurements. Also shown in Fig. 6 is the change in acid mass fraction as a function of dimensionless time. For example, a 100-fold dilution is expected to occur in 3.8 sec for an initial acid size of 500 gm, and 8.3 sec for a 50 kg release.

2. Continuous Releases

(1) Theoretical Considerations

The dispersion of sulphuric acid from a gradual leak through a finite size hole resulting from a minor vessel collision may be simply described in terms of existing models for an axisymmetric maintained plume in a uniform quiescent fluid. A large volume of work exists on modeling buoyant plumes and our present state of knowledge appears to be adequate in describing their behavior (for good reviews see for examples [13-15]). However, because of the high pressure head in the acid container of the vessel (as much as 1 kiloton), the acid will emerge from the hole with large momentum flux. Such a scenario is characterized by some researchers as a forced plume [16] or as a buoyant jet by others [17]. The present model will somewhat resemble Morton's formulation [16]. The general characteristics of the model are depicted schematically in the following sketch:



Underlying this model are the following assumptions:

- (1) steady-state condition prevails so that all the physical variables are functions of x' only.
- (2) ambient fluid is uniform and quiescent.
- (3) the plume is axisymmetric and turbulence is fully developed except very close to the source.
- (4) the flow is self-similar. Accordingly, the velocity profile is assumed to be Gaussian,

$$u'(x', r') = \tilde{u}(x')e^{-r'^2/b'^2} \quad (12)$$

where $b' = b'(x')$ may be regarded as the characteristic radius of the plume at x' and $\tilde{u}(x')$ is the axial velocity.

- (5) Experimental data indicate that the temperature profile is also Gaussian but with a larger lateral spread than that of velocity,

$$T'(x', r') = \tilde{T}(x')e^{-r'^2/\lambda^2 b'^2} \quad (13)$$

where T' stands for excess temperature over that of the ambient fluid and $\lambda > 1$ is an empirical constant. Similarly, the acid concentration is expected to be higher in the core of the plume than at the "outer" edge. Moreover, the temperature rise is caused by the heat generated due to acid dilution. Therefore, the acid mass fraction distribution is assumed to be Gaussian with the same lateral spread as that of the temperature profile.

$$y'(x', r') = \tilde{y}(x') e^{-r'^2/\lambda^2 b'^2} \quad (14)$$

- (6) For computational conveniences, here the Boussinesq approximation is retained, i.e. the density of the plume is assumed constant and equal to that of the ambient fluid except in the buoyancy term

$$g\Delta\rho'(x', r') = g\rho_w' P(x') e^{-r'^2/\lambda^2 b'^2} \quad (14a)$$

where $P(x') = \phi(\tilde{y})f(\tilde{T}) - 1$

- (7) Although the heat capacity of the acid is a function of y' and therefore would have a lateral spread too, it is assumed to be given by the mass fraction \tilde{y} at the axis of the plume

$$C_p(x') = C_p(\tilde{y}(x'))$$

- (8) The rate of entrainment of ambient fluid at the "edge" of the plume at any level is proportional to the axial velocity at that level. The proportionality constant, α , is independent of x' .

With these assumptions the following four conservation equations can be written

$$\text{volume: } \frac{d}{dx'} \left(\int_0^\infty 2\pi r' u' dr' \right) = 2\pi b' \alpha \tilde{u} \quad (15)$$

$$\text{momentum: } \frac{d}{dx'} \left(\int_0^\infty 2\pi r' u'^2 dr' \right) = \int_0^\infty 2\pi r' g \Delta\rho' dr' \quad (16)$$

$$\text{energy: } \frac{d}{dx'} \left(\int_0^\infty 2\pi r' u' \rho' c_p T' dr' \right) = \int_0^\infty 2\pi r' u' \rho' \left(\frac{\partial \Delta H}{\partial y'} \right) \left(\frac{\partial y'}{\partial x'} \right) dr' \quad (17)$$

$$\text{acid: } \frac{d}{dx'} \left(\int_0^\infty 2\pi r' u' \rho' y' dr' \right) = 0 \quad (18)$$

Upon evaluation of the integrals, Eqs. (15)-(18) become

$$\frac{d}{dx'} (b'^2 \tilde{u}) = 2ab' \tilde{u} \quad (19)$$

$$\frac{d}{dx'} (b'^2 \tilde{u}^2) = 2g\lambda^2 b'^2 p(x') \quad (20)$$

$$\frac{d}{dx'} (b'^2 \tilde{u} c_p \tilde{T}) = -(\lambda^2 + 1) b'^2 \tilde{u} \left[\tilde{Q}(\tilde{y}) \frac{d\tilde{y}}{dx} + \tilde{S}(\tilde{y}) \frac{2\tilde{y}}{b'} \frac{db'}{dx'} \right] \quad (21)$$

$$\frac{d}{dx'} (b'^2 \tilde{u} \tilde{y}) = 0 \quad (22)$$

The details of the derivation are given in Appendix 3.

To transform Eqs.(19)-(22) into non-dimensional forms, we need to choose the correct scales for the physical variables that govern the behavior of the plume. At the source the momentum force is expected to dominate over buoyancy force and therefore the momentum flux $M_0 = b'^2 \tilde{u}^2$ at the source is of primary importance in setting the scales. Since b' is a statistical variable, M_0 must be properly related to measurable quantities,

$$\begin{aligned} M_0 = (b'^2 \tilde{u}^2)_{x'=0} &= (\text{volumetric flow rate}) \times (\text{mean velocity}) \\ &= \frac{\text{mass flow rate}}{\text{density of fluid}} \times (\text{mean velocity}) \end{aligned}$$

For a source in the form of a circular orifice with radius R,

$$\text{mean velocity} = \frac{\text{mass flow rate}}{(\text{density})\pi R^2}$$

$$\text{Therefore,} \quad M_o = \frac{1}{\pi} \left[\frac{\text{mass flow rate}}{\text{density} \times R} \right]^2 \quad (23)$$

Then the following transformation is chosen

$$b' \tilde{u} = (M_o^{5/6} g^{-1/3}) V$$

$$b' \tilde{u}^2 = M_o M$$

$$b' \tilde{u} C_p \tilde{T} = (\gamma M_o^{5/6} g^{-1/3} C_p^*) W$$

$$b' \tilde{u} \tilde{y} = (\gamma_o M_o^{5/6} g^{-1/3}) N$$

$$x' = (M_o^{1/3} g^{-1/3}) x$$

$$b' = (M_o^{1/3} g^{-1/3}) b$$

Where $\gamma = A y_o / C_p^*$. Then, in non-dimensional form, Eqs. (19)-(22) become

$$\frac{dV}{dx} = 2\alpha M^{1/2} \quad (24)$$

$$\frac{dM}{dx} = 2\lambda \frac{V^2}{M} (\phi f - 1) \quad (25)$$

$$\frac{dW}{dx} = (\lambda^2 + 1) \frac{N}{V} \left[(Q - 2S) \frac{dV}{dx} + \frac{SV}{M} \frac{dM}{dx} \right] \quad (26)$$

$$\frac{dN}{dx} = 0 \quad (27)$$

where
$$Q\left(\frac{N}{V}\right) = \frac{1}{\lambda^2+1} - \frac{\lambda_1}{\lambda^2+2}\left(\frac{N}{V}\right) + \frac{\lambda_2}{\lambda^2+3}\left(\frac{N}{V}\right)^2$$

$$S\left(\frac{N}{V}\right) = \frac{1}{(\lambda^2+1)^2} - \frac{\lambda_1}{(\lambda^2+2)^2}\left(\frac{N}{V}\right) + \frac{\lambda_2}{(\lambda^2+3)^2}\left(\frac{N}{V}\right)^2$$

$$\lambda_1 = \frac{B}{A} y_0 \quad \text{and} \quad \lambda_2 = \frac{C}{A} y_0^2$$

It must be emphasized that Eqs. (24)-(27) are good approximations only for a fully developed free turbulent plume at a distance far from the source. Close to the source the situation is more complicated and the nature of the flow is evolving very rapidly, due to instability, from a laminar jet immediately after emergence from the source to a fully-developed self-preserving turbulent jet at some distance x_1' . To construct a model which is valid for the entire plume is difficult and besides, given the complexity of an actual acid spill, it is probably not worth the effort. Instead, the following approach is adopted. The flow is divided into two regimes: $0 \leq x' \leq x_1'$, the flow is essentially a pure jet, where momentum forces dominate and for $x' > x_1'$, it is essentially a buoyant plume, where the buoyancy force becomes dominant. The governing equations (24)-(27) are assumed to be valid for both regimes with different values of the entrainment constant α . The point of transition between these two regimes, x_1' , is somewhat uncertain. Tennekes and Lumley [18] indicated that the mean velocity profile appears to be self-preserving beyond about eight orifice diameters, although turbulence quantities are still evolving at 40 orifice diameters. Therefore, given the simplification of the present model, x_1' will be adjusted between 10 and 15 orifice diameters to yield the best fit with measurements.

Experimental data presented by Ricou and Spalding [19] indicated that the entrainment rate for a buoyant jet is somewhat larger than that for a pure jet with the same momentum. Comparison of boundary-layer theory with experiments showed that for an axisymmetric pure jet the volumetric flow rate at a distance x' from the orifice may be given by [20]

$$\text{volumetric flow rate} = 0.404 \sqrt{M_0} x' \quad (28)$$

Thus, the gradient of the volumetric flow rate is constant. This fact may be used to define an equivalent entrainment constant for a pure jet based on Taylor's entrainment assumption [7],

$$\frac{d}{dx'} (\text{volumetric flow rate}) = 2\pi \alpha \overline{b' \tilde{u}} \quad (29)$$

where $\overline{(b' \tilde{u})^2}$ is a measure of the average momentum flux. If the pure jet regime is small so that the buoyancy force has a negligible effect, $\overline{b' \tilde{u}}$ is approximately constant by virtue of the conservation of momentum. Then, comparison between Eqs. (28) and (29) implies that

$$\alpha = \frac{0.404}{2\pi} \approx 0.065 \quad (30)$$

Direct measurements of entrainment into a pure jet yielded, however, a smaller value of 0.057 for α [17,21]. Thus, the value of α will be adjusted in our model between 0.057 and 0.065 to give a best fit with measurements. For $x' > x_1'$, i.e. in the buoyancy regime, existing data showed that α lies between 0.08 and 0.12 [13,16,17,21]; the lower value corresponds to Gaussian profiles while

the higher value to "top-hat" profiles. In the present model, we again adjust α between this range to yield best fit with experimental data.

It can be readily shown from Eqn. (24)-(27) that as $x \rightarrow \infty$

$$\frac{db}{dx} \rightarrow \frac{6\alpha}{5} \quad (31)$$

which agrees with known results deduced from pure plume models [7,22]. This is intuitively expected, because far from the source the acid in the plume has been so diluted that the flow approaches the conditions of a pure plume. Thus, at large x , the plume tends to approach the shape of a circular cone subtending an angle of $2 \tan^{-1}(\frac{6\alpha}{5})$. The measurement of this angle offers a simple way to determine the entrainment constant in the buoyant regime ($x' > x_1'$).

(ii) Experimental Results

A forced plume of 96% sulphuric acid was produced from a release device constructed simply by fusing an ordinary laboratory burett to the bottom of a glass trough. The tip of the burett was placed just above the water surface in the acid spill tank. The glass trough is made as large as possible so that during the course of the experiment the head of the acid in the trough was fairly constant thereby maintaining a steady rate of acid feed. This is essential to assure steady-state condition. The mass flow rate was measured by weighing the amount of acid released in a certain period of time and was found to be about 22.2 gm/sec.

High speed photographs were taken at various instants after the acid release, again using shadowgraphic techniques. Figs. 7a and 7b show a typical set of pictures which were taken at a rate of 1 frame per second. It can be seen that at about 10 seconds after release, steady-state was reached. The

acid feed was turned off as soon as the acid front reached the bottom of the tank. Fig. 8, 9, and 10 are enlargements of the plume of the same run at 13, 21 and 29 seconds, respectively, after the release. A comparison between Fig. 9 and 10 indicates that the shape and the size of the plume were pretty stable with the bulk of the acid flow more or less confined within a circular cone.

Temperature distribution across a horizontal section of the plume was measured by placing an array of four thermocouples, equal distances apart, so that the first thermocouple was vertically below the release nozzle, i.e. on the axis of the plume, and the fourth thermocouple more or less at the "edge" of the plume. Fig. 11-1 shows the measurements with four such thermocouples placed at a distance two inches below the nozzle, showing a distinct temperature profile. Fig. 11-2 indicates that the temperature profile at nine inches from the nozzle was almost flat. Only measured plume axis temperature, T' , as a function of distance, x' , from the nozzle can be directly compared with theoretical predictions. The experimental data are summarized in Table 1.

x' (inches)	x	T' (°C)	$\tilde{T} = T' - T_w'$ ($T_w' \approx 18^\circ\text{C}$)
2	3.96	121.0	103.0
3	5.94	72.0	54.0
4	7.92	62.0	44.0
5	9.90	56.0	34.0
6	11.80	46.0	28.0
7	13.86	38.0	20.0
8	15.84	35.0	17.0
9	17.82	33.0	15.0

Table 1. Measured plume axis temperatures at various distances from the release nozzle. Column 2 lists the dimensionless distances converted from Column 1. Column 4 contains the excess temperature derived from Column 3.

With a measured mass flow rate of 22.2 g/sec, M_0 was calculated to be about $2069.5 \text{ cm}^4/\text{sec}^2$, which defines a characteristic length scale of 1.283 cm for the model. From Fig. 8, 9, and 10, the angle of the cone defined by that part of the plume far away from the source was estimated to be about $15^\circ \pm 0.5^\circ$, which would, according to Eq. 31, give a value of 0.11 ± 0.004 for the entrainment constant α in the buoyant plume regime.

The proper initial conditions for the model are at $x = 0$

$$V = 1$$

$$M = 1$$

$$W = 5/\gamma$$

$$N = 1$$

Here $\tilde{T} = 5$, since the initial acid temperature was always about 5°C warmer than the water temperature. Since Eq. (27) implies

$$N = \text{constant} = 1, \text{ for all } x,$$

the governing equations reduce to three, (24)-(26). They were solved simultaneously by the fourth order Runge-Kutta algorithm with a step size of 0.1 and

$$\alpha = \alpha_1 \quad 0 \leq x \leq x_1$$

$$\alpha = 0.11 \quad x > x_1$$

A print-out of the computer program is given in Appendix 4.

The values of α_1 and x_1 were adjusted to produce a best fit with the temperature measurements. It was found that $\alpha_1 = 0.065$ and $x_1 \approx 3.0$ (which corresponds to about 13 orifice diameters from the source) were the optimal figures. In Fig. 12, the theoretical axial excess temperature and axial acid mass fraction were plotted against x on the same graph. The overall agreement between theoretical prediction and experimental data for axial excess temperature is excellent.

With the values for the entrainment constant in both regimes established by experimental measurements, the axial acid mass fraction (as shown in Fig. 12) was predicted to drop below 5% for $x > 25$, which corresponds to a distance of about 107 orifice diameters in this case. An acid solution of this concentration would have a pH value of about 6, which for most practical considerations is only mildly acidic.

Class II Accident: Acid Aerosol Formation

The various possible mechanisms of acid aerosol formation due to an oleum spill on water have been reviewed in considerable details in the interim report (July 1978). However, the actual scenario is too complicated to be described by a single mechanism or a combination of several mechanisms. The partition of the spilled acid between the bulk water and air cannot be calculated a priori. Only some very conservative estimates could be deduced from thermodynamic considerations. Some heat of formation data for oleum are available in the literature [23,24]. From these data the partial molar heats of mixing required in the enthalpy calculations may be derived. The distribution of energy depends upon the dynamics of the mixing and vaporization processes and may be expected to vary considerably under different conditions. One can only calculate from constant enthalpy considerations, by assuming adiabatic conditions and instantaneous and uniform mixing, the amount of SO_3 vaporized, given a priori knowledge of temperature increases of the oleum which is being diluted down to 100% H_2SO_4 . The results of such calculations for 20% oleum are given in Fig. 13, where the fraction of SO_3 vaporized is plotted vs. the temperature increment. It is seen that as much as 12% of SO_3 could be released into air to form sulfuric acid aerosols, if all energy generated from dilution were channeled

into the SO_3 vaporization process only. Obviously, this represents a hypothetical upper limit; the actual fraction is more likely to be much less since most of the released heat will be consumed heating up the fluid rather than vaporizing SO_3 . Thus the actual partition coefficients have to be measured experimentally.

In a typical oleum spill experiment, the water tank was initially filled with tap water to a predetermined level and the oleum release device (as shown in Fig. 1) was suspended from the top center of the tank. The tank was then sealed against air leakage and purged with nitrogen gas. The release device in this case consisted of a fixed stainless steel spike and a long spring-loaded lucite plunger rod. A specially blown thin-bottom glass flask containing an oleum sample of known weight was capped and attached to the lower end of the plunger. When the rod was released, the flask was propelled downward with the plunger and ruptured against the spike located a fixed distance from the bottom of the flask. The level of the water in the tank with respect to the sharp point of the spike determined the depth of release, at, above, or below the surface. Thus, oleum was instantaneously released in a consistent manner at a reproducible depth.

Usually, a white cloud was observed to rise at the instant of the release. Four circulating fans, each located at one corner of the tank cover and interconnected through ducts, quickly dispersed the cloud into a dense fog which filled the whole air space above the water. Figs. 14a and 14b show the fog formation in a sequence of pictures taken immediately before and after an oleum release experiment. A solenoid valve controlled by a pressure switch was then activated to regulate the rate at which fresh water was introduced to fill the tank. The rising water level displaced a steady volume of gas through

either a membrane filter for acid aerosol collection or a diffusion battery (Fig. 15) for particle-size distribution measurements. Sulfuric acid aerosols collected on Fluoropore filters were subsequently analyzed for total sulfate by ion chromatography [25]. Fig. 16 shows the temperature variation with time at two local points in water and in air, indicating the extent of temperature rise from oleum-water reaction.

Oleum releases varying from 50 to 475 g in size and containing either 20% or 30% free SO_3 were employed. The quantities of sulfuric acid aerosols produced in these experiments were found to depend on both the sample size and release depth in water. In general, less aerosol was formed in experiments where oleum was released below the water surface than at or above the surface. While the above-surface releases always generated a large amount of both steam and acid aerosols, which quickly formed a dense fog in the air space of the spill tank, the acid aerosols produced from the below-surface releases were barely observable even with the aid of a He-Ne laser beam.

The particle-size distributions were measured with a "Collimated Holes Structures" diffusion battery, the operation details of which have been given elsewhere [26,27]. A nonlinear iterative inversion method has been developed [27] for the analysis of diffusion battery data (Appendix 5). Fig. 17 shows a composite of two particle-size distributions for the acid aerosols generated by releasing 50 gm of 20% oleum at 2.5 cm below the surface (dashed curve) and at 2.5 cm above the surface (solid curve). Both sets of data, measured at 10% relative humidity, exhibit a distinct, well-defined log-normal particle-size distribution. The particle sizes of the aerosols produced in underwater releases are usually smaller than those produced in above-surface releases. A detailed study of the effect of oleum release depth on particle size was

undertaken for 20% oleum and the results are shown in Fig. 18, where the droplet diameter of the acid aerosol is plotted as a function of normalized sample immersion depth. Here, an immersion depth is defined as the distance measured from the water surface to the center of gravity of the oleum sample at the moment of release. For the case where the center of gravity of the sample is above water surface, the immersion depth is considered to be negative by definition. The immersion depth is then divided by the sample size taken as the radius of a sphere of equivalent volume to obtain the normalized sample immersion depth, Z , plotted as the abscissa in Fig. 18. A definite decrease in particle size is noted with increasing release depth until Z reaches about 2.5. Below this depth, the particle size seems to level off at $0.14 \pm 0.03 \mu\text{m}$ in diameter. In all cases, the observed aerosol sizes (0.1 to $0.6 \mu\text{m}$) are well within the respirable size range.

Experiments were also performed to determine the extent to which sulfuric acid could become airborne in an oleum spill accident. Although such information is extremely useful in assessing the consequences of a given accident, reproducible experimental data are very difficult to obtain since the vaporization process depends strongly on the manner in which oleum is being released in water. In addition, there is no a priori information to determine how the liberated heat of dilution is to be channeled into the several processes simultaneously operating during the initial vaporization period.

An attempt was made to correlate the airborne acid fraction with release depth and initial sample size. Fig. 19 shows the results of two series of experiments with 30% oleum of two different initial sample sizes, namely $170 \pm 10\text{g}$ and $450 \pm 25\text{g}$, released at the same depth, i.e., surface release. The concentrations of the airborne sulfate as collected on filters are monitored

for the duration of the run. The concentration decay shown in Fig. 19 is typical of a stirred aerosol in a confined space where settling and plate-out are the dominant aerosol loss processes. The bar lengths of the data points represent the time duration that a filter sample is taken, which ranges from one to ten minutes. The percent sulfate airborne for each release was obtained by extrapolating the concentration to $t=0$. It is seen that for the two series of experiments, the percent sulfate airborne is almost identical within the precision of the experimental data, although the initial sample sizes differ by a factor of almost three.

Table 2 is a summary of all release data obtained for both 20% and 30% oleum. To normalize the release depth, the previously defined normalized immersion depth, Z , is again used in Table 2. Although data are somewhat scattered, a few conclusions may be drawn from the results. It seems that, for each type of oleum, there exists a limiting value to the amount of sulfuric acid aerosol that may be formed during a spill. The fractional vaporization does not depend strongly on the initial sample size, as is suggested by the data shown in Fig. 19. As a conservative estimate, therefore, one can state that no more than one-tenth of a percent of sulfuric acid may become airborne to form an acid mist under most oleum spill conditions. The fractional airborne acid decreases very rapidly from surface spills ($Z = 0$) to releases just below the water surface ($Z = 2$).

Table 2. Summary of airborne acid fractions in oleum release experiments

Release Condition			% Acid Airborne	
Release Position	Z	Av. Sample wt. gm	20% Oleum	30% Oleum
33 cm above Surface	-8	450	$1.4 - 1.6 \times 10^{-2}$	$6.0 - 6.5 \times 10^{-2}$
On Surface	0	175	$2.2 - 4.2 \times 10^{-3}$	$1.8 - 4.6 \times 10^{-2}$
		450		$1.1 - 5.1 \times 10^{-2}$
9 cm below Surface	+2	450	$2.9 - 3.8 \times 10^{-5}$	$1.2 - 2.5 \times 10^{-4}$
17 cm below Surface	+4	450	$7.1 - 8.4 \times 10^{-5}$	$1.7 - 3.6 \times 10^{-4}$

CONCLUSIONS

Two aspects of sulfuric acid spill accidents have been investigated in laboratory experiments. It is shown that the convective mixing of concentrated sulfuric acid with water can adequately be described, for both the instantaneous and continuous releases, by mathematical models taking into account the variation of the buoyancy force arising from changes in acid concentration and liberated heat of dilution. For oleum spills in which acid aerosol formation is a potential safety hazard, a conservative estimate of less than one-tenth of a percent is obtained to represent the amount of airborne acid under most accident conditions. The fraction of airborne acid, however, decreases very rapidly with increasing release depth. The acid aerosols exhibit a well-defined log-normal particle-size distribution with peak diameter varying from 0.1 to 0.6 μm (at 70% R.H.) depending upon release depths. This is well within the respirable particle size range.

ACKNOWLEDGMENTS

The authors wish to thank Dr. C. Depazo for initial work on the mathematical model. They are indebted to J.G. Davis and W.L. Kalinowski for their invaluable contributions in designing the apparatus and performing the experiments and M. Rosen for suggesting the shadowgraphic technique and taking the photographs.

REFERENCES

1. Halvorsen, F.H., Proc. Marine Safety Council, Vol. 34, No. 4, 72 (1977).
2. Batchelor, G.K., Quart. J. Roy. Met. Soc. 80, 339 (1954).
3. Scorer, R.S., J. Fluid Mech. 2, 583 (1957).
4. Turner, J.S., J. Fluid Mech. 13, 356 (1962).
5. Csanady, G.T., J. Fluid Mech. 22, 225 (1965).
6. Tsang, G., Atm. Environ. 6, 123 (1972).
7. Morton, B.R., Taylor, G.I. and Turner, J.S., Proc. Roy. Soc. London, A234, 1 (1956).
8. Perry, R.H. and Chilton, C.H., Chemical Engineers' Handbook, 5th ed. McGraw-Hill, New York (1973).
9. Bump, T.R. and Sibbitt, W.L. Ind. Eng. Chem. 47, 1665 (1955).
10. Sinha, O.P. and Puri, O.P., Chem. Phys. Lett. 32, 495 (1975).
11. Glauque, W.R., Hornung, E.W., Kinzler, J.E. and Rubin, T.R., J. Am. Chem. Soc. 82, 62 (1960).
12. Azarniouch, M.K., Bobkiewicz, A.J., Cooke, N.E. and Farkas, E.J., Can. J. Chem. Eng. 51, 590 (1973).
13. Turner, J.S., "Buoyant plumes and thermals," Ann. Rev. Fluid Mech. 1, 29 (1969).
14. Fay, J.A., "Buoyant plumes and waves," Ann. Rev. Fluid Mech. 5, 151 (1973).
15. Briggs, G.A., "Plume Rise," AEC TID-25075 (1969).
16. Morton, B.R., J. Fluid Mech. 5, 151 (1959).
17. List, E.J. and Imberger, Jorg, J. Hydraulics Div., Am. Soc. Civil Eng. 99, HY9, 1461 (1973).

18. Tennekes, H. and Lumley J.L., "A first course in turbulence," MIT Press, 1972, pp. 131.
19. Ricou F.D. and Spalding, D.B., J. Fluid Mech. 11, 21 (1961).
20. Schlichting, J., "Boundary-layer theory," McGraw-Hill, 6th edition, 1968, p. 699.
21. Davis, L.R., Shirazi, M.A., and Slegel, D.L., J. Heat Transfer., Trans. ASME, 100, 443 (1978).
22. Crapper, P.F., Tellus 29, 470 (1977).
23. Herrmann, C.V., Ind. and Eng. Chem. 33, 899 (1941).
24. Morgen, R.A., Ind. Eng. Chem. 34, 571 (1942).
25. Small, H., Stevens, T.S. and Bauman, W.C., Anal. Chem. 47, 1801 (1975).
26. Sinclair, D., Amer. Ind. Hyg. J. 33, 729 (1972).
27. Tang, I.N., Wong, W.T. and Munkelwitz, H.R., paper presented at the AIChE Symposium on Developments in Air Pollution Sampling and Analysis, Aug. 17-20, 1980, Portland, Oregon, U.S.A.

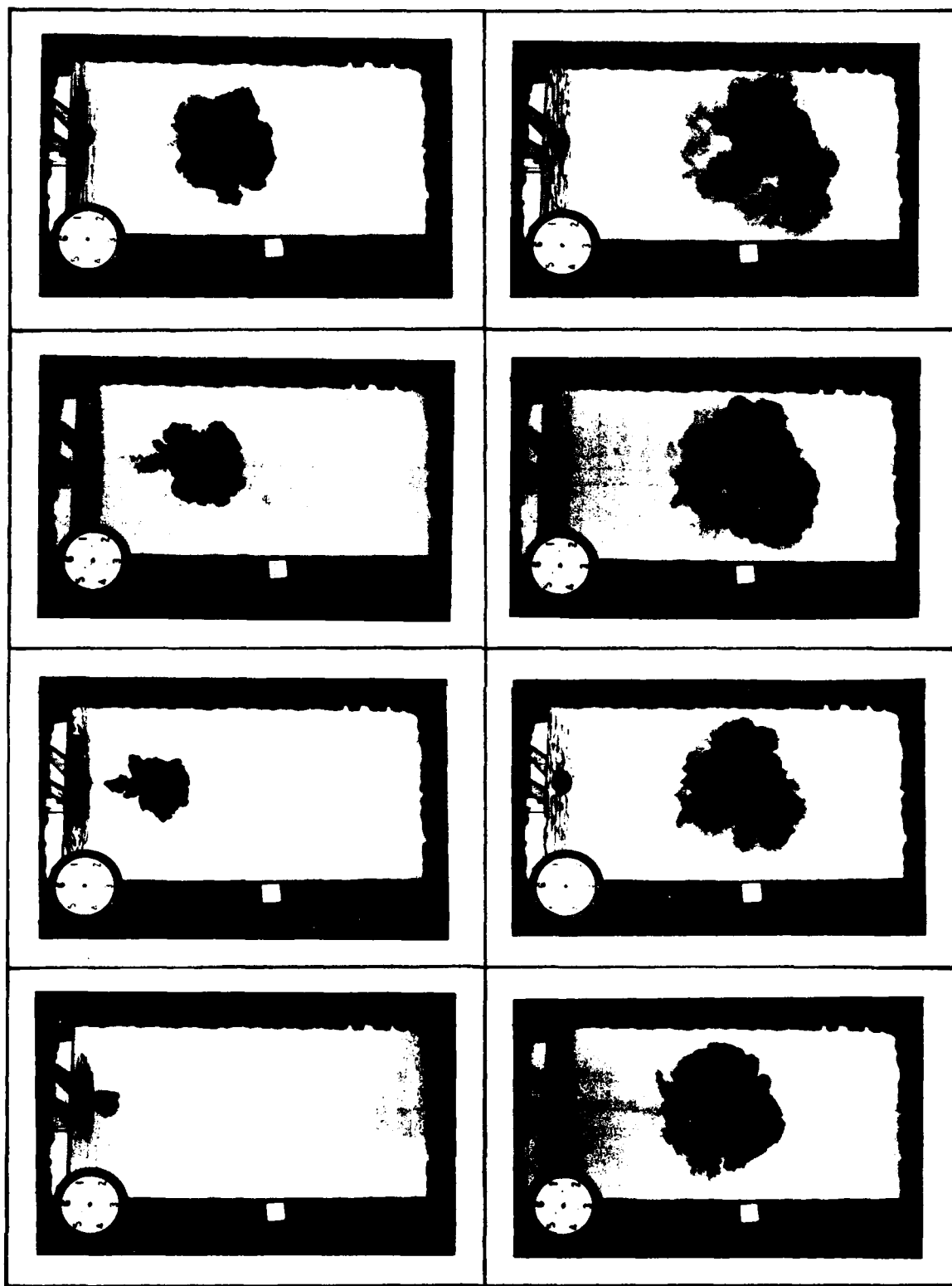


Fig. 1 Pictures of a lump of concentrated sulfuric acid instantaneously released into stagnant water and its subsequent spreading and settling as a function of time.

ACID SPILL FACILITY

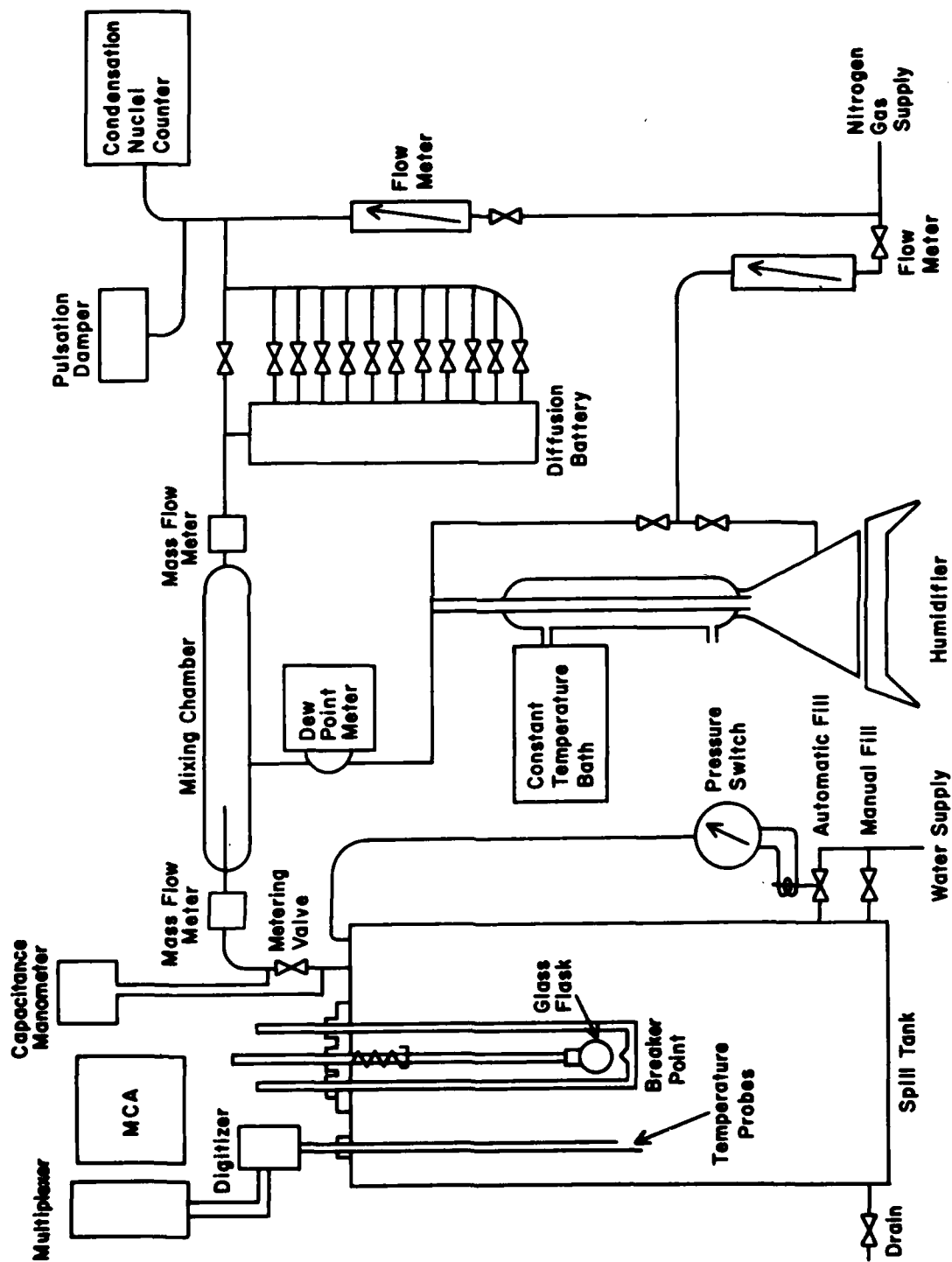


Fig. 2 Schematic diagram of BNL Acid Spill Facility

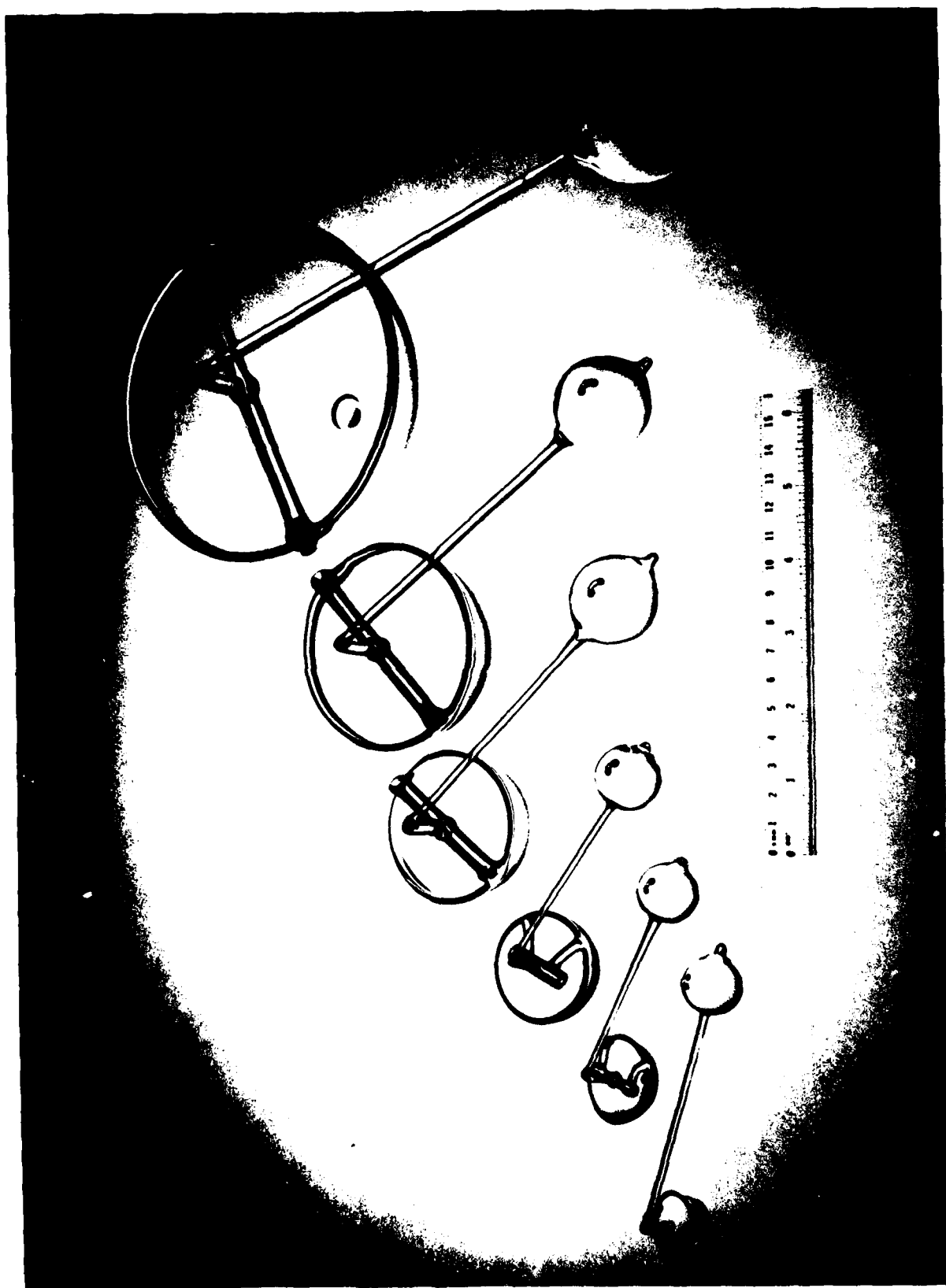
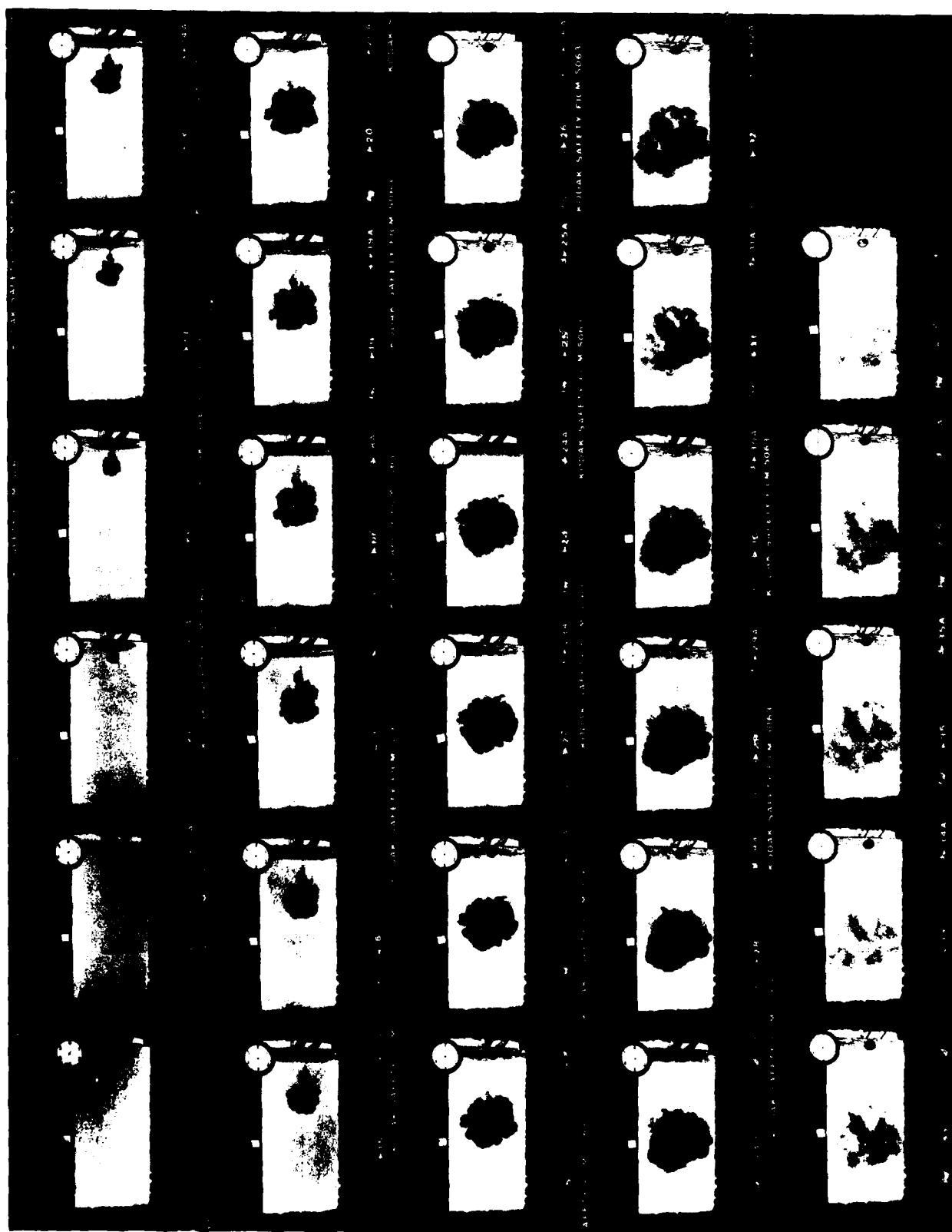


Fig. 3 Glass hemispherical cups used in acid spill experiments

Fig. 4 Shadowgraphs taken at various stages of mixing for a 500 g acid dump.



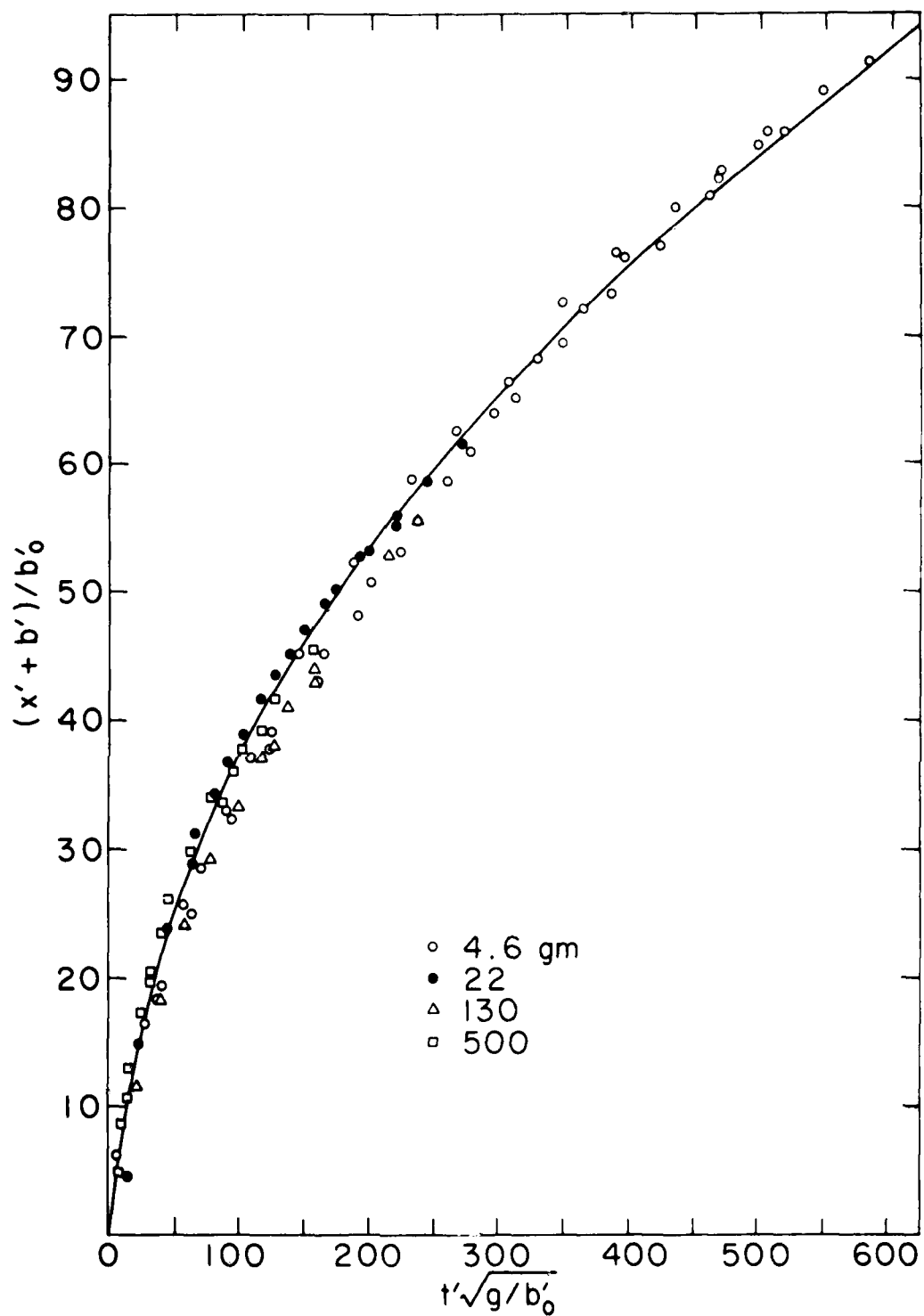


Fig. 5 Dispersion of sulfuric acid in stagnant water. The solid curve is model prediction with $\alpha=0.21$.

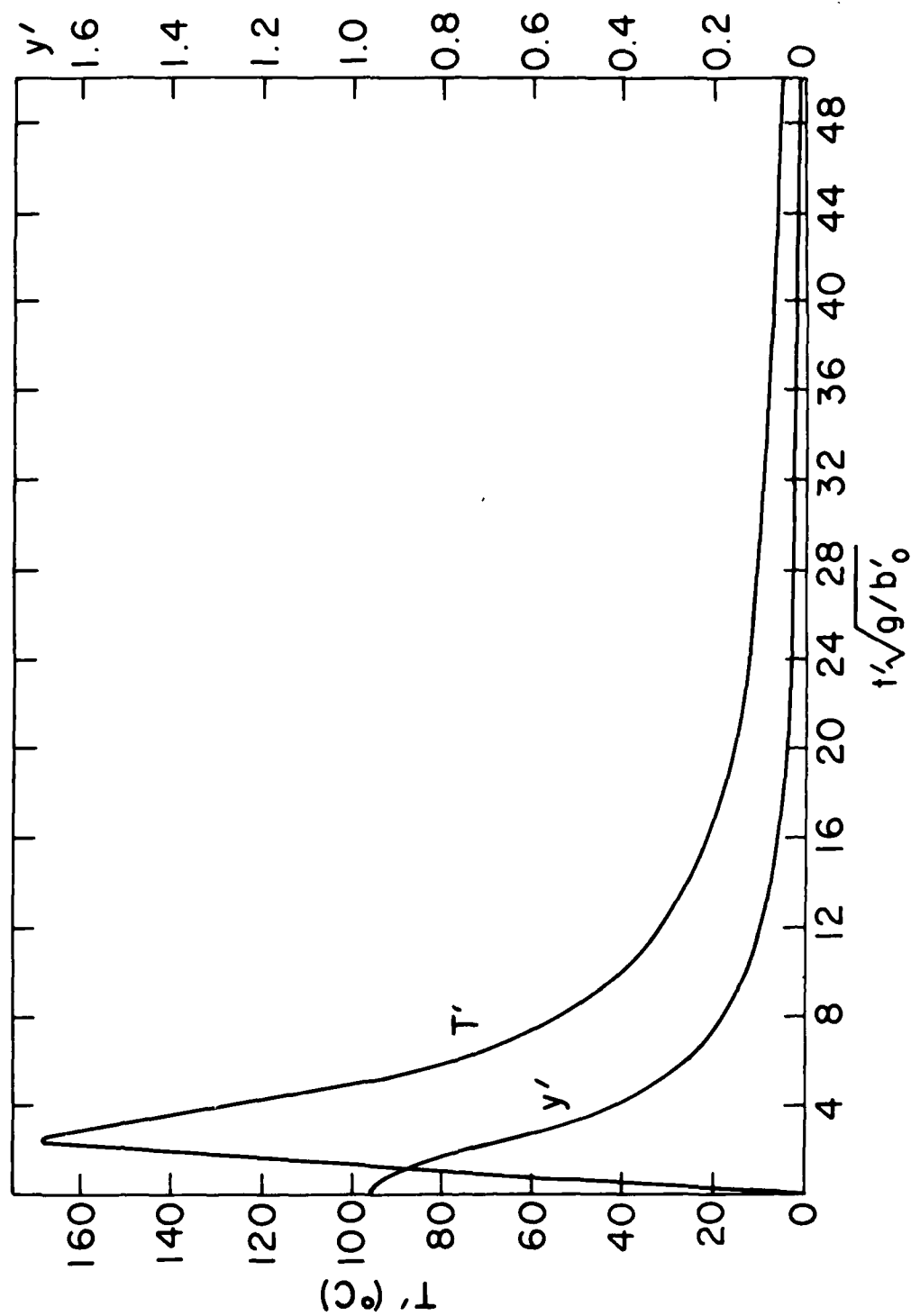


Fig. 6 Calculated temperature and acid concentration changes with time.

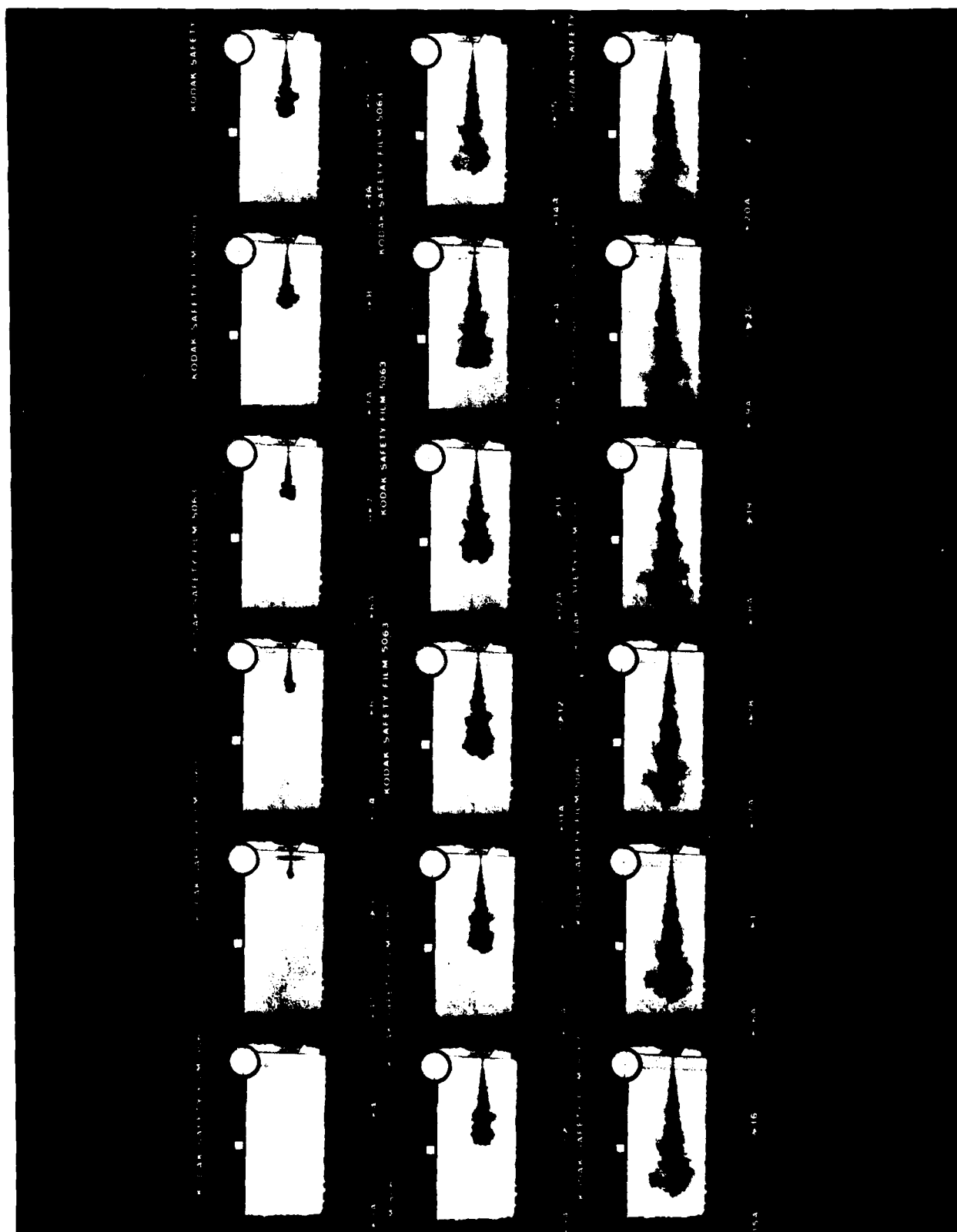


Fig. 7a Shadowgraphs of an acid plume taken at intervals of one frame per sec.

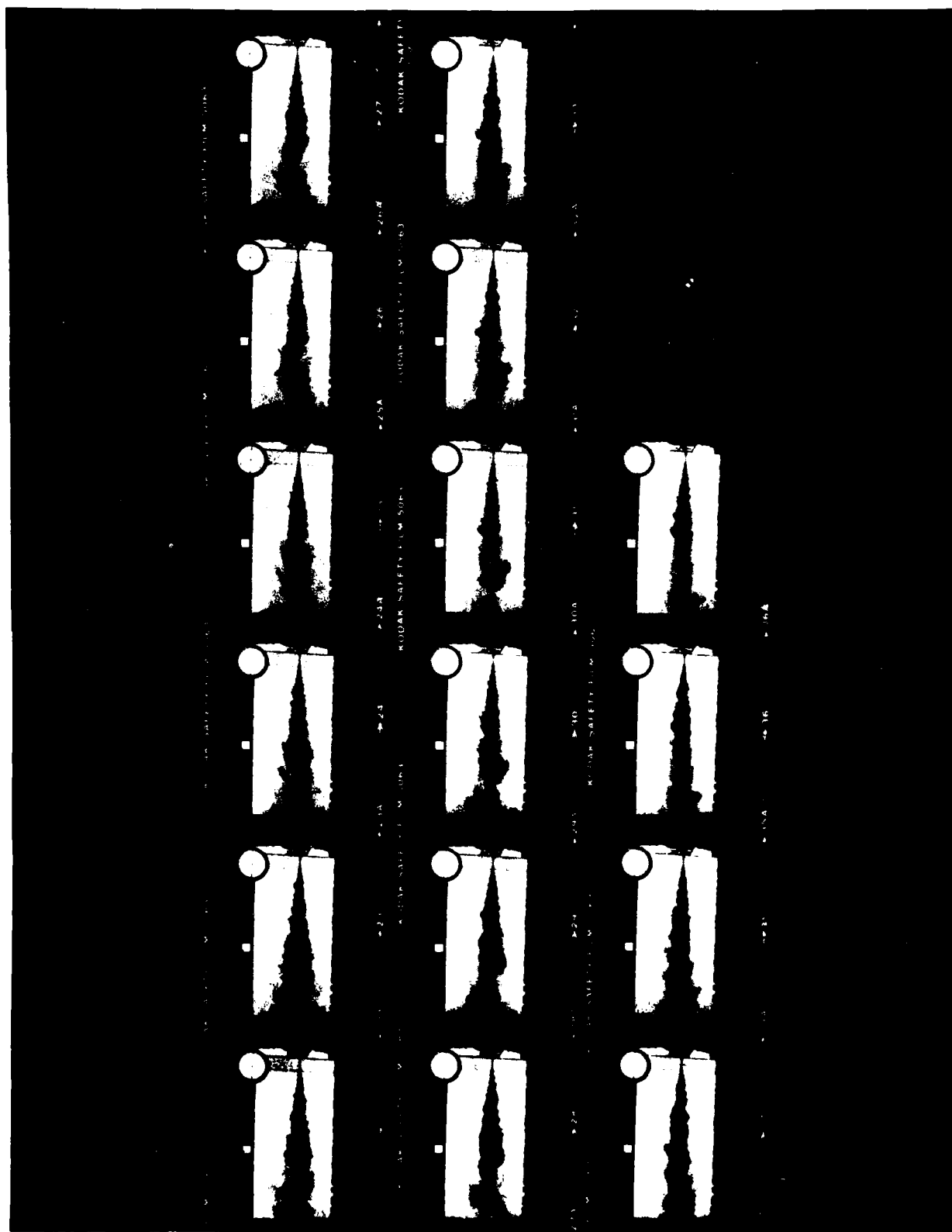


Fig. 7b Continued from Fig. 7a.



Fig. 8 Enlargement of the acid plume at 13
sec after release.

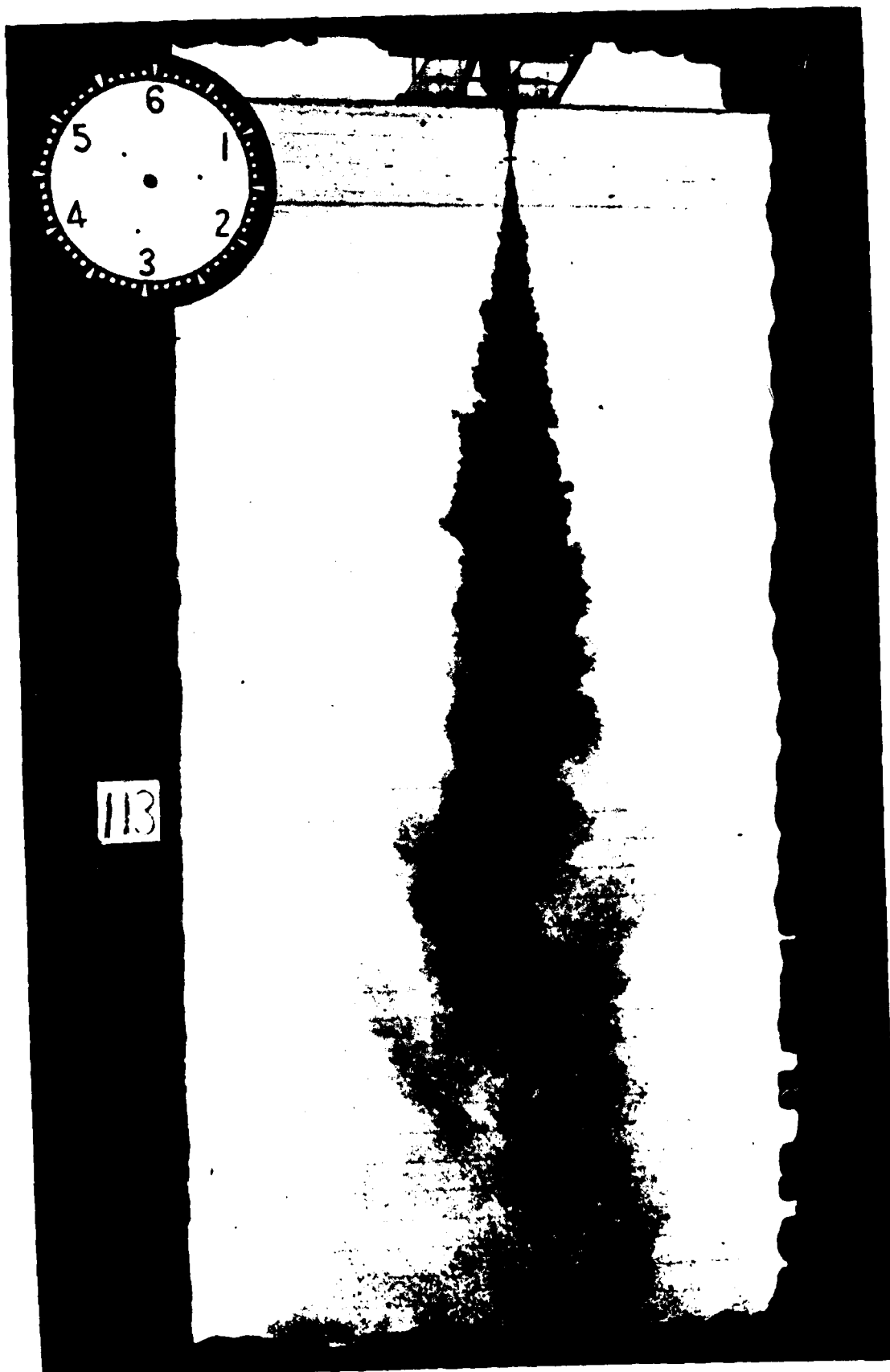


Fig. 9 Acid plume at 21 sec after release.



Fig. 10 Acid plume at 29 sec after release.

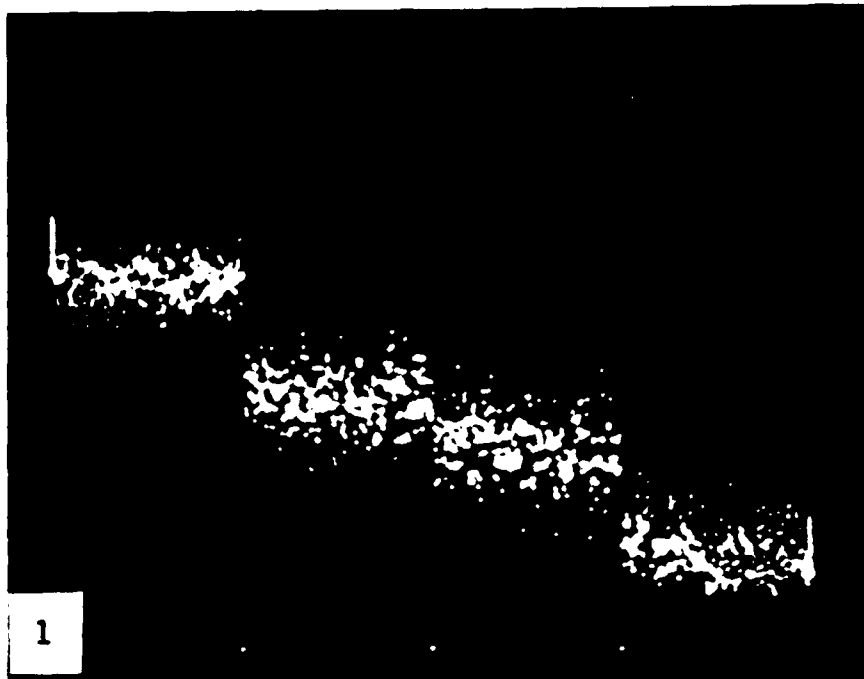
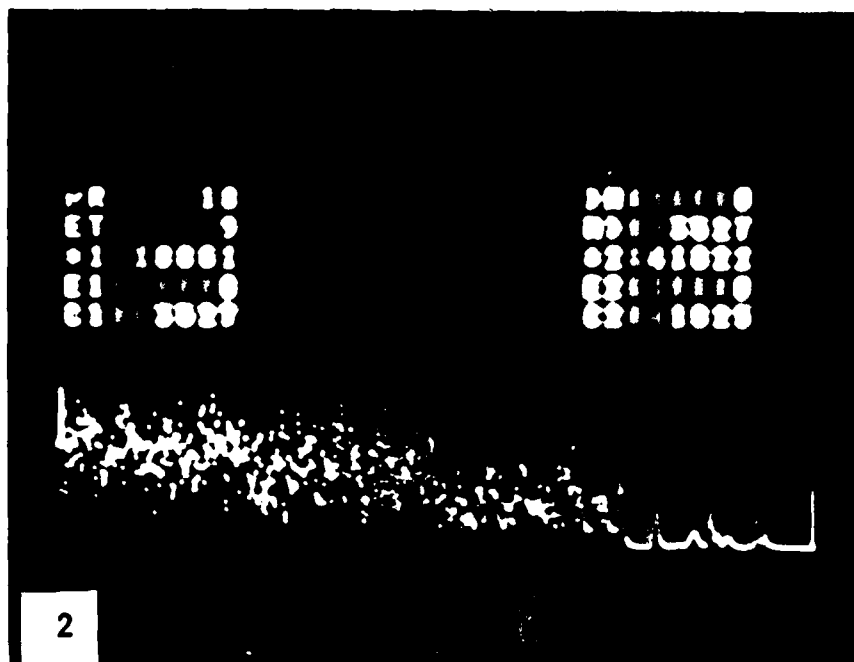


Fig. 11 Temperature measurements at four different locations inside the acid plume. The top insert was taken at 2 inches below the release nozzle; the bottom insert at 9 inches.



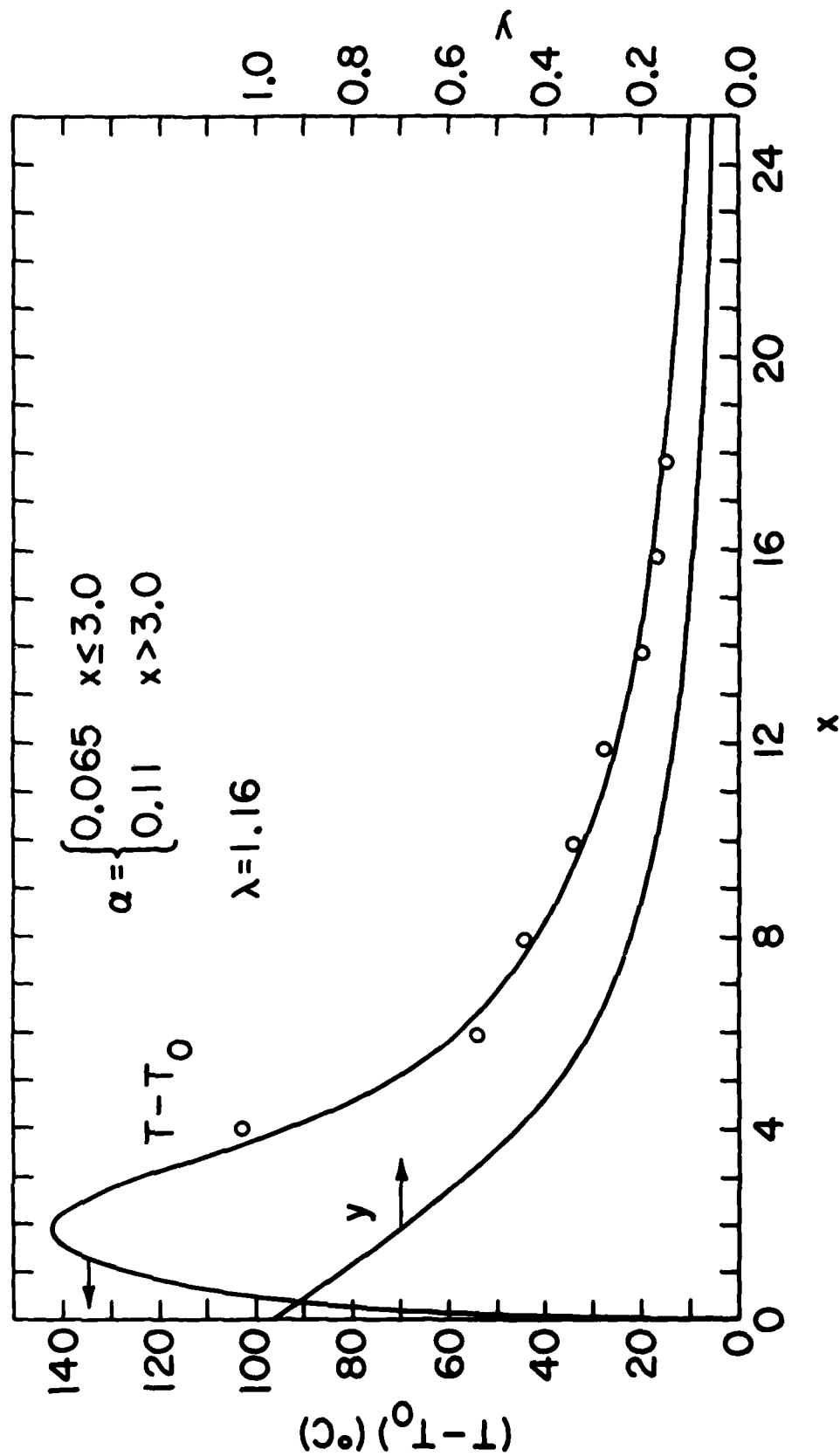


Fig. 12 A comparison of the experimental plume axis temperatures (open circles) with theoretical prediction (solid line). The computed acid concentration, y , as a function of distance is also given.

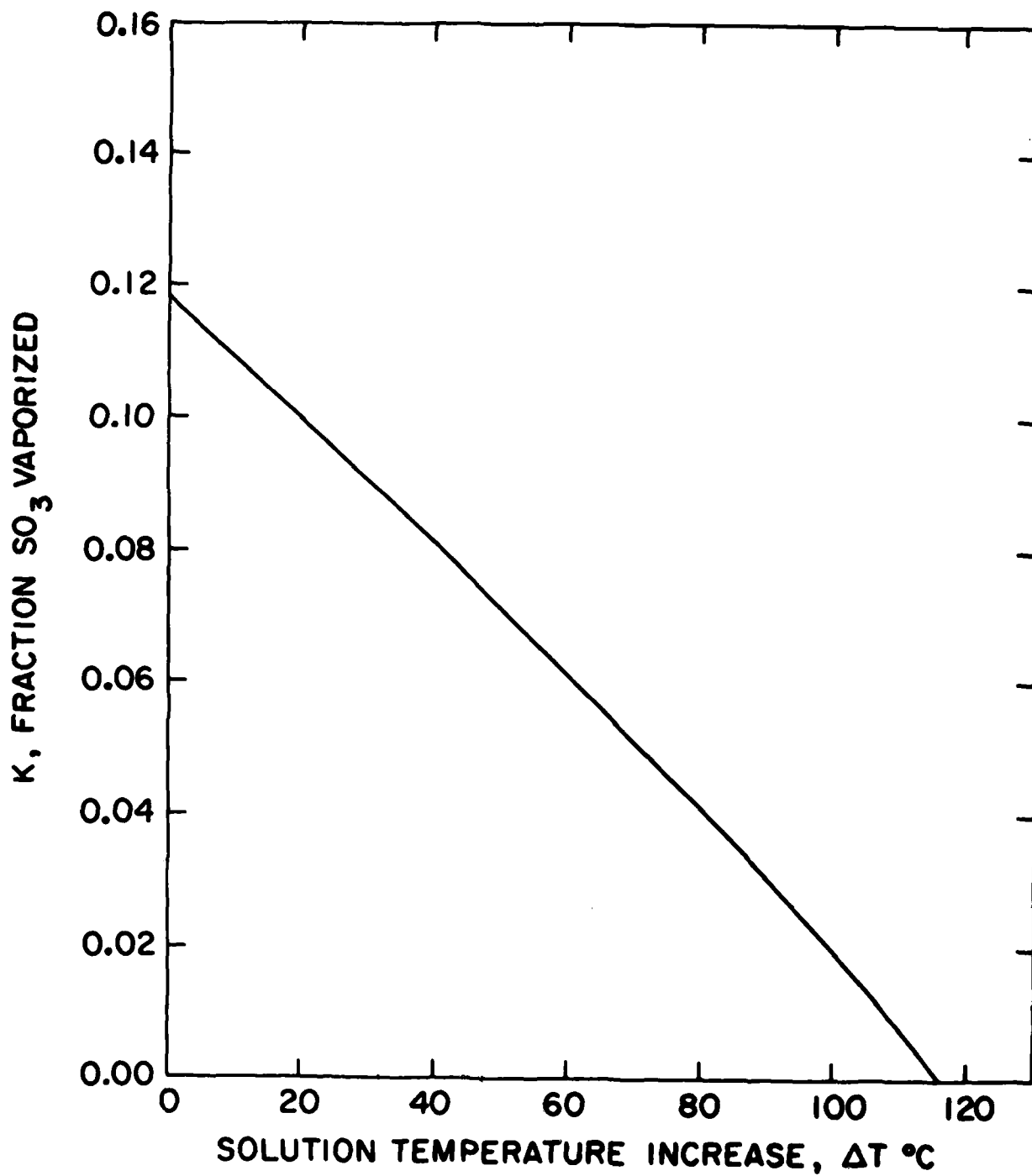


Fig. 13 Estimated fraction of SO_3 vaporized as a function of water temperature increase resulting from heat of mixing (20% oleum)

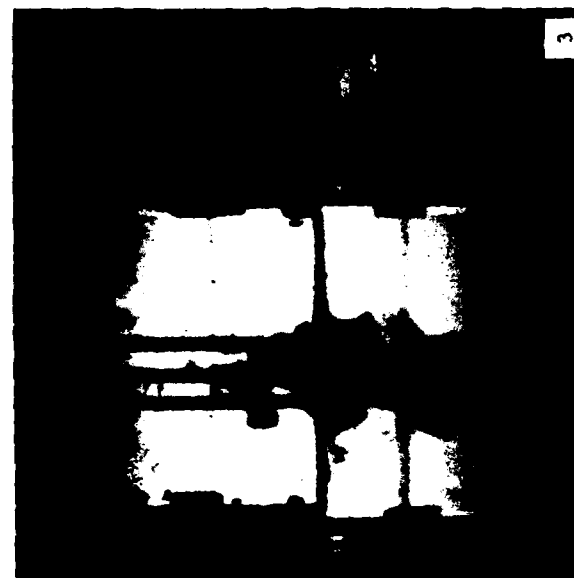
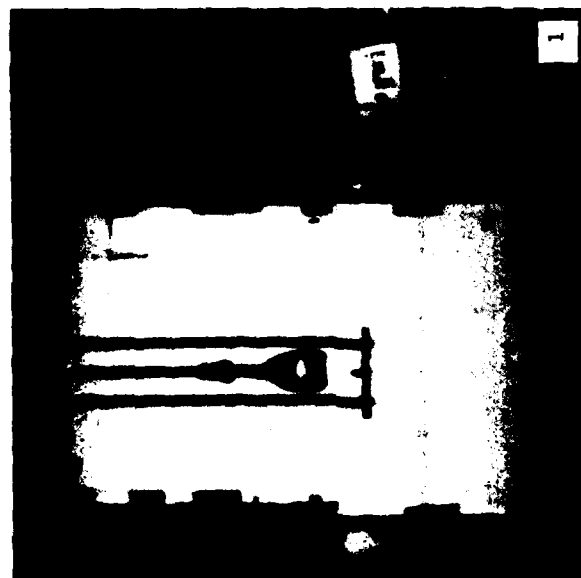
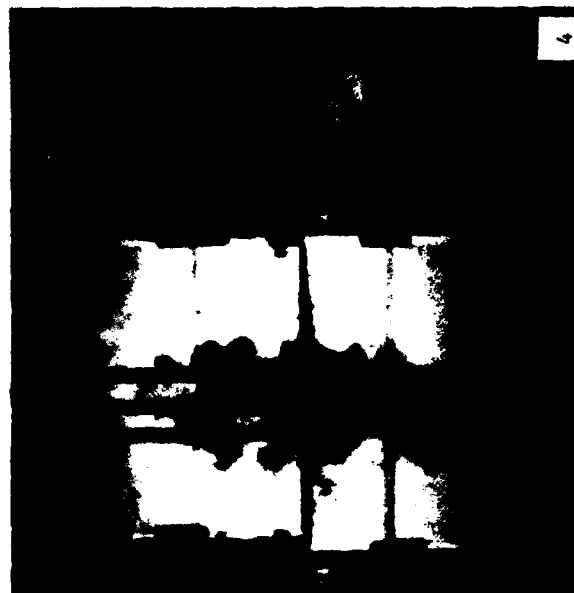
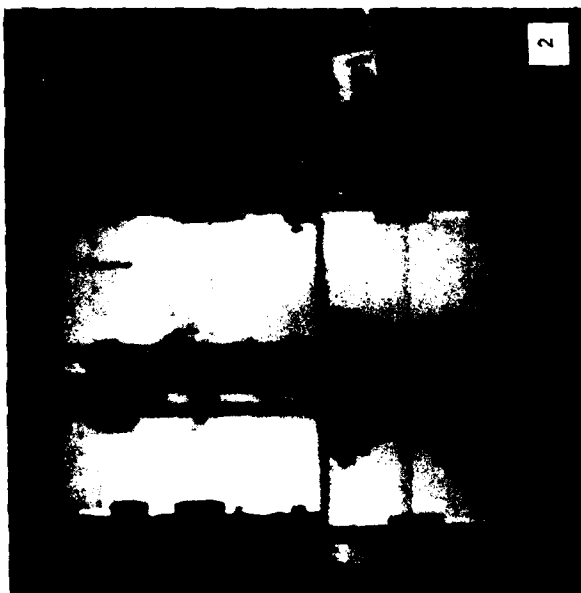


Fig. 14a Pictures taken of an oleum release experiment to show the formation of a dense fog.

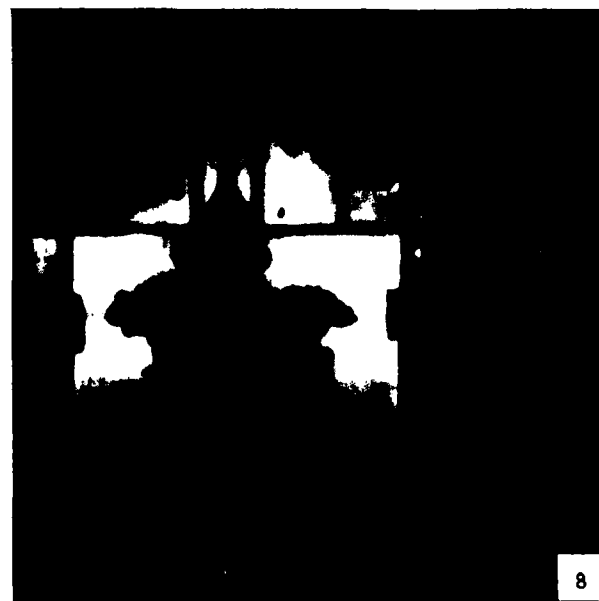
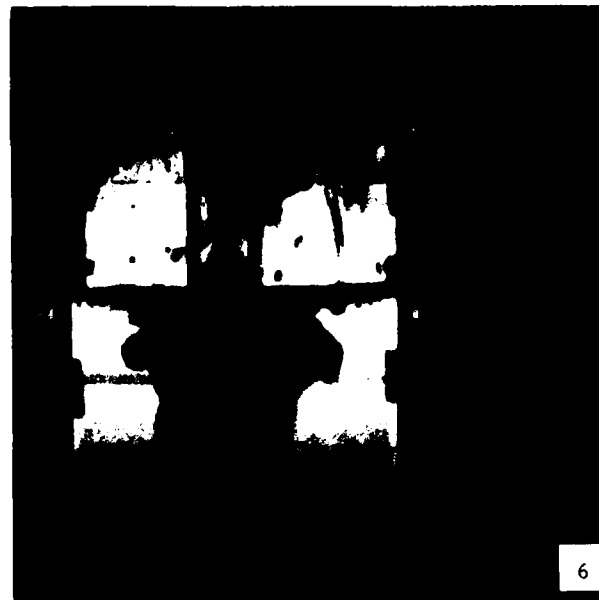


Fig. 14b continued from Fig. 14a.

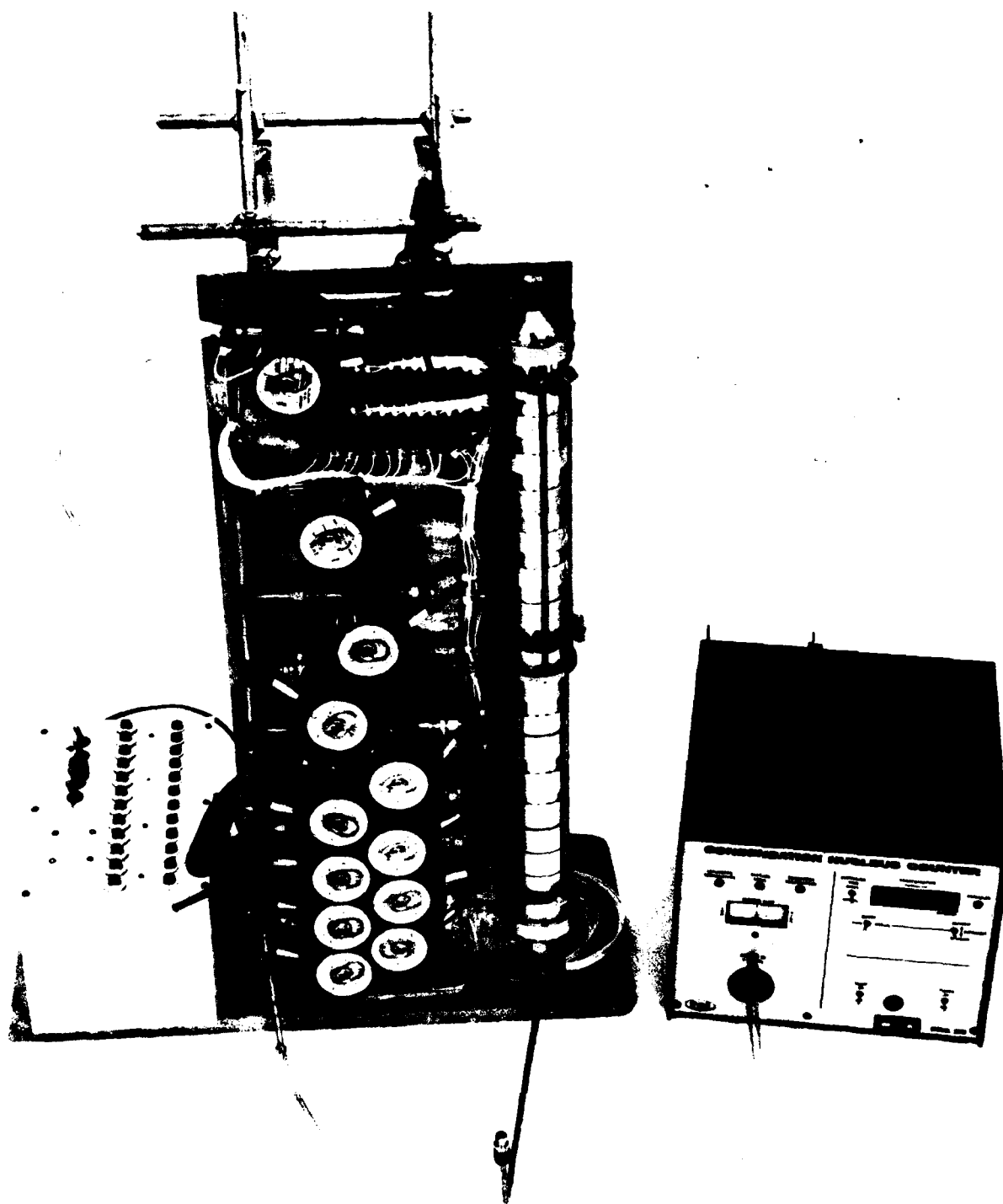


Fig. 15 Picture of the diffusion battery used in particle size measurements.

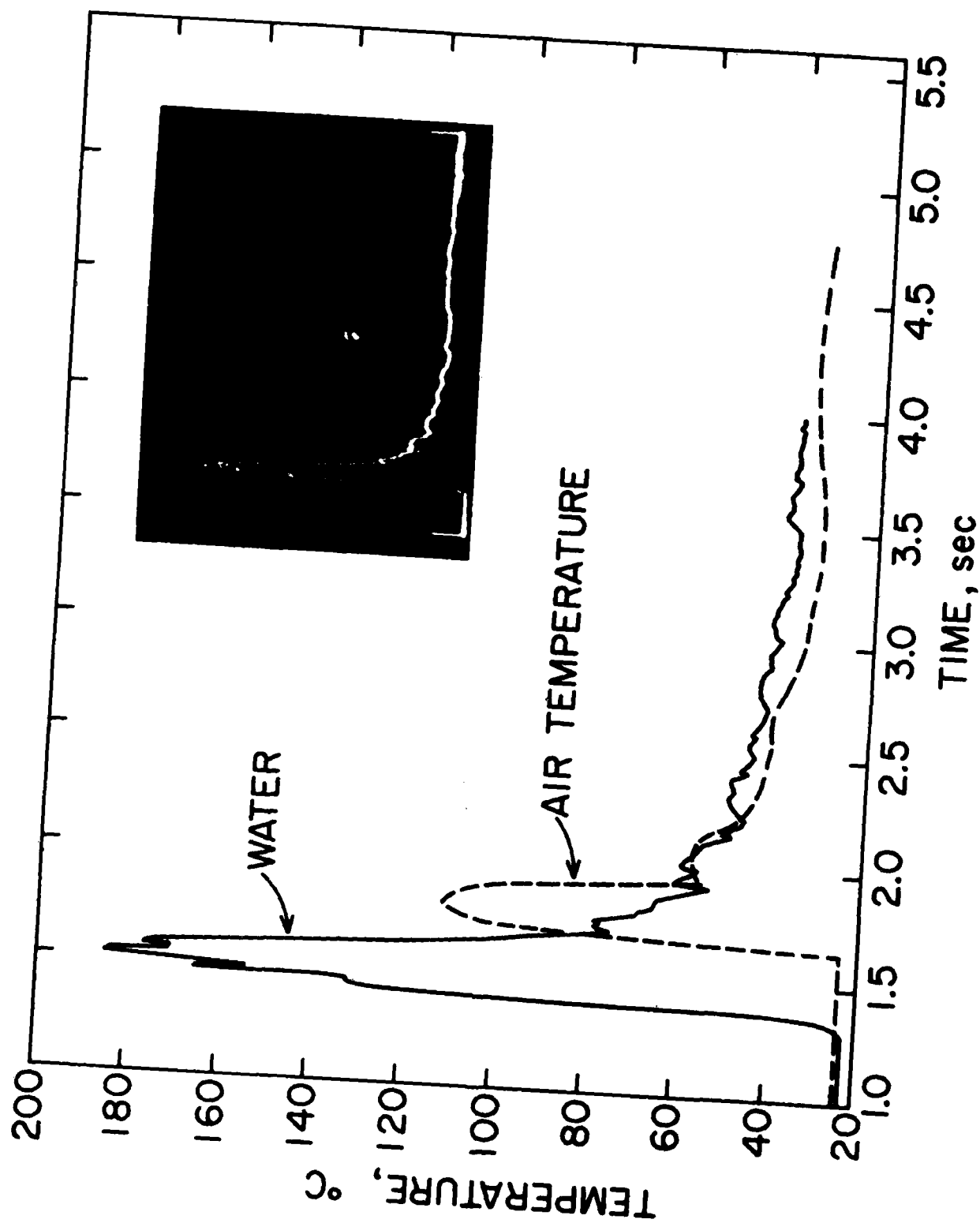


Fig. 16 Record of temperature increases for both air and water as a result of oleum-water reaction.

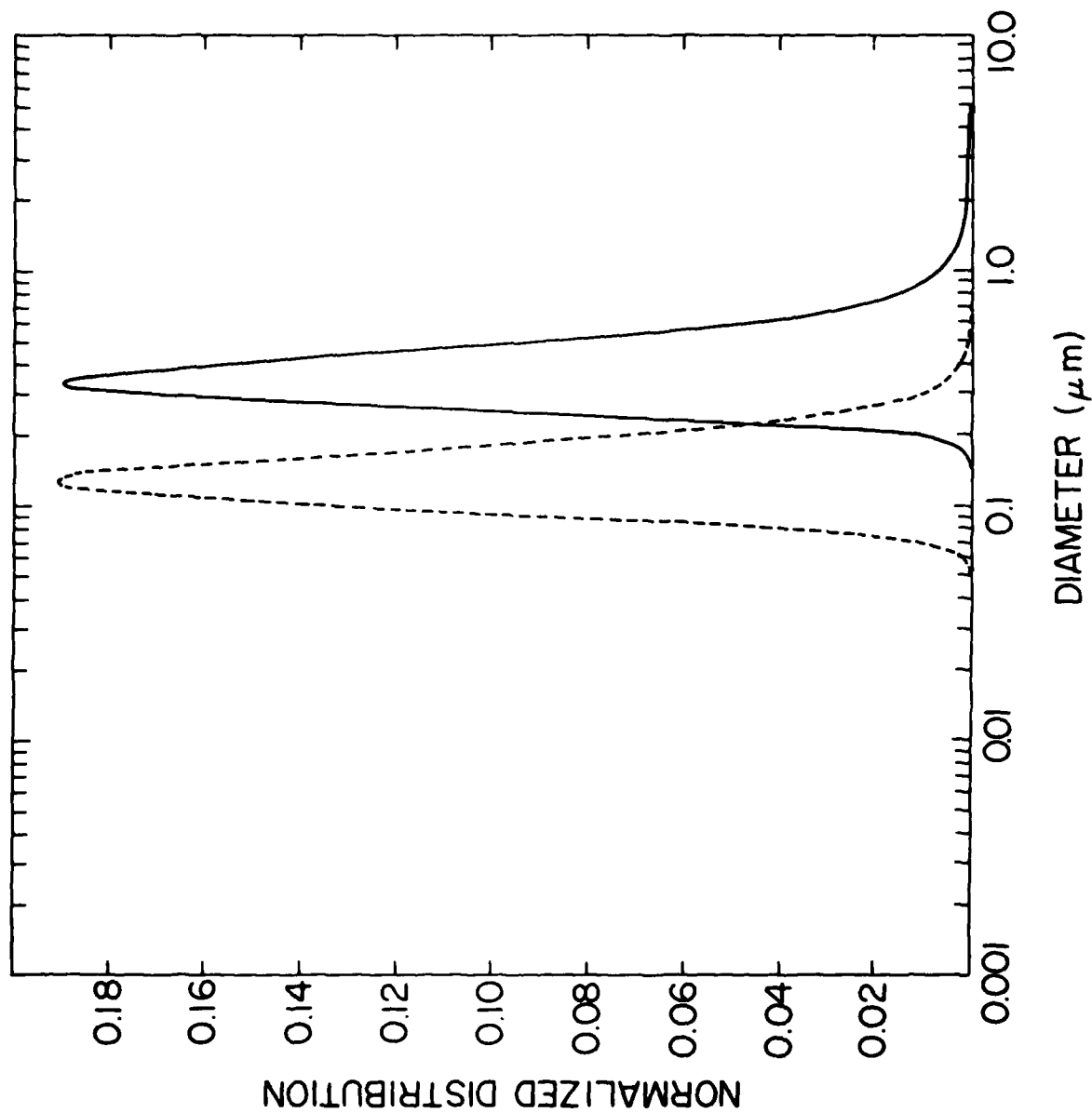


Fig. 17 Sulfuric acid aerosol size distributions measured with the diffusion battery.

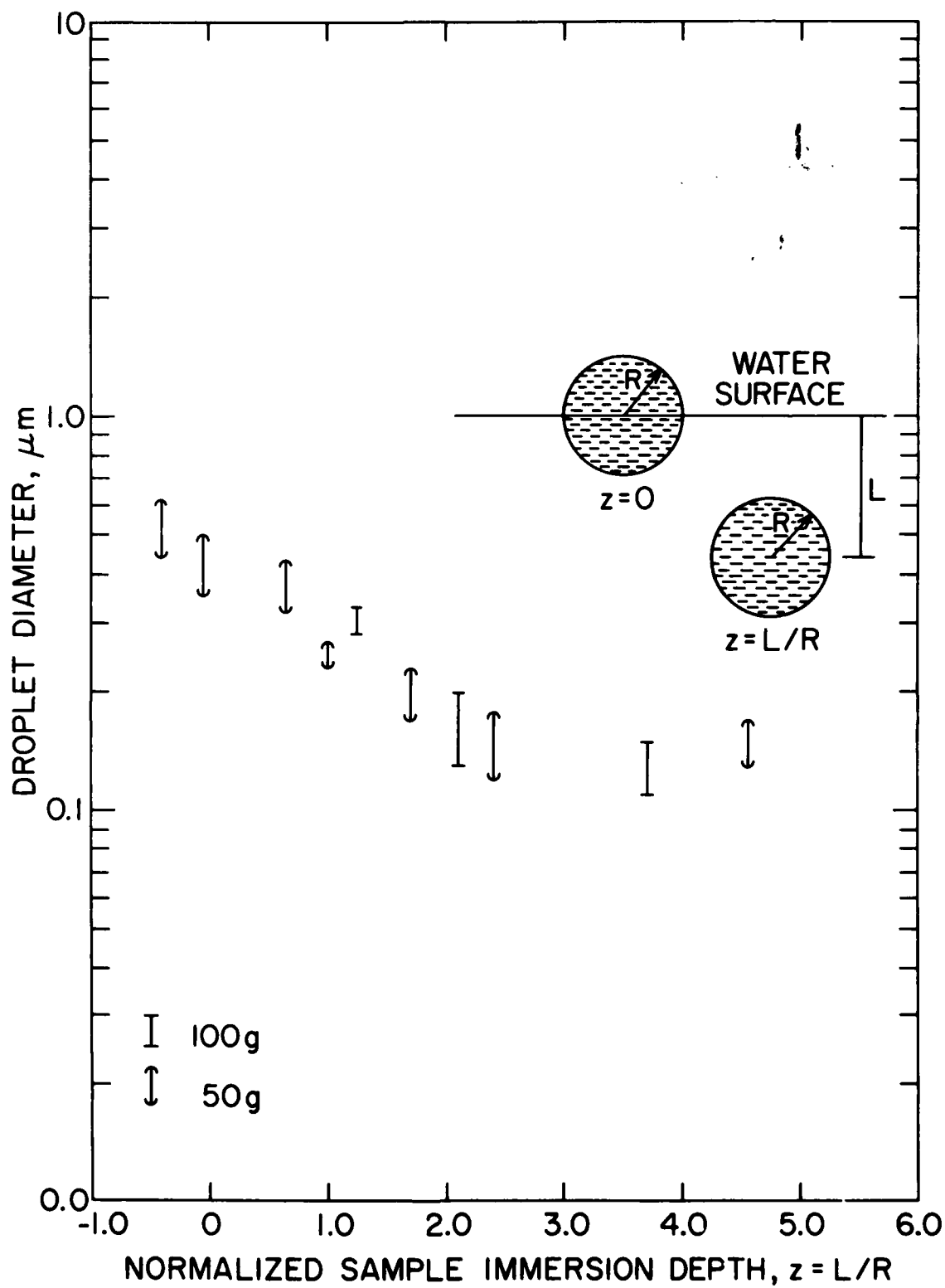


Fig. 18 Average droplet size of sulfuric acid aerosols as a function of release depth in water.

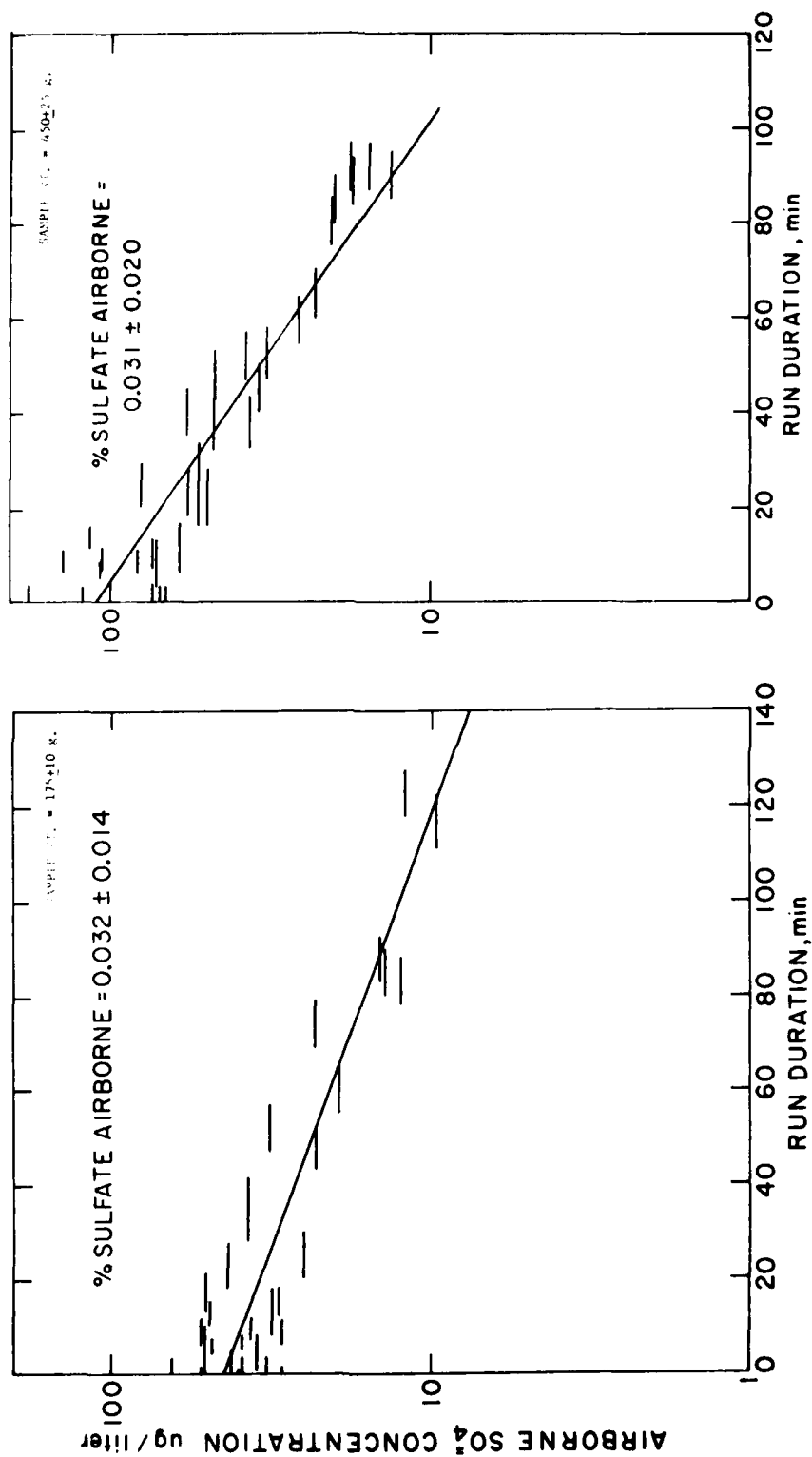


Fig. 19 Airborne sulfuric acid concentration as a function of run duration from experiments with 175 ± 10 g and 450 ± 25 g 30% oleum samples.

Appendix 1. Computer Program for Instantaneous Releases

The program solves the dimensionless governing equations for the instantaneous release of 96% H_2SO_4 in stagnant water. No input data is necessary. The output tabulates the following dimensionless quantities from the time of release up to a dimensionless time of 600: time, volume, radius, velocity, mass fraction, temperature increase ($^{\circ}C$), buoyancy, center distance, and frontal distance. A description of the FORTRAN parameters is given as follows:

FORTTRAN Parameter	Description
AK	α
CP	C_p
ETA1	η_1
SHI1	ζ_1
GA	γ
AL1	λ_1
RAD	b
VEL	u
Y	y
2HI	ξ
PHI	ϕ
F	f
TI	T
Z	An array consisting of V,M,W,N,X
DER	A subroutine to calculate the derivatives of Z

```

1      PROGRAM DIFE(OUTPUT)
      DIMENSION Z(5),ZP(5),TEMP(5,5)
      EXTERNAL DER
      COMMON GA,AL1,AL2,AK,S,ETA1,ETA2,ETA3,SHI1,SHI2
5      DATA Y0,CP,A,B,C/0.96,1.0,63.091,128.698,558.288/
      AK = 0.235
      CP = 1.109346763-0.791366907*Y0
      ETA1 = 1.0/CP
      ETA2 = 0.602620787/CP
10     ETA3 = 1.109346763/CP
      SHI1 = 0.791366907/CP
      SHI2 = 0.191549227/CP
      GA = A*Y0/CP
      AL1 = B*Y0/A
15     AL2 = C*Y0*Y0/A
      TIO = 5.0
      S = 1.0
      N = 5
      H = 0.1
20     T = 0.0
      Z(1) = 1.0
      Z(2) = 0.0
      Z(3) = TIO/GA
      Z(4) = 1.0
25     Z(5) = 0.0
      U = 0.8
      PRINT 100
100    FORMAT(1H1,1X,*TIME*,6X,*VOLUME*,9X,*RADIUS*,8X,*VELOCITY*,6X,
+ *MASS FRACT*,4X,*TEMP INCR(0C)*,4X,*BUOYANCY*,8X,*CENTER*,10X,
+ *XFRONT*/)
30     CALL DDO(T,H,N,Z,ZP,U,DER,TEMP)
50     CONTINUE
52     RAD = Z(1)**(1.0/3.0)
      VEL = Z(2)/Z(1)
35     Y = Y0*Z(4)/Z(1)
      IF(Y.LE.0.5525)GO TO 20
      IF(Y.LE.0.8448)GO TO 30
      THI = ETA3-SHI1*Y
40     GO TO 40
20     THI = ETA1-SHI1*Y
      GO TO 40
30     THI = ETA2-SHI2*Y
40     CONTINUE
      TI = GA*Z(3)/(THI*Z(1))
45     ZHI = Y/(5.44405-4.44405*Y)
      PHI = 1.0+(3.0943-4.0834*ZHI+1.9032*ZHI*ZHI)*ZHI
      F = S - 0.000535977*TI
      ACID = PHI*F*Z(4)
      BUOY = ZP(2)
50     XFRONT = Z(5) + RAD
      PRINT 101, T,Z(1),RAD,VEL,Y,TI,BUOY,Z(5),XFRONT,ACID
101    FORMAT(F6.1,8E15.6,F6.3)
      IF(T.GT.600.0)GO TO 51
      DO 10 I=1,5
55     CALL DDO(T,H,N,Z,ZP,U,DER,TEMP)
10     CONTINUE
      GO TO 52
51     CALL EXIT
      END

```

SUBROUTINE DER

74/74 OPT=1

FTN 4,5+414

```

1      SUBROUTINE DER(T,N,Z,ZP)
      DIMENSION Z(5),ZP(5)
      COMMON GA,AL1,AL2,AK,S,ETA1,ETA2,ETA3,SHI1,SHI2
      DATA Y0,CP,A,B,C/0.96,1.0,63.091,128.698,558.288/
5      Y = Z(4)/Z(1)
      YP = Y0*Y
      IF(YP.LE.0.6625)GO TO 10
      IF(YP.LE.0.8448)GO TO 20
      THI = ETA3-SHI1*YP
10     BETA = -SHI1*Y0
      GO TO 30
      10    THI = ETA1-SHI1*YP
      BETA = -SHI1*Y0
      GO TO 30
15     20    THI = ETA2-SHI2*YP
      BETA = -SHI2*Y0
      30    CONTINUE
      ZHI = Y/(5.44405/Y0-4.44405*Y)
      PHI = 1.0*(3.0943-4.0834*ZHI+1.9032*ZHI*ZHI)*ZHI
20     TEMP = GA*Z(3)/(THI*Z(1))
      Q = 0.000535977*TEMP
      F = S - Q
      Q = - Q/F
      P = 5.44405*ZHI*ZHI*(3.0943-8.1668*ZHI+5.7096*ZHI*ZHI)/(Y0*Y*Y*
25     X PHI)- BETA*Q/THI
      R = -Z(1)*(1.0-AL1*Y+AL2*Y*Y)-Z(3)*P
      ZP(1) = 3.0*AK*Z(2)/Z(1)**(1.0/3.0)
      A1 = -H/Z(1)
      B1 = 1.0*Q
30     C1 = (Z(3)*Q-Y*R)*ZP(1)/Z(1)
      A2 = 1.0*Y*P
      B2 = Z(4)*Q/Z(3)
      C2 = Y*(Q*Y*P)*ZP(1)
      DET = A1*B2-A2*B1
35     ZP(3) = (A1*C2-A2*C1)/DET
      ZP(4) = (C1*B2-C2*B1)/DET
      ZP(2) = Z(1)*(1.0-1.0/(PHI*F))-Z(2)*(P*ZP(4)/Z(1)+Q*ZP(3)/Z(3)-
      X (Q*Y*P)*ZP(1)/Z(1))
      ZP(5) = Z(2)/Z(1)
40     RETURN
      END

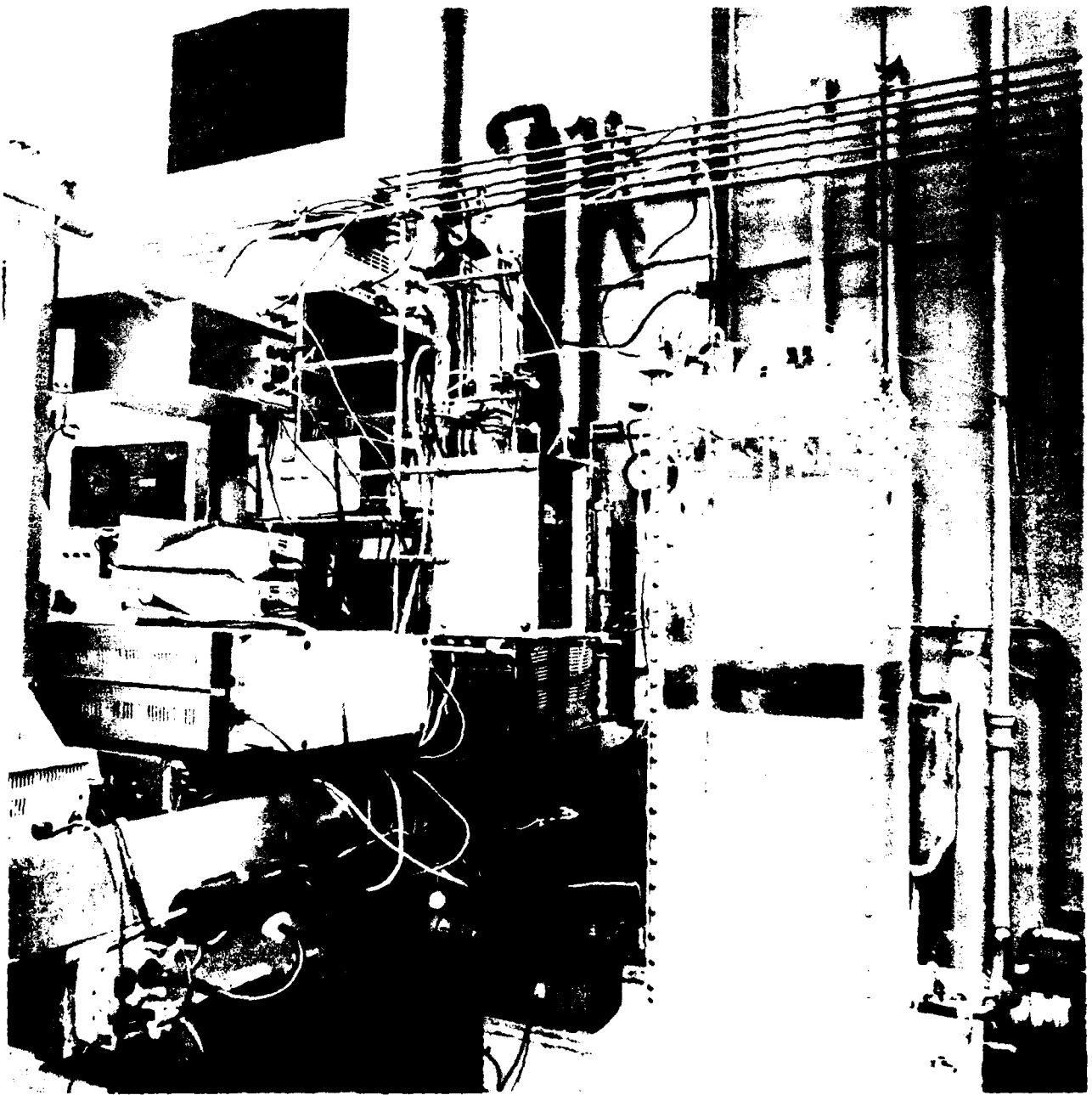
```

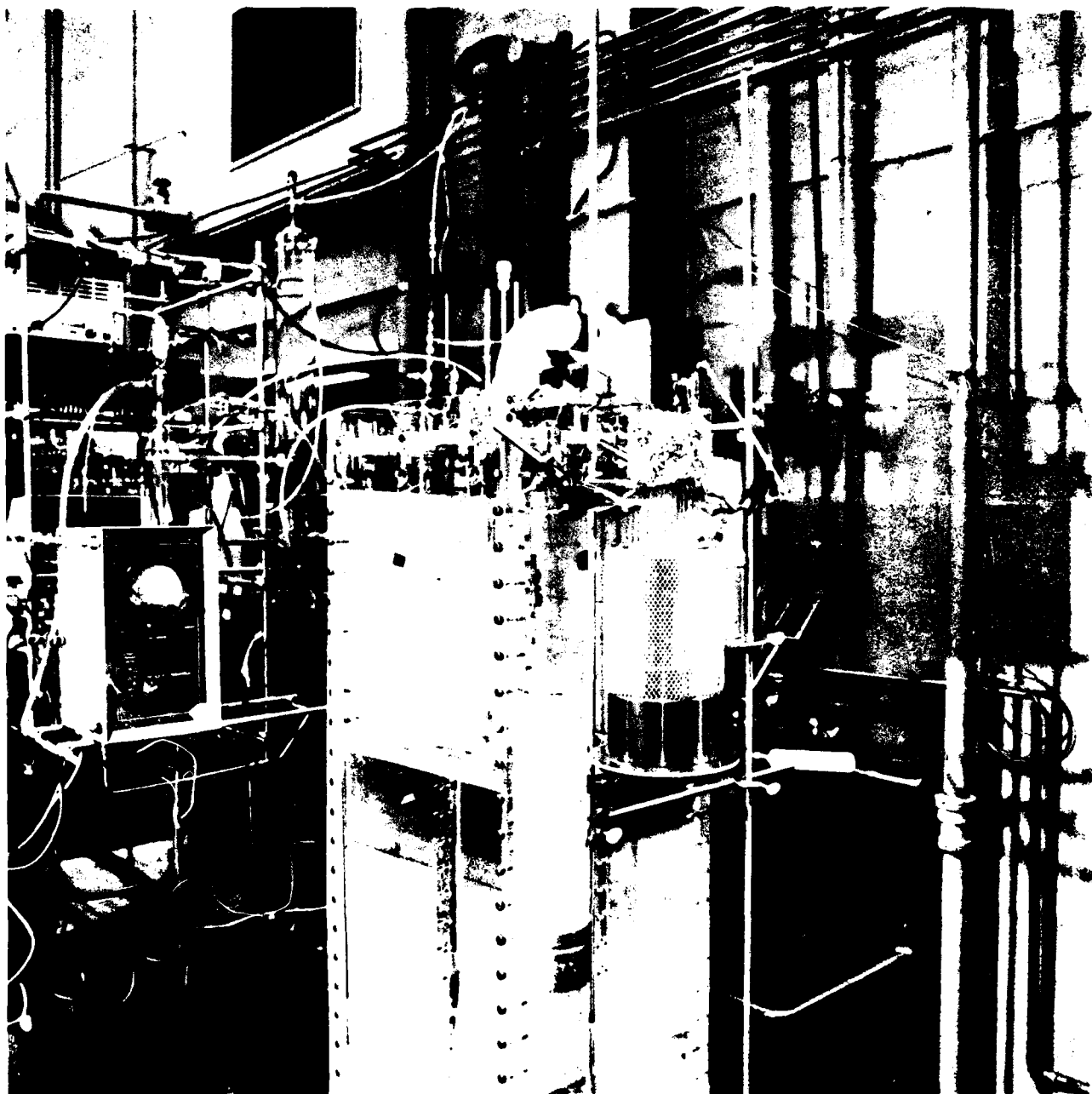
SYMBOLIC REFERENCE MAP (R=1)

POINTS
DER

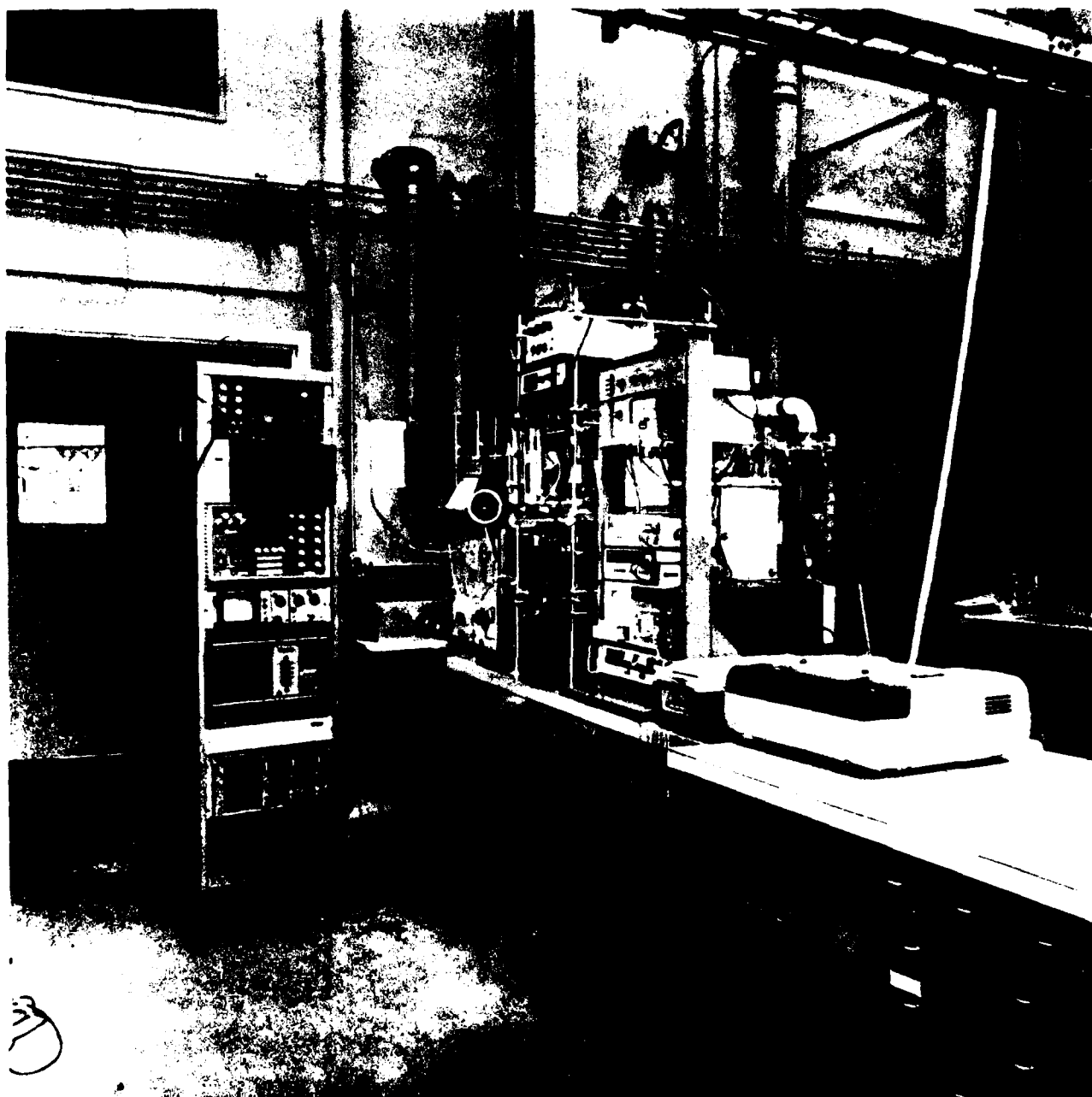
BLES	SN	TYPE	RELOCATION	
A		REAL		REAL /
AL1		REAL	/ /	REAL /
A1		REAL		REAL
B		REAL		REAL
B1		REAL	29-11	REAL

Appendix 2. Photographs of BNL Acid Spill Facility

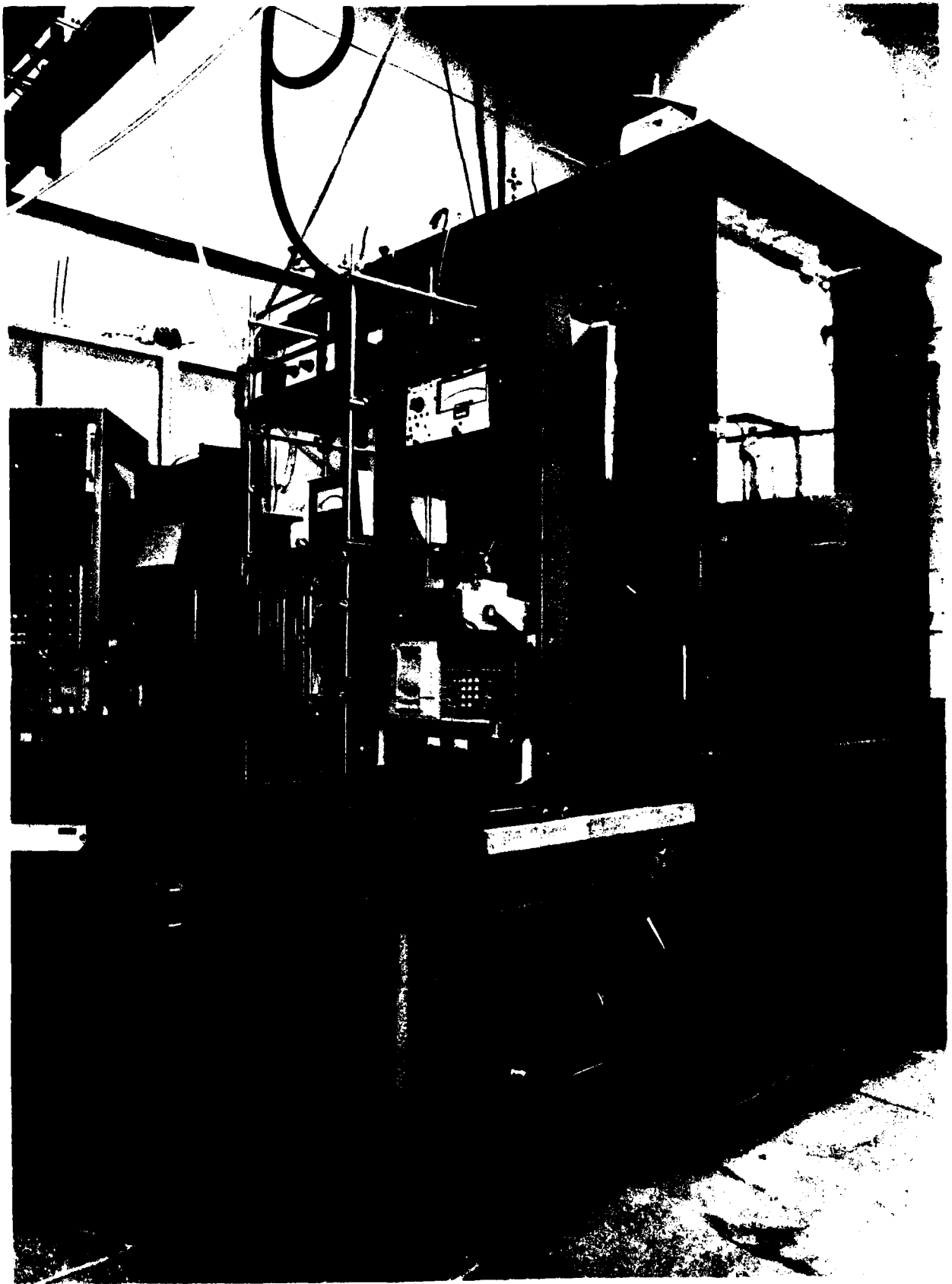




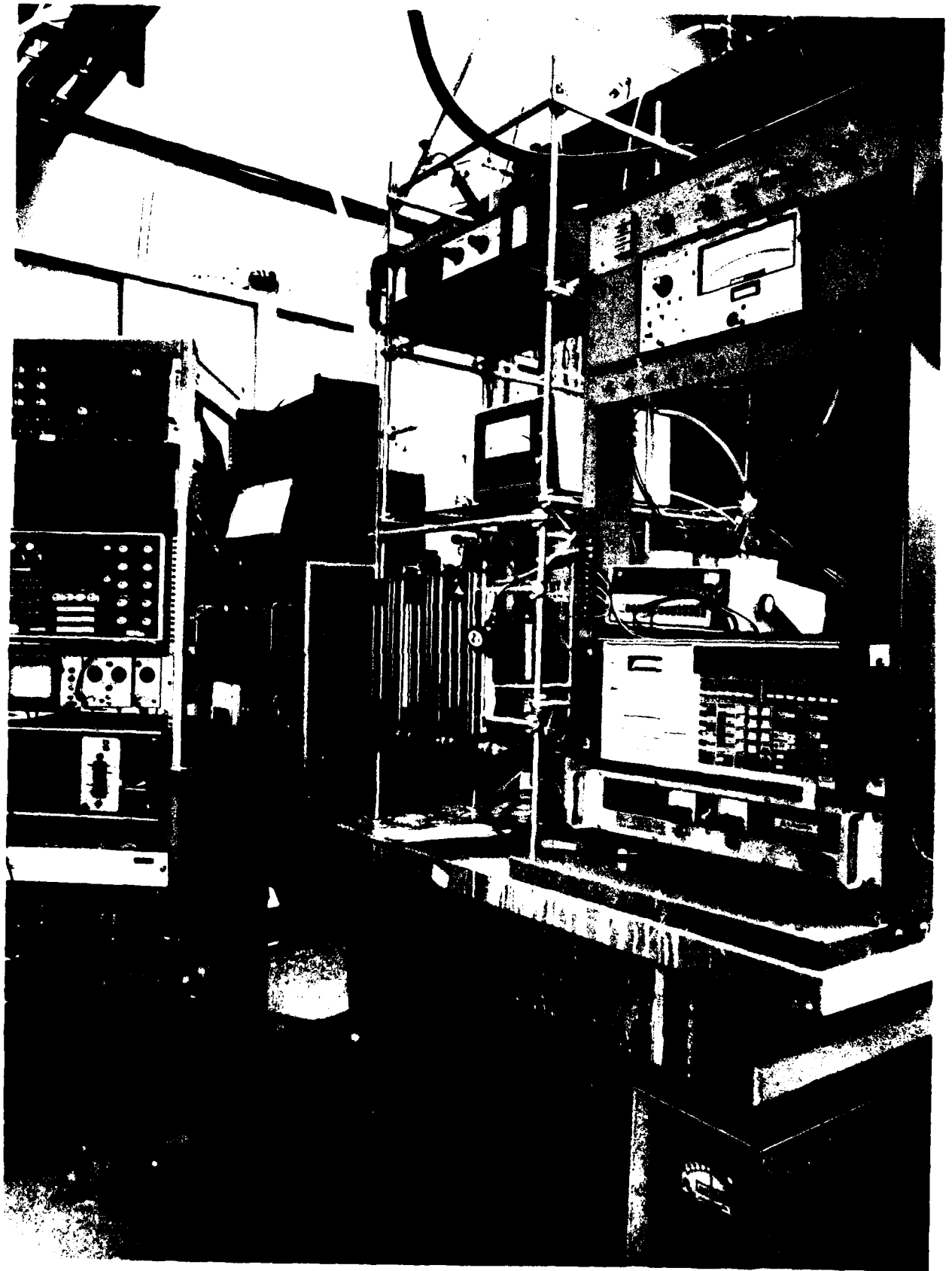
30-11

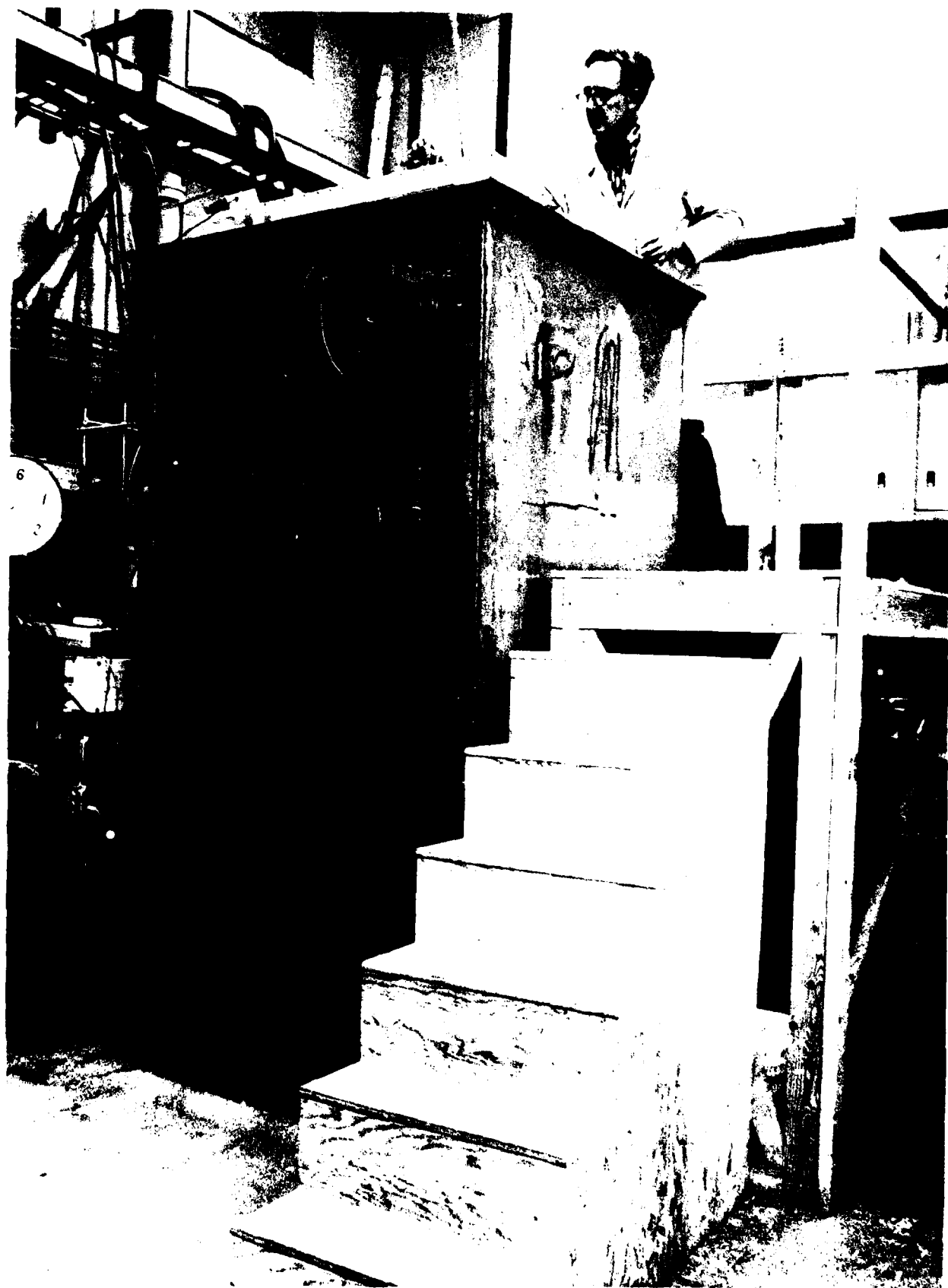


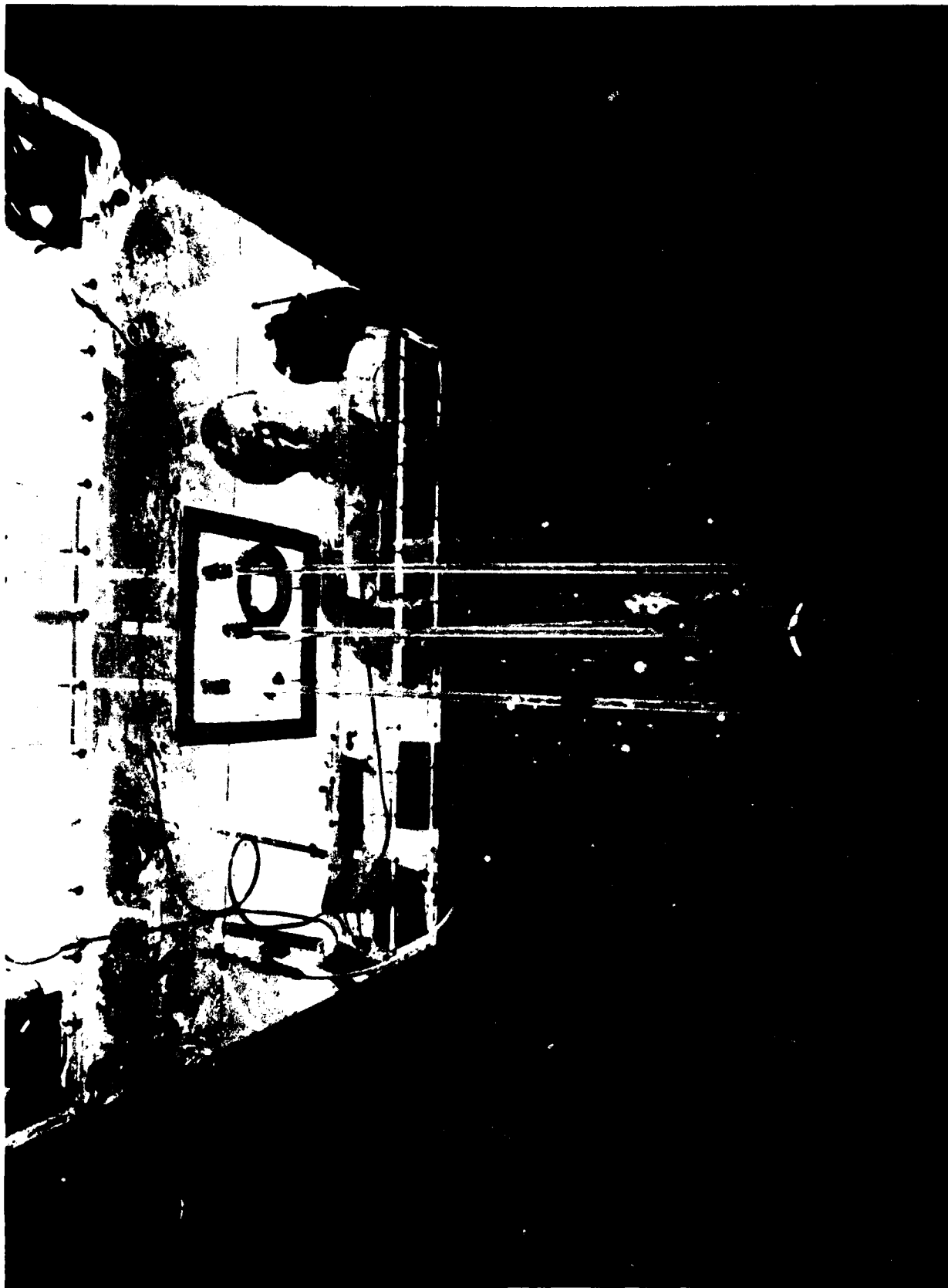
30-111



30-1v







30-v11

Appendix 3. Evaluation of the Integrals in Eq. (15)-(18)

$$\begin{aligned}\int_0^{\infty} 2\pi r' u' dr' &= \pi \tilde{u} \int_0^{\infty} 2r' e^{-r'^2/b'^2} dr' \\ &= \pi \tilde{u} \left[-b'^2 e^{-r'^2/b'^2} \right]_0^{\infty} = \pi b'^2 \tilde{u}\end{aligned}$$

$$\begin{aligned}\int_0^{\infty} 2\pi r' u'^2 \rho' dr' &= \pi \rho'_w \tilde{u}^2 \int_0^{\infty} 2r' e^{-2r'^2/b'^2} dr' \\ &= \pi \rho'_w \tilde{u}^2 \left[-\frac{b'^2}{2} e^{-2r'^2/b'^2} \right]_0^{\infty} = \frac{1}{2} \pi \rho'_w b'^2 \tilde{u}^2\end{aligned}$$

$$\begin{aligned}\int_0^{\infty} 2\pi r' g \Delta \rho' dr' &= \pi g \rho'_w P(x') \int_0^{\infty} 2r' e^{-r'^2/\lambda^2 b'^2} dr' \\ &= \pi g \rho'_w P(x') \left[-\lambda^2 b'^2 e^{-r'^2/\lambda^2 b'^2} \right]_0^{\infty} = \pi \lambda^2 g \rho'_w b'^2 P(x')\end{aligned}$$

$$\begin{aligned}\int_0^{\infty} 2\pi r' u' \rho' C_p T' dr' &= \pi \rho'_w \tilde{u} C_p(\tilde{y}) \tilde{T} \int_0^{\infty} 2r' e^{-\left(1+\frac{1}{\lambda^2}\right) \frac{r'^2}{b'^2}} dr' \\ &= \pi \rho'_w \tilde{u} C_p(\tilde{y}) \tilde{T} \left[-\frac{\lambda^2 b'^2}{\lambda^2 + 1} e^{-\left(1+\frac{1}{\lambda^2}\right) \frac{r'^2}{b'^2}} \right]_0^{\infty} \\ &= \pi \frac{\lambda^2}{\lambda^2 + 1} \rho'_w b'^2 \tilde{u} C_p(\tilde{y}) \tilde{T}\end{aligned}$$

$$\begin{aligned}\text{Now, } \frac{\partial y'}{\partial x'} &= \frac{\partial}{\partial x'} \left[\tilde{y}(x') e^{-r'^2/\lambda^2 b'^2} \right] \\ &= \left[\frac{d\tilde{y}}{dx'} + \tilde{y} \frac{2r'^2}{\lambda^2 b'^3} \frac{db'}{dx'} \right] e^{-r'^2/\lambda^2 b'^2}\end{aligned}$$

Therefore,

$$\begin{aligned}\int_0^\infty 2\pi r' u' \rho' \left(\frac{\partial \Delta H}{\partial y'} \right) \left(\frac{\partial y'}{\partial x'} \right) dr' &= -\pi \rho_w' \tilde{u} \int_0^\infty 2r' (A - By' + Cy'^2) \cdot \\ &\quad \left[\frac{d\tilde{y}}{dx'} + \tilde{y} \frac{2r'^2}{\lambda^2 b'^3} \frac{db'}{dx'} \right] e^{-(1+\frac{1}{\lambda^2})\frac{r'^2}{b'^2}} dr'\end{aligned}$$

In general,

$$\int_0^\infty 2r' \left[\frac{d\tilde{y}}{dx'} + \tilde{y} \frac{2r'^2}{\lambda^2 b'^3} \frac{db'}{dx'} \right] e^{-(1+\frac{n}{\lambda^2})\frac{r'^2}{b'^2}} dr' = \frac{\lambda^2 b'^2}{\lambda^2 + n} \left[\frac{d\tilde{y}}{dx'} + \frac{2\tilde{y}}{\lambda^2 + n} \frac{1}{b'} \frac{db'}{dx'} \right]$$

Thus,

$$\int_0^\infty 2\pi r' u' \rho' \left(\frac{\partial \Delta H}{\partial y'} \right) \left(\frac{\partial y'}{\partial x'} \right) dr' = -\pi \lambda^2 \rho_w' b'^2 \tilde{u} \left[\tilde{Q}(\tilde{y}) \frac{d\tilde{y}}{dx'} + \tilde{S}(\tilde{y}) \frac{2\tilde{y}}{b'} \frac{db'}{dx'} \right]$$

$$\text{where } \tilde{Q}(\tilde{y}) = \frac{A}{\lambda^2 + 1} - \frac{B}{\lambda^2 + 1} \tilde{y} + \frac{C}{\lambda^2 + 3} \tilde{y}^2$$

$$\tilde{S}(\tilde{y}) = \frac{A}{(\lambda^2 + 1)^2} - \frac{B}{(\lambda^2 + 2)^2} \tilde{y} + \frac{C}{(\lambda^2 + 3)^2} \tilde{y}^2$$

$$\begin{aligned}
 \int_0^{\infty} 2\pi r' u' \rho' y' dr' &= \pi \rho_w' \tilde{u} y \int_0^{\infty} 2r' e^{-\left(1+\frac{1}{\lambda^2}\right) \frac{r'^2}{b'^2}} dr' \\
 &= \pi \left(\frac{\lambda^2}{\lambda^2+1} \right) \rho_w' b'^2 \tilde{u} y
 \end{aligned}$$

Appendix 4. Computer Program for Continuous Releases

The program solves the dimensionless governing equations for the continuous release of 96% H_2SO_4 into stagnant water. No input data is necessary. The output tabulates the following dimensionless quantities from the point of release up to a dimensionless distance of 100: depth, flowrate, radius, velocity, mass fraction, temp. increment. A description of the FORTRAN parameters is given as follows:

FORTRAN Parameters	Description
ALPHA	α
AL	λ
ALSQ	λ^2
CP	C_p
ETA1	η_1
SHI1	ζ_1
GA	γ
AL1	λ_1
MO	initial momentum flux
X	x
TI	T
Y	y
RAD	b
VEL	u
THI	ψ
Z	An array representing V,M,N and X
DER	A subroutine to calculate the derivatives of Z


```

1      PROGRAM DIFF (OUTPUT)
      DIMENSION Z(4), ZP(4), TEMP(4,5)
      REAL M0
      EXTERNAL DER
5      COMMON GA, AL1, AL2, ALPHA, ETA1, ETA2, ETA3, SHI1, SHI2, ALSQ, TI1
      DATA G, Y0, A, B, C/98.0, 0.96, 63.091, 128.698, 558.288/
      ALPHA = 1.11
      AL = 1.16
      ALSQ = AL*AL
10     CP = 1.109346763-0.791366907*Y0
      ETA1 = 1.0/CP
      ETA2 = 0.602626787/CP
      ETA3 = 1.19346763/CP
      SHI1 = 0.791366907/CP
15     SHI2 = 1.191549227/CP
      GA = A*Y0/CP
      AL1 = B*Y0/A
      AL2 = C*Y0*Y0/A
      M0 = 2069.5
20     TI1 = 5.0
      CX = (M0/G)**(1.0/3.0)
      RAD = 0.15/CX
      PRINT 200
200    FORMAT(1H1)
      PRINT 100
25     100    FORMAT(//1X, *DEPTH*, 5X, *FLOW RATE*, 8X, *RADIUS*, 7X, *VELOCITY*, 6X,
      + *MASS FRACT*, 4X, *TEMP INCR(OC)*, 4X, *BUOYANCY*/)
      N = 4
      H = 0.1
30     Z(1) = 1.0
      Z(2) = 1.0
      Z(3) = TI1/GA
      Z(4) = 1.0
      X = 0.0
35     Q = 0.0
      TI = TI1
      Y = Y0
      IF(X.LE.3.0) ALPHA = 0.165
      CALL DER(X, H, N, Z, ZP, Q, DER, TEMP)
40     101    CONTINUE
      VEL = Z(2)/Z(1)
      Y = Y0*Z(4)/Z(1)
      IF(Y.LE.0.6625) GO TO 25
      IF(Y.LE.0.8448) GO TO 30
45     THI = ETA3-SHI1*Y
      GO TO 40
      25     THI = ETA1-SHI1*Y
      GO TO 40
      30     THI = ETA2-SHI2*Y
50     40     CONTINUE
      TI = GA*Z(3)/(THI*Z(1))
      50     CONTINUE
      RAD = Z(1)/SQRT(Z(2))
      PRINT 1, X, Z(1), RAD, VEL, Y, TI
55     1      FORMAT(F6.1, 6E15.6)
      IF(X.GT.10.0) GO TO 102
      DO 10 I=1,5

```

PROGRAM DIFF

76/76 OPT=1

FTN 4.54414

```

      ALPHA = 0.11
      IF(X.LE.3.0)ALPHA = 0.065
60      CALL DEQ(X,H,N,Z,ZP,Q,DER,TEMP)
      10  CONTINUE
      GO TO 101
      102 CALL EXIT
      END

```

SUBROUTINE DER

76/76 OPT=1

FTN 4.54414

```

1      SUBROUTINE DER(X,N,Z,ZP)
      DIMENSION Z(4),ZP(4)
      COMMON GA,AL1,AL2,ALPHA,ETA1,ETA2,ETA3,SHI1,SHI2,ALSO,TIG
      DATA G,Y0,A,B,C/984.0,0.96,63.091,128.698,558.288/
5      Y = Z(4)/Z(1)
      40  CONTINUE
      YP = Y0*Y
      IF(YP.LE.1.6625)GO TO 10
      IF(YP.LE.0.8448)GO TO 20
10     THI = ETA3-SHI1*YP
      GO TO 30
      10  THI = ETA1-SHI1*YP
      GO TO 30
      20  THI = ETA2-SHI2*YP
15     30  CONTINUE
      ZHI = Y/(5.44405/Y0-4.44405*Y)
      PHI = 1.0+(3.0943-4.0834*ZHI+1.9132*ZHI*ZHI)*ZHI
      F = 1.0 - 1.000535977*GA*Z(3)/(THI*Z(1))
      50  CONTINUE
20     U = 1.0/(ALSO + 1.0)
      V = AL1*Y/(ALSO + 2.0)
      R = AL2*Y*Y/(ALSO + 3.0)
      Q = U - V + R
      S = U/(ALSO + 1.0) - V/(ALSO + 2.0) + R/(ALSO + 3.0)
25     ZP(1) = 2.0*ALPHA*SQRT(Z(2))
      ZP(2) = 2.0*ALSO*Z(1)*Z(1)*(PHI*F-1.0)/Z(2)
      ZP(3) = (ALSO+1.0)*Y*((Q-2.0*S)*ZP(1)+S*Z(1)*ZP(2)/Z(2))
      ZP(4) = 0.0
      RETURN
30     END

```

SYMBOLIC REFERENCE MAP (R=1)

POINTS
DEF

32-11

RIFS

SN TYPE

REF. NO.

Appendix 5. A non-linear Iterative Algorithm
for Inverting Diffusion Battery DATA

Abstract

A non-linear iterative algorithm is presented for use in retrieving particle size information from diffusion battery data. It is shown with numerically generated test cases that the inversion method has a relatively fast rate of convergence, good size resolution, and is stable to as much as 5% random errors in the data. Application of the method to experimental monodisperse aerosol data gives satisfactory agreements between retrieved particle sizes and corresponding stated sizes up to 0.8 μm in diameter.

I. Introduction

Diffusional deposition in a flow stream through narrow channels has long been recognized as an effective means of size classification of polydisperse submicron particles. Since smaller particles, whose diffusion coefficients are larger than those of the larger particles, are readily removed from the stream by diffusion to the channel walls, diffusion batteries, consisting either of circular or rectangular channels, have been constructed according to this principle [1]. More compact and versatile versions made of a series of stainless-steel screens are now commercially available [2,3].

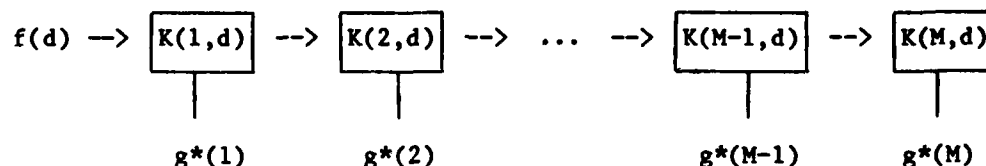
However, difficulties in the analysis of diffusion battery data have, until recently, prevented it from being widely used for routine particle sizing. Several investigators [4,5] have assumed a size distribution consisting of histograms over a finite number of discrete size classes to fit the data, whereas Raabe [6,7] has adopted a lognormal distribution to match grouped data. Mercer and Greene [8] have assumed instead that the diffusion coefficients of the particles are lognormally distributed, from which an "equivalent diffusion" lognormal distribution can be deduced for the particle diameters via an empirical correlation between diameter and diffusivity. Recently, Busigin, Van der Vooren and Phillips [9] have assumed that the actual size distribution can be represented by a sum of lognormal distributions with different parameters and adopted an iterative random search technique to determine the parameters that give a best fit to the data.

In the present paper, a new algorithm, belonging to the class of nonlinear iterative inversion techniques, is shown to be well suited for the retrieval of particle size information from diffusion battery data.

Although the formulation of the algorithm for solving inverse problems in general has been given elsewhere [10], a brief description of the method as applied to diffusion battery data is presented here in section II. In section III, its performance is checked with a few test cases of known size distributions. Finally, in section IV, it is applied to actual experimental data taken with latex spheres and sodium chloride particles whose diameters are known beforehand.

II. Theory

A M-stage diffusion battery may be depicted schematically, as follows,



where $f(d)$ is the unknown size distribution of an aerosol sample, $g^*(l)$, $l=1, \dots, M$, is the number of particles which penetrate to the l th stage and $K(l, d)$ is the fractional penetration of particles with diameter d at the l th stage. Then, f and g^* are related by

$$g^*(l) = \int_0^{\infty} K(l, d) f(d) dd \quad l=1, \dots, M \quad (1)$$

which is the Fredholm integral equation of the first kind. To find a solution of Eq. (1) is a well-known ill-posed problem. In general, a unique solution may not even exist. There are additional problems associated with instabilities in numerical computations. Many methods for obtaining an approximate solution have been proposed (see, for example, [11-15]); each has its shortcomings and advantages over others for a specific class of the kernel function, $K(l, d)$.

In actual inversion, Eq. (1) is usually discretized using an integration quadrature,

$$g^*(l) = \sum_{k=1}^N w_k K(l, d_k) f(d_k) \quad l=1, \dots, M \quad (2)$$

where w_k is the weight factor of the integration quadrature and the diameter is discretized in N points over certain finite range $[a, b]$. The new algorithm states that the solution is obtained by iteration via

$$f_i(d_k) = [1 + \psi_{i-1}(l, d_k)] f_{i-1}(d_k) \quad k=1, \dots, N \quad (3)$$

beginning with some assumed initial distribution $f_0(d_k)$. The corresponding penetration is then given by

$$g_i(l) = \sum_{k=1}^N w_k K(l, d_k) f_i(d_k) \quad l=1, \dots, M \quad (4)$$

$\psi_{i-1}(l, d_k)$ is chosen to have the functional form

$$\psi_{i-1}(l, d_k) = A_{i-1}(l) K^2(l, d_k) + B_{i-1}(l) \cdot K(l, d_k) + C_{i-1}(l) \quad (5)$$

where $A_{i-1}(l)$, $B_{i-1}(l)$, and $C_{i-1}(l)$ are coefficients to be determined by some specified conditions. In order that the iteration, Eq. (3), always produces positive values for $f_i(d_k)$, $\psi_{i-1}(l, d_k)$ is required to satisfy

$$|\psi_{i-1}(l, d_k)| < 1 \quad (6)$$

for all i , l , and k .

It can be readily proved from calculation that $K(l, d)$ is monotonic decreasing both in l and d . Then, since $f(d)$ is positive for all d , Eq. (1) implies that $g^*(l)$ is also monotonic decreasing. Thus, g^* can be so labelled that $g^*(1)$ and $g^*(M)$ is the largest and smallest values, respectively. The fundamental feature of the new algorithm is that

$$\sum_{k=1}^N w_k K(1, d_k) f_1(d_k) = g_1(1) = \eta_1 g^*(1) \quad (7)$$

$$\sum_{k=1}^N w_k K(M, d_k) f_1(d_k) = g_1(M) = \eta_M g^*(M) \quad (8)$$

for all i , where η_1 and η_M are positive constants close to 1. The effect of each iteration, under conditions (7) and (8), is to modify $f_1(d_k)$ such that the corresponding $g_1(l)$, $l=2, \dots, M-1$, always lie within the range bounded by $\eta_1 g^*(1)$ and $\eta_M g^*(M)$. The introduction of η_1 and η_M is to impart extra flexibility to the algorithm when dealing with experimental data with random errors. Substitution of Eq. (3) into Eq. (7) and (8) gives

$$\sum_{k=1}^N w_k K(1, d_k) \psi_{i-1}(l, d_k) f_{i-1}(d_k) = 0 \quad (9)$$

$$\sum_{k=1}^N w_k K(M, d_k) \psi_{i-1}(l, d_k) f_{i-1}(d_k) = 0 \quad (10)$$

for all i , and a given l . From Eqs. (5), (9), and (10), $\psi_{i-1}(l, d_k)$ can be written as

$$\psi_{i-1}(l, d_k) = R_{i-1}(l) \cdot \phi_{i-1}(l, d_k) \quad (11)$$

$$\text{where } \phi_{i-1}(l, d_k) = \frac{\gamma_{i-1}(l) \left[K^2(l, d_k) - \frac{h_{i-1}(1, l)}{\eta_1 g^*(1)} \right] + K(l, d_k) - \frac{p_{i-1}(1, l)}{\eta_1 g^*(1)}}{Q_{i-1}(l)}$$

$$Q_{i-1}(l) = \max_{k=1, \dots, N} \left| \gamma_{i-1}(l) \left[K^2(l, d_k) - \frac{h_{i-1}(1, l)}{\eta_1 g^*(1)} \right] + K(l, d_k) - \frac{p_{i-1}(1, l)}{\eta_1 g^*(1)} \right|$$

$$\gamma_{i-1}(\ell) = - \frac{p_{i-1}(M, \ell) - \frac{\eta_M g^*(M)}{\eta_1 g^*(1)} p_{i-1}(1, \ell)}{h_{i-1}(M, \ell) - \frac{\eta_M g^*(M)}{\eta_1 g^*(1)} h_{i-1}(1, \ell)}$$

$$h_{i-1}(j, \ell) = \sum_{k=1}^N w_k K(j, d_k) K^2(\ell, d_k) f_{i-1}(d_k)$$

$$p_{i-1}(j, \ell) = \sum_{k=1}^N w_k K(j, d_k) K(\ell, d_k) f_{i-1}(d_k)$$

and $R_{i-1}(\ell)$ is as yet undetermined. Obviously, the definition of $\phi_{i-1}(\ell, d_k)$ indicates that

$$|\phi_{i-1}(\ell, d_k)| \leq 1 \quad (12)$$

for all i, ℓ, k . Then, Eq. (6) implies that

$$|R_{i-1}(\ell)| < 1 \quad (13)$$

for all i and ℓ .

In order that the iteration process is convergent, $R_{i-1}(\ell)$ must be chosen subject to condition (13) such that $f_i(d)$ is modified at each iteration in a direction as to reduce the residual error between $g_i(\ell)$ and $g^*(\ell)$. However, because of the ill-posed nature of the problem, the solution is also required to be as smooth as possible. Mathematically, this is expressed as: find $R_{i-1}(\ell)$ which minimizes

$$\Gamma = \delta_1^2(\ell) + \lambda S(f_1) \quad (14)$$

where $\delta_1(\ell)$ is the residual error defined as

$$\begin{aligned}
\delta_1(l) &= 1 - \frac{g_1(l)}{g^*(l)} \\
&= 1 - \frac{1}{g^*(l)} \sum_{k=1}^N w_k K(l, d_k) f_1(d_k) \\
&= \delta_{1-1}(l) - \frac{Z_{1-1}(l)}{g^*(l)} \cdot R_{1-1}(l)
\end{aligned} \tag{15}$$

$$Z_{1-1}(l) = \sum_{k=1}^N w_k K(l, d_k) \phi_{1-1}(l, d_k) f_{1-1}(d_k),$$

$S(f_1)$ is a functional of f_1 , which is a measure of the smoothness of f_1 and λ is a Lagrange multiplier. This approach of determining $R_{1-1}(l)$ is analogous to that in the method of regularization. Several measures of smoothness have been considered by different investigators, for example, the variance, the sum of the squares of first differences, or the sum of the squares of second differences, etc. In the present formulation, the following definition of the measure of smoothness will be chosen,

$$\begin{aligned}
S(f_1) &= \int_0^\infty [f_1(d) - f_{1-1}(d)]^2 dd \\
&= \sum_{k=1}^N w_k [f_1(d_k) - f_{1-1}(d_k)]^2 \\
&= D_{1-1}(l) \cdot R_{1-1}^2(l)
\end{aligned} \tag{16}$$

where $D_{1-1}(l) = \sum_{k=1}^N w_k [\phi_{1-1}(l, d_k) f_{1-1}(d_k)]^2$. It should be pointed out that this definition of the measure of smoothness is only a matter of convenience to obtain an expression for $R_{1-1}(l)$. Thus, $S(f_1)$ may be considered

as proportional to the total amount of adjustment of f_{i-1} at the i^{th} iteration and by requiring it to stay within certain bounds has the effect of restricting any drastic change in f_i during the process of iteration. Substitution of Eq. (15) and (16) into (14) and then equating $d\Gamma/dR_{i-1}(\ell)$ to zero gives

$$R_{i-1}(\ell) = \frac{\frac{Z_{i-1}(\ell)}{g^*(\ell)} \delta_{i-1}(\ell)}{\left[\frac{Z_{i-1}(\ell)}{g^*(\ell)} \right]^2 + \lambda D_{i-1}(\ell)} \quad (17)$$

It is clear from Eq. (17) that a large value of λ reduces the amount of change in f_{i-1} at the i^{th} iteration and hence tends to maintain smoothness in f_i , while a small value of λ accelerates convergence.

To initiate the iteration, an initial distribution $f_0(d_k)$ must be chosen such that it satisfies Eq. (7) and (8). Since the functional form of the sought distribution is in general not known a priori, $f_0(d_k)$ is first assumed to be a flat profile, i.e.,

$$\tilde{f}_0(d_k) = \zeta, \quad k=1, \dots, N$$

so that no bias is aimed at certain sizes. ζ is evaluated from Eq. (7).

$$\zeta = \frac{\eta_1 g^*(1)}{\sum_{k=1}^N w_k K(1, d_k)}$$

Then, $f_0(d_k)$ is obtained by adjusting $\tilde{f}_0(d_k)$ according to

$$f_0(d_k) = [1 + E \cdot K^2(M, d_k) + F] \tilde{f}_0(d_k) \quad (18)$$

where E and F are determined by the two conditions $g_0(1) = \eta_1 g^*(1)$ and $g_0(M) = \eta_M g^*(M)$. Therefore,

$$f_0(d_k) = \left\{ 1 + \left[\frac{\eta_M g^*(M) - \tilde{g}_0(M)}{h_0(M, M) - \frac{\tilde{g}_0(M)}{\eta_1 g^*(1)} h_0(1, M)} \right] \left[K^2(M, d_k) - \frac{h_0(1, M)}{\eta_1 g^*(1)} \right] \right\} \zeta \quad (19)$$

where

$$\tilde{g}_0(M) = \zeta \sum_{k=1}^N w_k K(M, d_k)$$

It should be pointed out that the form of $f_0(d_k)$ defined in Eq. (18) is deliberately chosen to be similar to $\psi_{i-1}(l, d_k)$. If Eq. (19) should result in negative values of $f_0(d_k)$ for some d_k , $|\eta_M g^*(M) - \tilde{g}_0(M)|$ is successively reduced by temporarily adjusting $g^*(M)$ until $f_0(d_k) > 0$ for all k and then Eq. (19) is repeatedly applied until $g^*(M)$ returns to its original given value.

Twomey [16] proposed a different expression for $\psi_{i-1}(l, d_k)$

$$\psi_{i-1}(l, d_k) = K(l, d_k) \left[\frac{g^*(l)}{g_{i-1}(l)} - 1 \right] \quad (20)$$

Since for any physical system $K(l, d_k)$ can always be normalized to be less than or equal to 1, $\psi_{i-1}(l, d_k)$ in Eq. (20) satisfies the condition (6). He applied Eq. (3) with (20) to determine the size distribution from measurements of the number of particles through nuclepore filters and showed that it yields better results than the constrained linear inversion method, particularly when the sought distribution is not smooth. Although the Twomey's scheme is simpler, the present technique, derived from a general mathematical basis, is considered more systematic with built-in control of speed

of convergence and smoothness of the solution. In the next section, the two methods will be compared by means of test cases of known distributions.

The iteration procedure of the present algorithm is described as follows:

- (1) compute $f_0(d_k)$ from Eq. (19)
- (2) begin iteration at $l=2$
- (3) put λ equal to some chosen value
- (4) compute $\phi_{i-1}(l, d_k)$
- (5) calculate $R_{i-1}(l)$ from Eq. (17)
- (6) test if $|R_{i-1}(l)| < 1$; if not, increase λ successively by one order of magnitude until $|R_{i-1}(l)| < 1$
- (7) adjust $f_{i-1}(d_k)$ by Eq. (3)
- (8) compute $g_i(l')$, $l'=2, \dots, M-1$
- (9) increase l by 1 and go back to step (3) until $l=M-1$
- (10) calculate $\delta_i(l')$, $l'=2, \dots, M-1$
- (11) find $\max_{l'=2, \dots, M-1} |\delta_i(l')|$; if it is less than certain specific error limit criterion, stop iteration, if not, increase i by 1 and go back to step (2) to repeat the iteration process.

One pass of the iteration procedure from step (2) to (10) will be called one cycle of iteration.

III. Test Cases

Numerical test cases are generated by passing hypothetical aerosols with known distribution through the diffusion battery. At Brookhaven National Laboratory, experimental research is being conducted using a

prototype diffusion battery based on the original design of Sinclair [1]. It is made of collimated hole structures with approximately 9750 circular channels in each stage and has eleven stages and twelve sampling ports ($M=12$). The lengths of the various stages are listed in Table 1.

Exact mathematical expression has been derived for the fractional penetration $K(l,d)$ by Gormley and Kennedy [17].

Table 1. Lengths of Diffusion Battery Stages

Stage	Length (cm)
1	0.3175
2	0.3175
3	0.6350
4	0.9525
5	1.2700
6	1.9050
7	2.5400
8	3.8100
9	5.0800
10	7.6200
11	10.1600

$$K(l,d) = K(l-1,d) \left\{ 8 \sum_{n=1}^{\infty} \frac{\theta_x(l, \beta_n)}{\beta_n^3 \theta_\beta(l, \beta_n)} e^{-\beta_n^2 \mu/2} \right\} \quad (21)$$

where $\theta(x, \beta) = e^{-\beta x^2/2} \left\{ 1 + \sum_{n=1}^{\infty} J_n(\beta x^2)^n \right\}$

$$J_n = \left[\frac{2(2n-1)-\beta}{(2n)^2} \right] J_{n-1}$$

$$J_0 = 1$$

and β_n are roots of $\theta(1, \beta) = 0$, $\mu = \frac{\pi DL}{q}$ is the diffusion parameter, D the diffusion coefficient of a particle of diameter d , L length of the circular channel between ports l and $l-1$ and q is the volumetric flow rate per channel. However, the five terms approximation proposed by Thomas [18] will be adopted,

$$K(l, d) = K(l-1, d) [0.819 e^{-3.65\mu} + 0.097 e^{-22.3\mu} + 0.032 e^{-57\mu} + 0.027 e^{-123\mu} + 0.025 e^{-750\mu}] \quad (22)$$

$l=2, \dots, M$. This expression has been verified experimental by Sinclair et al. [19] for particles smaller than $0.2 \mu m$ in diameter. In this paper, it is assumed to be still valid for particles up to $1 \mu m$ in diameter. The diffusion coefficient D is calculated from Einstein equation with the Cunningham's slip correction,

$$D = \frac{kT}{3\pi\zeta d} \left[1 + (1.257 + 0.4 e^{-0.55d/\sigma}) \frac{2\sigma}{d} \right]$$

where k is the Boltzmann constant, T the absolute temperature of the carrier gas, ζ the viscosity of the carrier gas, σ the mean free path of the gas molecules. It should be noted that the sampling ports are so labelled that the first port ($l=1$) corresponds to the input of the diffusion battery, i.e.,

$$K(1, d) = 1 \text{ for all } d \quad (23)$$

Eq. (23) indicates that $g^*(1)$ represents the total number of particles entering the diffusion battery. Henceforth in the discussion of test cases

and experimental measurements, the diffusion battery data $g^*(l)$, $l=1, \dots, M$, will be divided by $g^*(1)$ so that $g^*(1)$ becomes 1; in other words the inversion algorithm will yield a normalized size distribution. Accordingly, n_1 can be fixed at 1.

Since in many actual data inversion, the significant size range of the aerosol sample, whose size distribution is sought, is often insufficiently known a priori, a diameter range $[0.001 \mu\text{m}, 10.0 \mu\text{m}]$ over four decades of magnitude will be assumed which is considered to be more than sufficient for most applications of diffusion battery. This diameter range is then discretized uniformly on a logarithmic scale, i.e.,

$$d_k = d_1 \left(\frac{d_N}{d_1} \right)^{(k-1)/(N-1)} \quad k=1, \dots, N \quad (24)$$

where $d_1 = 0.001 \mu\text{m}$ and $d_N = 10.0 \mu\text{m}$. Simpson's rule will be adopted as the integration quadrature.

Test cases are generated by assuming a normalized size distribution and calculating $g^*(l)$, $l=1, \dots, M$ from Eq. (2). In all cases, fifty-one ($N=51$) diameter points and a flow rate of 2 l/min are used in computing $K(l, d_k)$. Because of the inherent non-uniqueness character of the problem, certain measures have to be devised to terminate the iteration process at the "best" solution. However, the standard of the "best" solution is somewhat ambiguous, depending on the quality of the given data g^* and the desired accuracy of the retrieved f . In the following discussion of test cases, the maximum value of the absolute value of $\delta_1(l)$, $l=2, \dots, M-1$, after each cycle of iteration, is calculated,

$$\bar{\delta}_1 = \max_{\ell=2, \dots, M-1} |\delta_1(\ell)|. \quad (25)$$

If $\bar{\delta}_1$ is less than some prescribed limit or if the number of cycles of iteration is equal to a certain prescribed number, the iteration process is terminated. Our experience with the present algorithm indicates, however, that as the iteration process proceeds, $\bar{\delta}_1$ decreases and then in some cases it starts to increase again at certain point of the iteration process. Thus, two more provisions are incorporated in the computer program to record the two "best" iterated distributions in the iteration process according to these two criteria:

(1) The retrieved distribution at the I_δ^{th} cycle of iteration which gives the smallest $\bar{\delta}_1$, compared with that given by iterated distributions at iterations prior to and after I_δ , that is

$$\bar{\delta}_{I_\delta} = \min_i \bar{\delta}_i \quad (26)$$

(2) The retrieved distribution at the I_ϵ^{th} cycle of iteration which gives the smallest global residual error ϵ_1 in the least square sense compared with that given by iterated distributions prior to and after I_ϵ , that is

$$\epsilon_{I_\epsilon} = \min_i \epsilon_i \quad (27)$$

where $\epsilon_1 = \sum_{\ell=2}^{M-1} \delta_1^2(\ell)$ after each cycle of iteration.

I_δ sometimes does not coincide with I_ϵ .

A total of ten test cases are now presented. The retrieved distributions by the new algorithm (dashed curve) developed in this paper are compared with those obtained by Twomey algorithm (broken curve) relative to the original known distributions (solid curve) in Fig. (1) to (10). The accuracy of the solutions (measured by $\bar{\delta}_{I_\delta}$ and ϵ_{I_ϵ}) and the rate of convergence (measured by I_δ and I_ϵ) by both schemes are summarized in Table 2. In all cases, the number of cycles of iteration is set for a limit of 10000.

Test case 1 (Fig. 1) a monodisperse distribution of size $0.65 \mu\text{m}$ in diameter.

$$\lambda = 0.1, \eta_M = 1.0$$

Test case 2 (Fig. 2) a lognormal distribution defined as

$$f(d_k) = \frac{C}{d_k} \exp \left\{ - \left[\frac{\ln(d_k/d_g)}{\sqrt{2} \ln \sigma_g} \right]^2 \right\}$$

Where C is a normalizing factor such that

$$\sum_{k=1}^N w_k f(d_k) = 1. \text{ In this case, } d_g = 0.15 \mu\text{m and}$$

$$\sigma_g = 2.0$$

$$\lambda = 0.1, \eta_M = 1.0$$

Test case 3 (Fig. 3) A lognormal distribution with $d_g = 0.8 \mu\text{m}$ and

$$\sigma_g = 1.5$$

$$\lambda = 0.1, \eta_M = 1.0$$

Test case 4 (Fig. 4) A lognormal distribution with $d_g = 0.8 \mu\text{m}$ and

$$\sigma_g = 3.0$$

$$\lambda = 0.1, \eta_M = 1.0$$

Test case 5 (Fig. 5)

a bimodal distribution, which is the sum of two lognormal distributions: $d_g = 0.03 \mu\text{m}$, $\sigma_g = 1.2$ and $d_g = 0.15 \mu\text{m}$, $\sigma_g = 1.4$, with the relative amount of each distribution in the ratio 1.0:5.0, respectively.

$$\lambda = 0.1, \eta_M = 1.0$$

Test case 6 (Fig. 6)

a bimodal distribution, which is a sum of two lognormal distributions: $d_g = 0.09 \mu\text{m}$, $\sigma_g = 1.2$ and $d_g = 0.6 \mu\text{m}$, $\sigma_g = 1.4$, with the relative amount of each distribution in the ratio 0.5:5.0, respectively.

$$\lambda = 0.1, \eta_M = 1.0$$

Test case 7 (Fig. 7)

a gamma distribution

$$f(d_k) = \frac{C}{d_k^4} \exp - \frac{8 \times 10^{-2}}{d_k^2} /$$

where C is the normalizing factor

$$\lambda = 0.01, \eta_M = 1.0$$

Test case 8 (Fig. 8)

a Junge distribution

$$f(d_k) = \begin{cases} 0.001 & 0.001 \mu\text{m} \leq d_k < 0.05 \mu\text{m} \\ C \cdot d_k^{-3} & 0.05 \mu\text{m} \leq d_k \leq 10.0 \mu\text{m} \end{cases}$$

where C is the normalizing factor

$$\lambda = \begin{cases} 0.01 & \bar{\delta}_1 > 10^{-3} \\ 0.001 & \bar{\delta}_1 < 10^{-3} \end{cases}$$

$$\eta_M = 1.0$$

Test case 9 (Fig. 9)

same as Test case 2, except that 5% random noise was superimposed on $g^*(l)$, $l=2, \dots, M$, by making use of a random number generator in the computer function library. In this case, η_M is randomly fixed at within 5% about 1.0. Since the amount of

error in g^* is known a priori, the iteration is terminated as soon as $\bar{\delta}_1 < 5\%$.

$$\lambda = 1.0$$

Test case 10 (Fig. 10) same as Test case 4 except that 5% random noise was superimposed on $g^*(l)$, $l = 2, \dots, M$

$$\lambda = 1.0$$

Table 2. Comparison of performance between methods.

Test case	Present scheme		Twomey's scheme	
	I_δ	$\bar{\delta}_{I_\delta}$	I_δ	$\bar{\delta}_{I_\delta}$
1	10000	8.3×10^{-5}	10000	7.6×10^{-3}
2	694	1.0×10^{-5}	10000	8.4×10^{-4}
3	1268	9.7×10^{-6}	10000	5.8×10^{-3}
4	1861	1.0×10^{-5}	2722	1.1×10^{-3}
5	1605	5.0×10^{-5}	10000	1.7×10^{-3}
6	8226	5.0×10^{-5}	10000	8.0×10^{-4}
7	33	4.8×10^{-5}	10000	9.5×10^{-5}
8	2431	5.0×10^{-5}	10000	9.6×10^{-4}
9	24	5.0×10^{-2}	73	5.0×10^{-2}
10	23	5.0×10^{-2}	107	5.0×10^{-2}

The ten test cases just presented were constructed from size distribution models commonly used to describe atmospheric aerosol particles. Agreement between the retrieved distributions by the inversion scheme developed in this paper and the original distributions is excellent in most cases. Particularly in the last two test cases, the method was found to be stable to 5% random error in the given data. In comparison, the results by Twomey's scheme are in general less satisfactory with respect to the present scheme and it has a much slower rate of convergence to attain a given degree of accuracy, although it is simpler to implement. Furthermore, the present

scheme has an added advantage in that it has built-in control of the rate of convergence and the smoothness of the retrieved distribution. If the original distribution is predominant in sizes smaller than about 0.1 μm in diameter, Twomey's scheme gives results comparable in quality to that obtained by the present scheme, though it is still slower in convergence (see Test cases 2, 5, and 8). For distributions predominant in sizes greater about 0.3 μm in diameter, Twomey's scheme is very slow in convergence (see Test cases 1, 3, 6, and 7). Hitherto, diffusion battery has been used mainly in sampling particles smaller than 0.1 μm . Now, with the new inversion scheme developed in this paper, it is possible to extend the particle sizing range up to 0.8 μm in diameter, provided the flow rate is not too high.

Although the test cases above were based on the collimated hole structures diffusion battery, it is of interest to test the performance of the present inversion scheme for the parallel plate diffusion battery constructed by Busigin et al. [9] using the hypothetical gamma distribution

$$f(d_k) = \frac{C}{d_k^4} \exp \left(- \frac{4 \times 10^{-4}}{d_k^2} \right)$$

as the basis of comparison with their technique. Because of the design of this diffusion battery, the penetration at successive ports are 0.965, 0.861, 0.247, 0.023, and 0.002 for a flow rate of 2 l/min. In fact, the penetration at the last port is so small that considerable computer time was spent on calculating the initial profile via Eq. (19). Accordingly, data from the last port was neglected and the result of the present inversion scheme is shown as the dashed curve in Fig. 11 with $\lambda = 0.01$ and a size range [0.01 μm , 1.0 μm]. The accuracy at 6396 cycles of iteration is $\bar{\delta} < 10^{-5}$. Also shown in Fig. 11 (open circles) is the result using the

collimated hole structures diffusion battery (with the first 6 ports only). The agreement with the original distribution is only fair for the parallel plate diffusion battery, whereas the agreement is excellent for the collimated hole structures diffusion battery. The reason for the poorer performance of the present inversion scheme in the case of the parallel-plate diffusion battery may be attributed to the fact that the penetration drops sharply at the last three ports and consequently there is insufficient information to yield adequate resolution. While the technique of Busigin et al. gives slightly better agreement, the present method is faster (about 11 seconds of execution time) compared to 1 minute by their method.

IV. Interpretation of Experimental Data

The success of the inversion scheme developed in this paper is now further examined by applying it to real experimental data. Monodisperse samples of latex and sodium chloride particles were generated by an experimental setup shown schematically in Fig. (12), which has been described elsewhere [20]. Latex particles of sizes 0.312, 0.46, 0.6, and 0.801 μm in diameter and sodium chloride particle of size 0.26 μm in diameter were used. The penetrations of the collimated hole structures diffusion battery at a flow rate of 1.5 l/min were measured by a Climet optical counter for the latex particles and by a TSI continuous flow CNC for the salt particles. The normalized penetrations (relative to port 1, which is the input to the diffusion battery) are plotted in Fig. (13). The solid lines are the theoretical penetrations as calculated using Thomas' approximate expression (Eq. [22]). The agreement of the experimental data with the theoretical curves can be considered satisfactory. Irregularities in the data may be

attributed to several sources, the most noticeable of which are fluctuation in the number density of the sample entering the diffusion battery, unstable flow rate, and loss of particles through sampling ports during measurement. Some justifiable treatments were taken if necessary to correct the data before feeding them to the inversion scheme.

The retrieved size distributions in all cases are fairly broad, far from being monodisperse. This is partly due to the irregularities in the data and partly due to the non-uniqueness nature of the data inversion. In Fig. 14, the retrieved size distribution for 0.801 μm latex particles is shown as the dashed curve over a size range [0.01 μm , 10.0 μm]. The accuracy of the inversion, with $\lambda=0.1$, in 1000 cycles of iteration is $\bar{\delta}_1=1.5\%$. Accordingly, instead of taking the retrieved distributions as they are, further useful information may be extracted from them in the following way. Since the diffusion battery is an instrument to classify particles according to the magnitude of their diffusion coefficients, a mean diffusion coefficient calculated from the retrieved distribution has more physical significance than the size distribution itself, if the particle sample is known a priori to be monodisperse. From the mean diffusion coefficient, a corresponding mean diameter can be deduced. Since the diffusion coefficient is inversely proportional to the diameter, a mean particle diameter, \bar{d} , may be extracted from the retrieved distribution in the following way,

$$\bar{d} = \left[\sum_{k=1}^N w_k \frac{1}{d_k} f_{\text{retrieved}}(d_k) \right]^{-1}$$

The \bar{d} for the test particles used in the experiment are listed in Table 3. The agreement can be considered fair.

Table 3. Comparison of retrieved particle sizes with stated sizes of test aerosols.

<u>Test Aerosol</u>	<u>Stated Size</u>	<u>Retrieved</u>	<u>% Error</u>
	<u>(μm)</u>	<u>Mean Size (μm)</u>	
NaCl	0.26	0.31	+19
Latex	0.312	0.33	+6
Latex	0.46	0.44	-4
Latex	0.60	0.53	-12
Latex	0.801	0.74	-8

V. Conclusion

The new non-linear iterative inversion scheme developed in the paper has been established to work very well in analyzing data of the collimated hole structures diffusion battery. It has a relatively fast rate of convergence, good resolution, and is stable to as much as 5% random errors in the data. Furthermore, with this inversion scheme, the particle sizing capability of the diffusion battery can be extended up to 0.8 μm in diameter for a not too high flow rate. Since the commercially available screen-type diffusion battery is usually calibrated against the original collimated hole structures diffusion battery, the new inversion scheme presents a convenient means of analyzing data routinely obtained from the screen-type diffusion battery.

References

- [1] Sinclair, D., Am. Ind. Hygiene Ass. J., Nov., 729 (1972).
- [2] Sinclair, D. and Hoopes, G.S., Am. Ind. Hygiene Ass. J., Jan., 39 (1975).
- [3] Cheng, Y.S. and Yeh, H.C., J. Aerosol Sci. 11, 313 (1980).
- [4] Knutson, E.O., "Comparative measurements of New York City Aitken particles with a diffusional battery and an electrical aerosol analyzer," HASL Technical Memorandum 76-13 (1976).
- [5] Soderholm, S.C., J. Aerosol Sci. 10, 163 (1979).
- [6] Raabe, O.G., J. Aerosol Sci. 2, 289 (1971).
- [7] Raabe, O.G., Envir. Sci. Tech. 12, 1162 (1978).
- [8] Mercer, T.T. and Greene, T.D., J. Aerosol Sci. 5, 251 (1974).
- [9] Busigin, A., Van der Vooren, A.W., and Phillips, C.R., J. Aerosol Sci. 11, 359 (1980).
- [10] Wong, W.T. and Tang, I.N., "A non-linear iterative inversion technique for the Fredholm integral equation of the first kind," submitted to J. Comput. Phys.
- [11] Twomey, S., J. Franklin Inst. 279, 95 (1965).
- [12] Turchin, V.F., Kozlov, V.P., and Malkevich, M.S., Sov. Phys. Usp. 13, 681 (1971).
- [13] Deschamps, G.A. and Cabayan, H.S., IEEE Trans. Antennas and Propagation AP-20, 268 (1972).
- [14] Varah, J.M., SIAM Rev. 21, 100 (1979).
- [15] Twomey, S., "Introduction to the mathematics of inversion in remote sensing and indirect measurement," Elsevier Scientific Publishing Co., 1977.

- [16] Twomey, S., J. Comput. Phys. 18, 188 (1975).
- [17] Gormley, P.G. and Kennedy, M., Proc. Roy. Irish Acad. 52A, 163 (1949).
- [18] Thomas, J.W., Symp. Proc. Assessment of Airborne Radioactivity, p. 701, Intl. Atomic Energy Agency, Vienna (1967).
- [19] Sinclair, D., Countess, R.J., Liu, B.Y.H., and Pui, D.Y.H., presented at the 68th Annual Meeting of the Air Pollution Control Association, Boston, June 15-20, 1975.
- [20] Tang, I.N. and Munkelwitz, H.R., J. Aerosol Sci. 8, 321 (1977).

AD-A110 276

BROOKHAVEN NATIONAL LAB UPTON NY DEPT OF ENERGY AND --ETC F/G 13/2
SULFURIC ACID SPILL CHARACTERISTICS UNDER MARITIME ACCIDENT CON--ETC(U)
NOV 81 I N TANG, W T WONG, H R MUNKELWITZ MIPR-2-70099-7-75117A

USC6-D-73-81

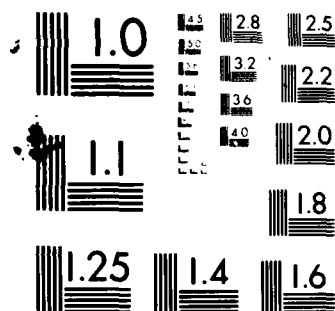
NL

UNCLASSIFIED

2 - 2
100%



END
DATE
FILMED
2 82
DTIC



MICROCOPY RESOLUTION TEST CHART
NATIONAL BUREAU OF STANDARDS-1963-A

Figure Captions

- Fig. 1. Test case 1.
- Fig. 2. Test case 2.
- Fig. 3. Test case 3.
- Fig. 4. Test case 4.
- Fig. 5. Test case 5.
- Fig. 6. Test case 6.
- Fig. 7. Test case 7. o retrieved distribution by Twomey's scheme
- Fig. 8. Test case 8.
- Fig. 9. Test case 9.
- Fig. 10. Test case 10.
- Fig. 11. Inversion of parallel-plant diffusion battery data. — assumed gamma distribution; ---- retrieved distribution by present scheme using parallel-plate diffusion battery data; o retrieved distribution by present scheme using collimated hole structures diffusion battery data.
- Fig. 12. Experimental arrangement for generating samples and measuring penetration data of Latex and sodium chloride particles.
- Fig. 13. Normalized penetration data for several Latex particles. — theoretical fractional penetration.
- Fig. 14. Retrieved distribution (----) by present scheme from measured penetration data of 0.801 μm Latex particle.

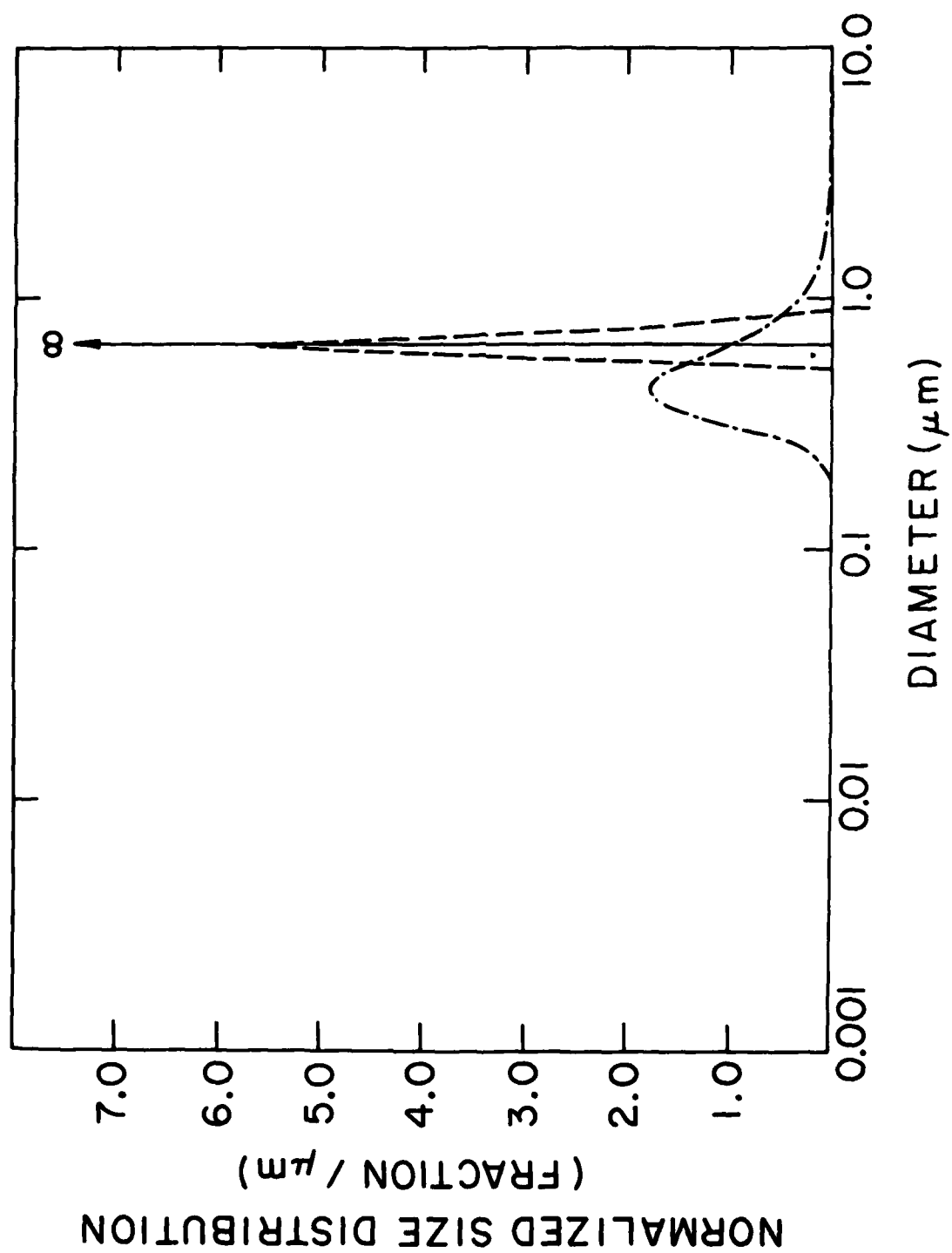


Fig. 1

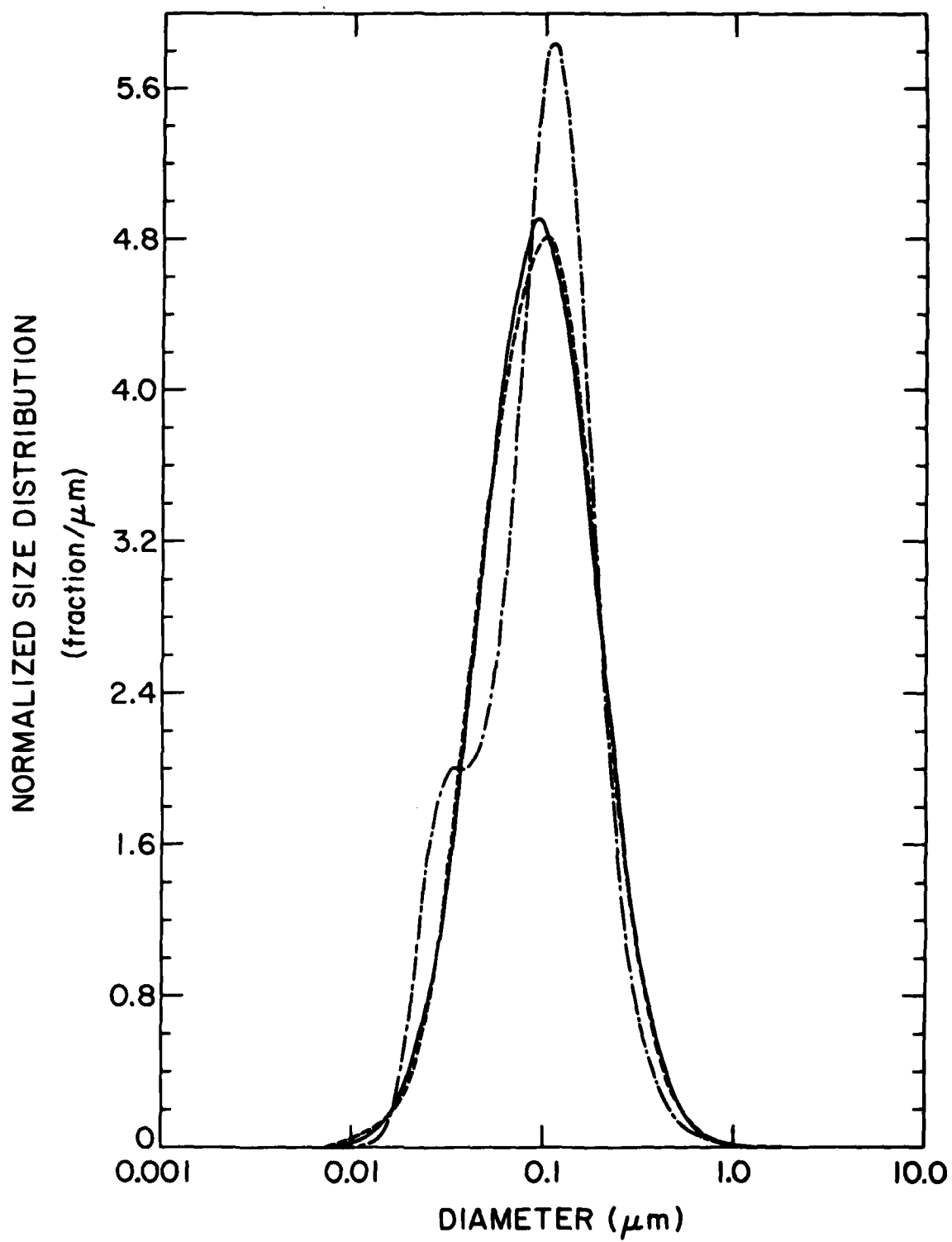


Fig. 2

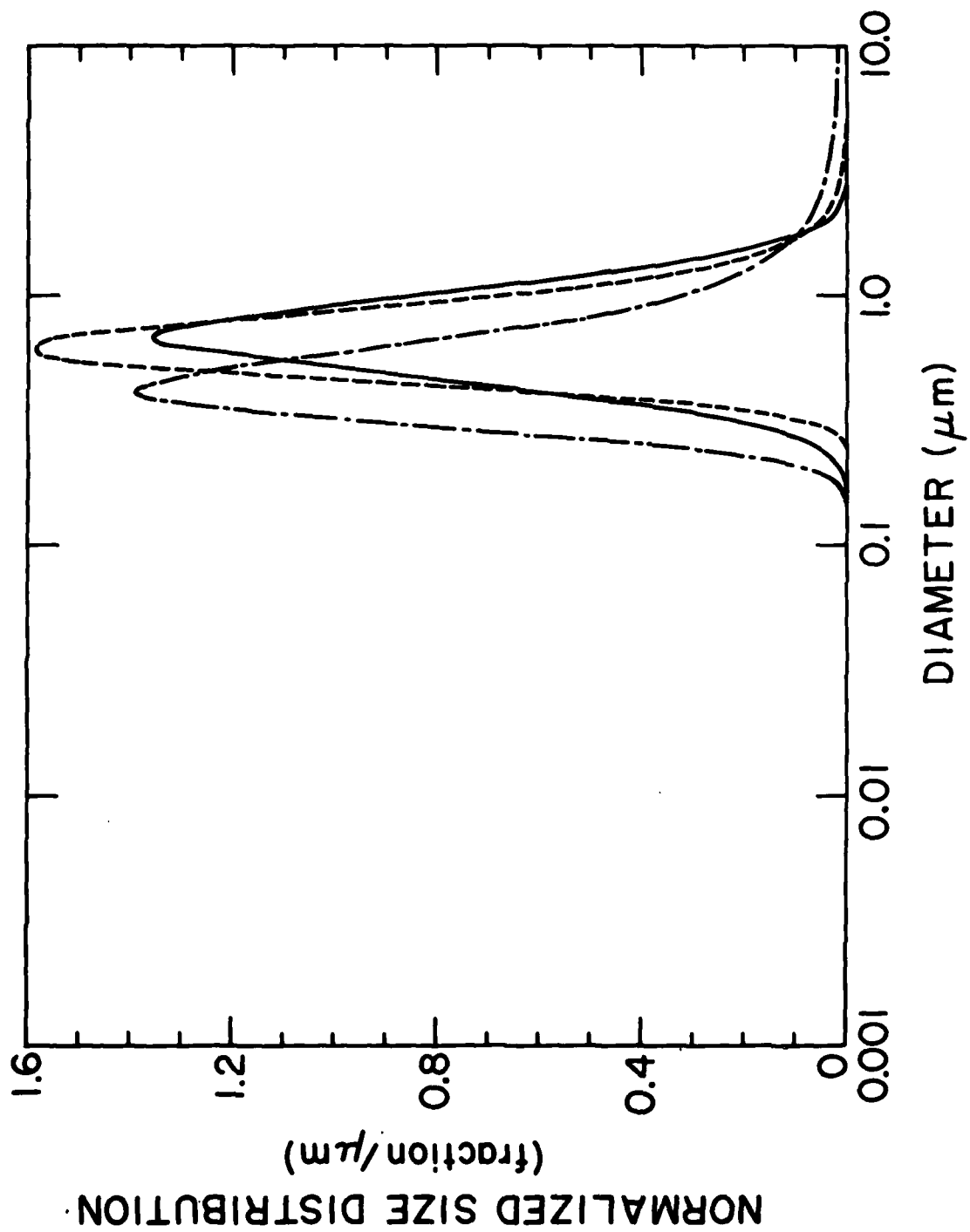


Fig. 3

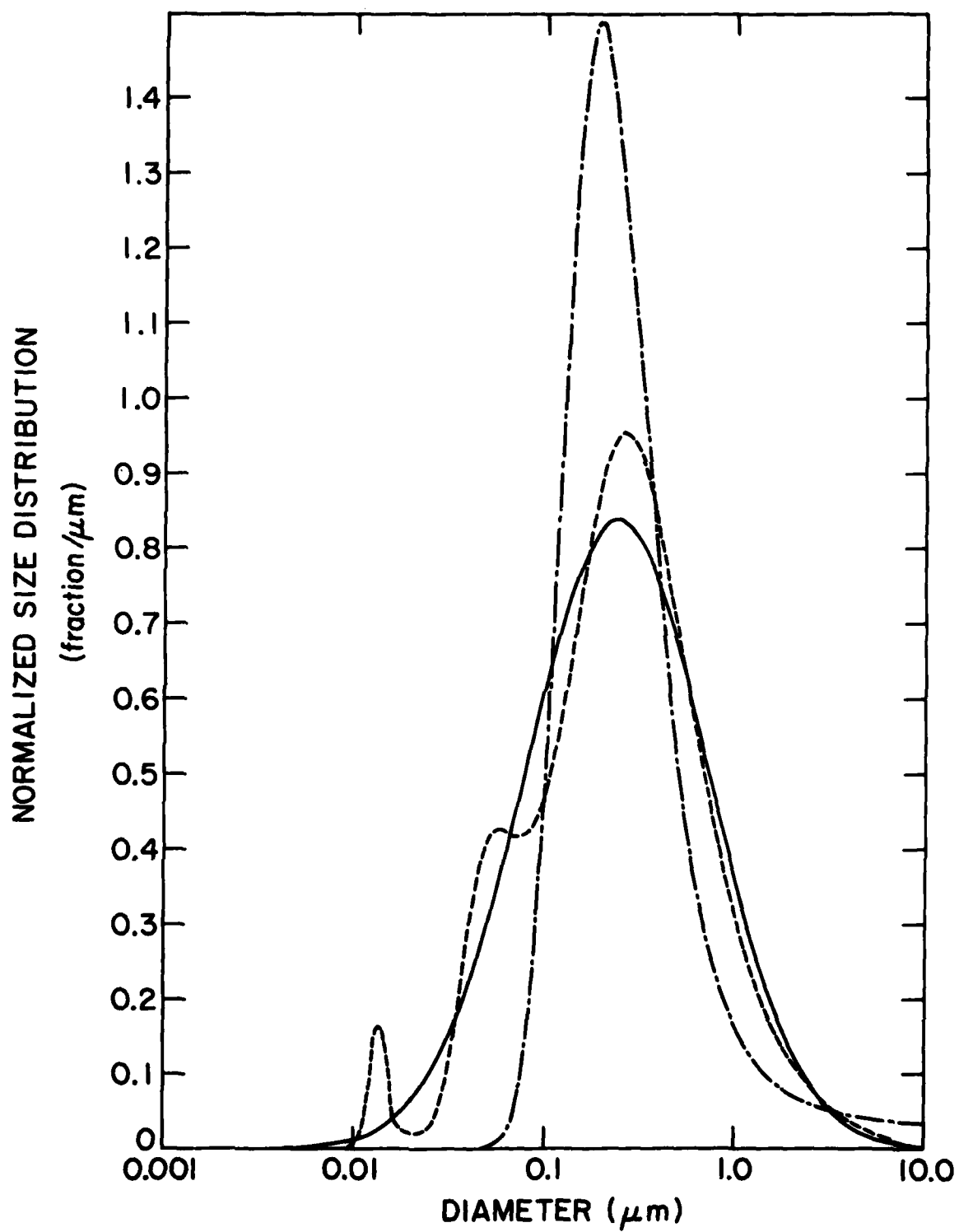


Fig. 4

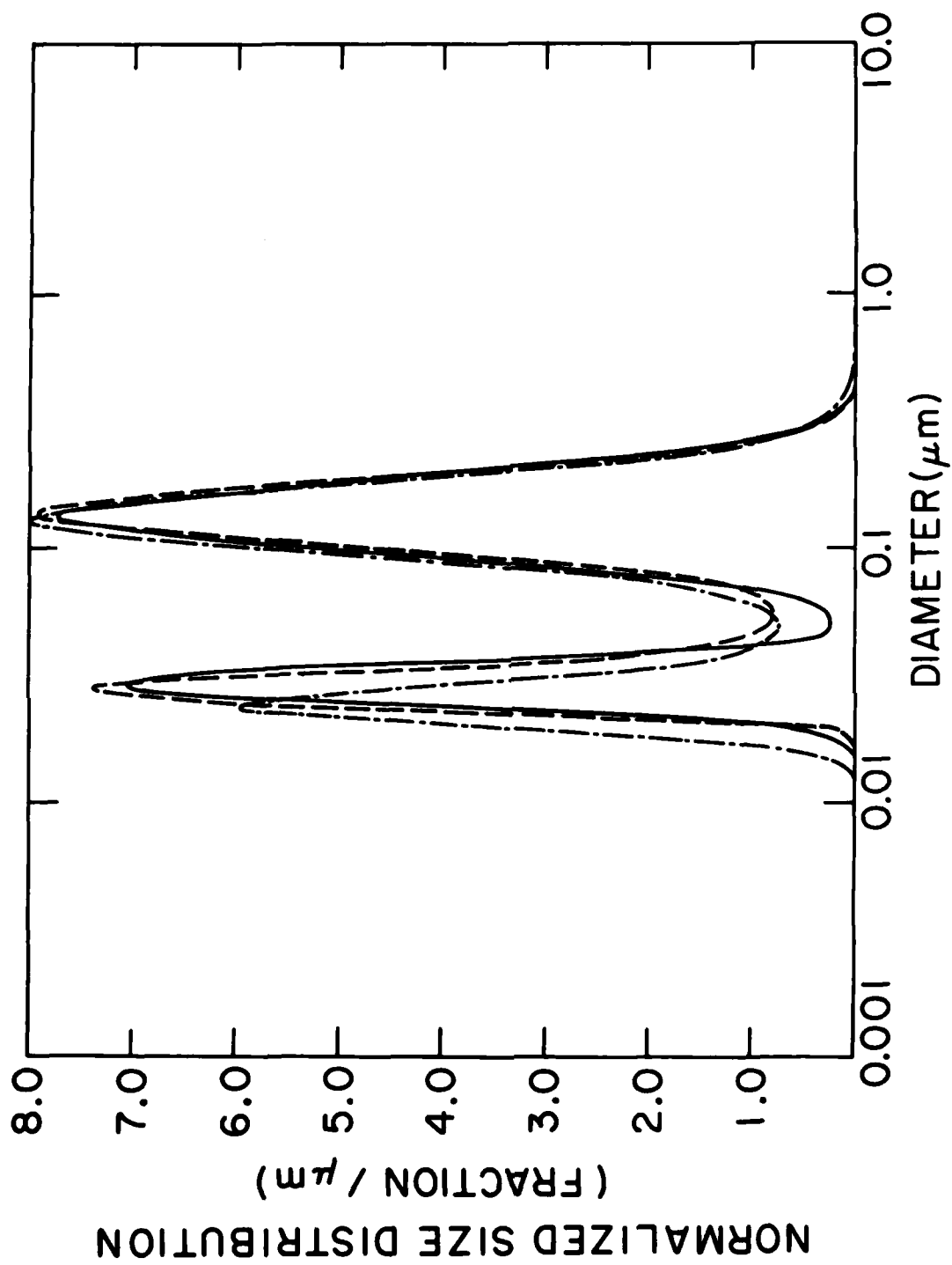


Fig. 5

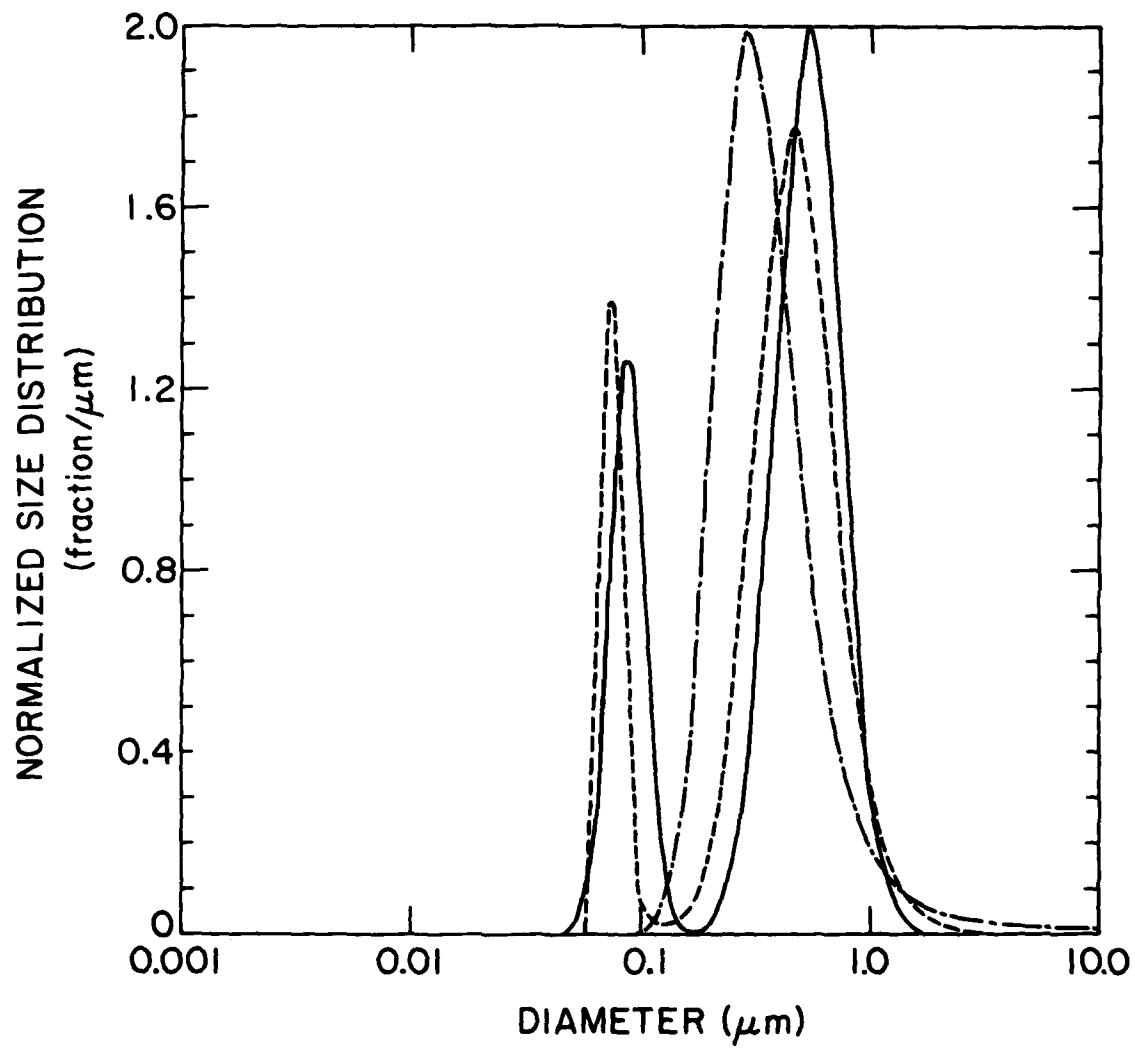


Fig. 6

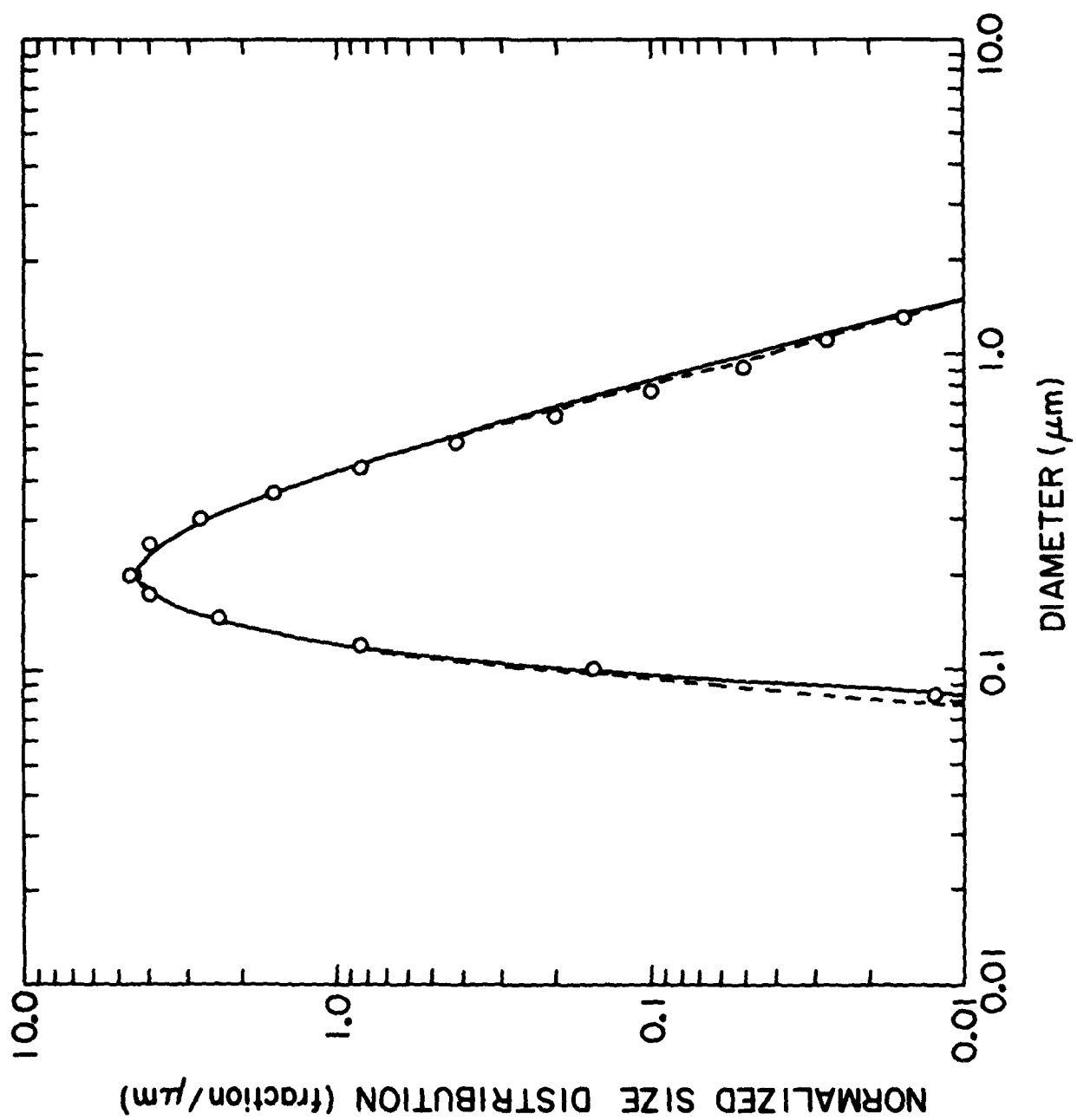


Fig. 7

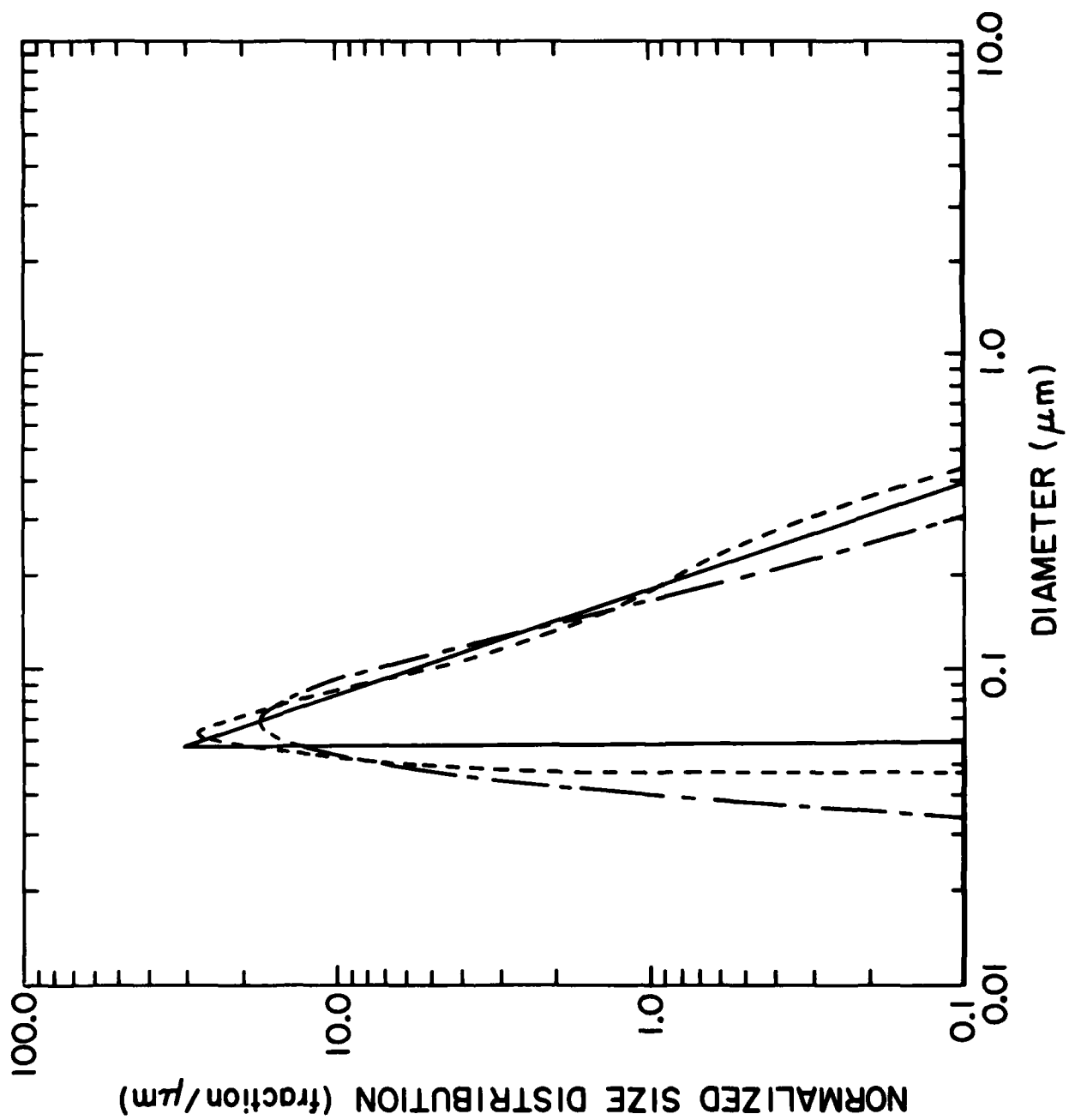


Fig. 8

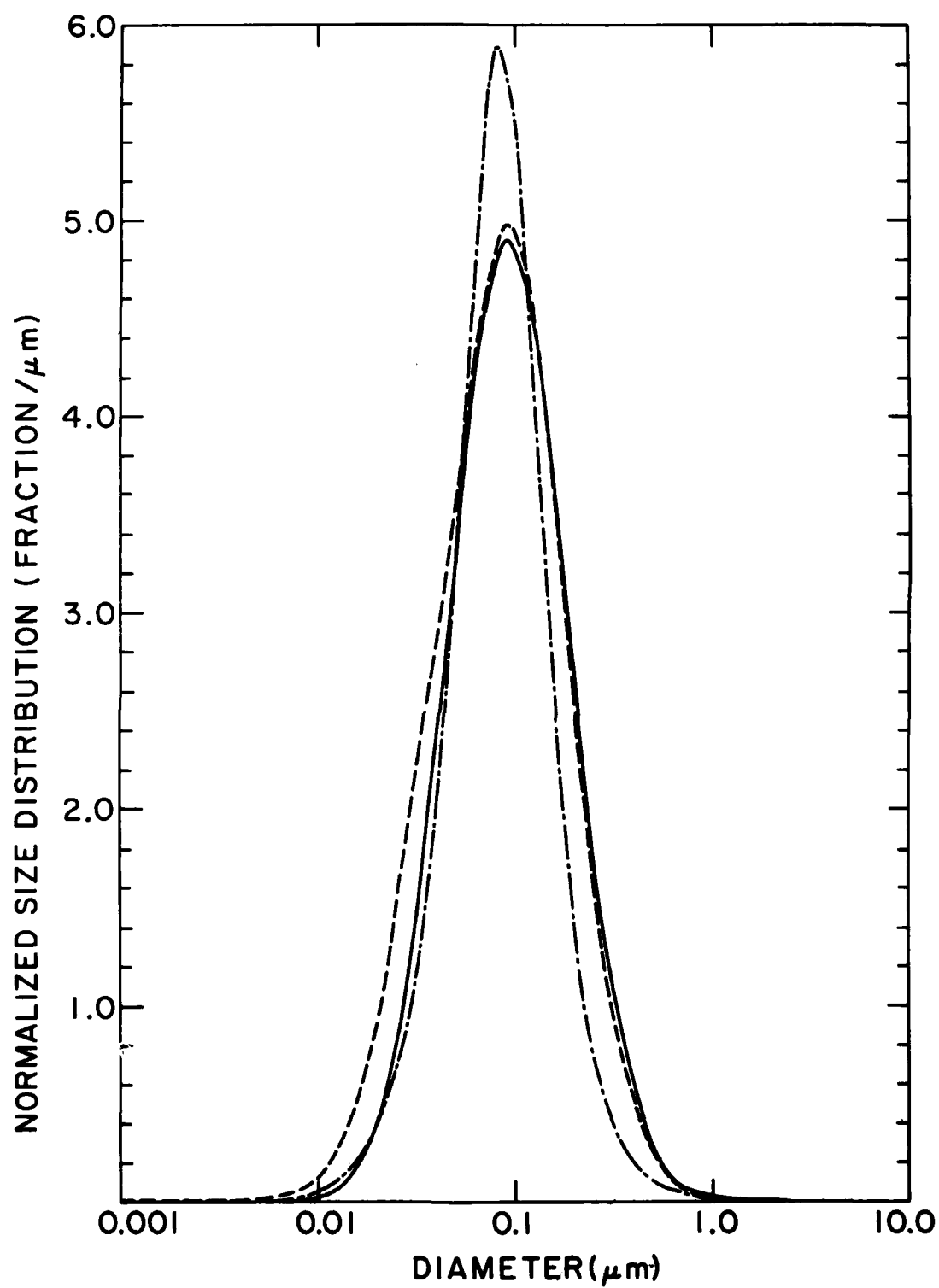


Fig. 9

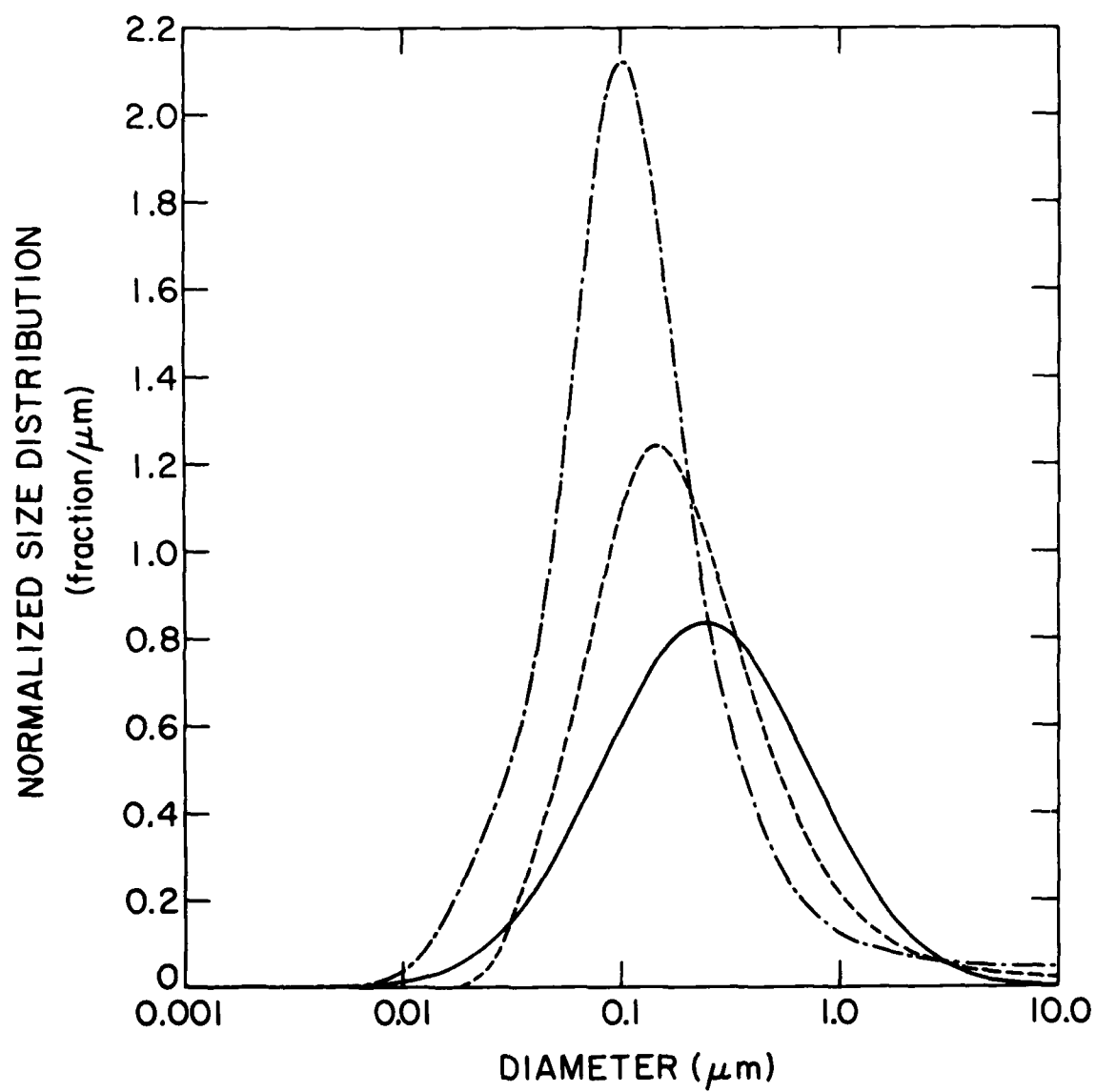


Fig. 10

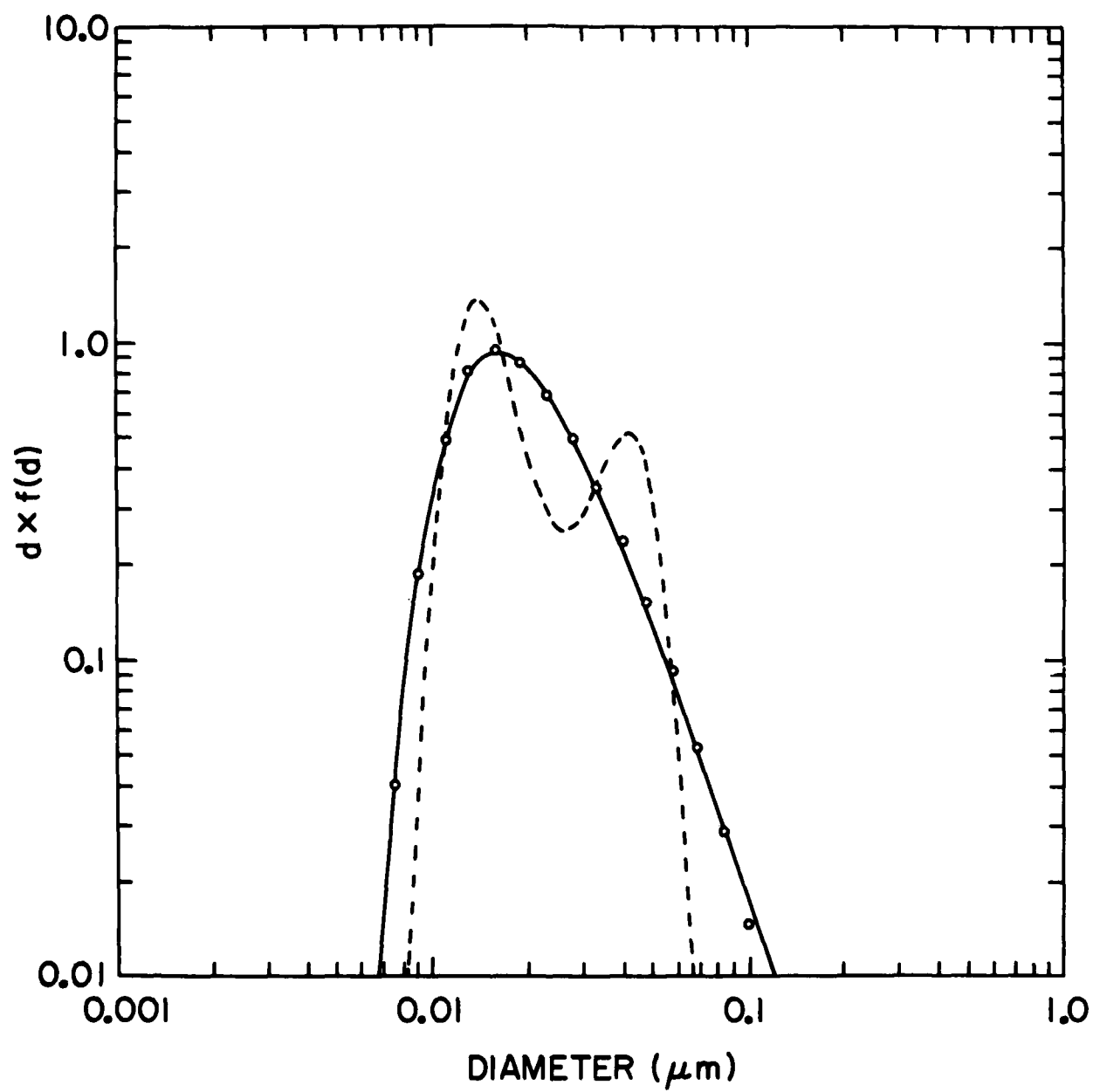
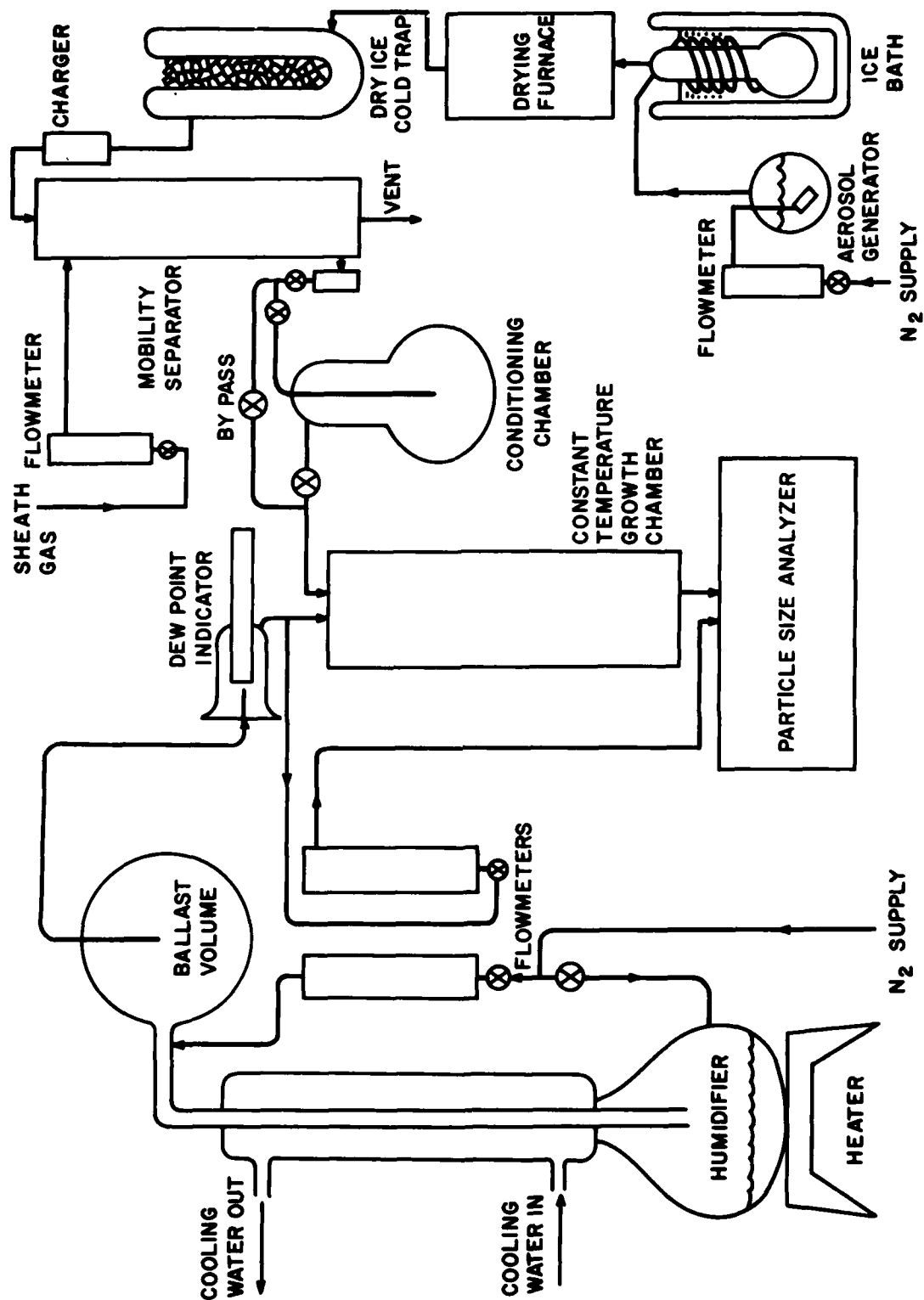


Fig. 11



NH₄HSO₄-AEROSOL GROWTH APPARATUS

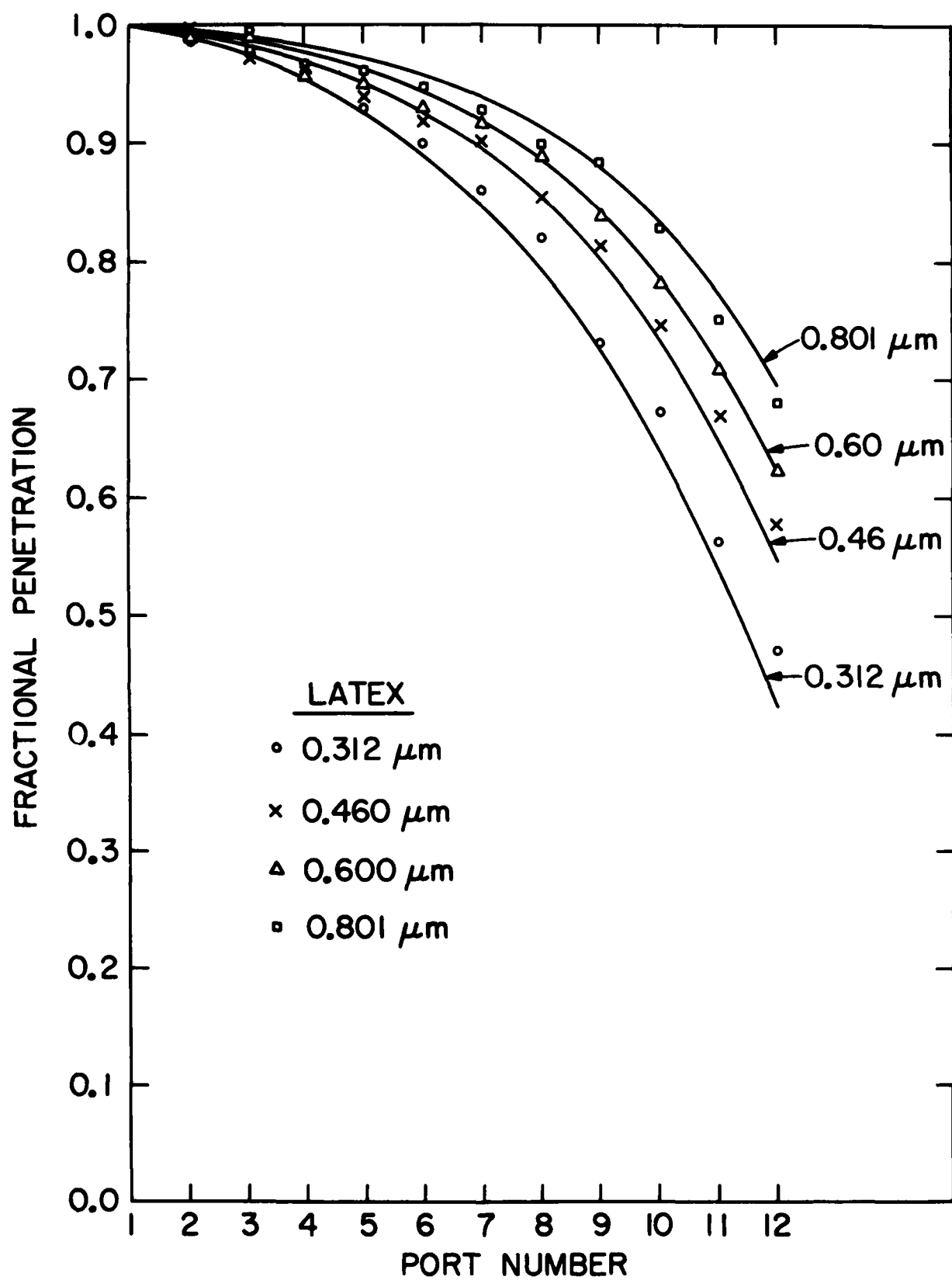
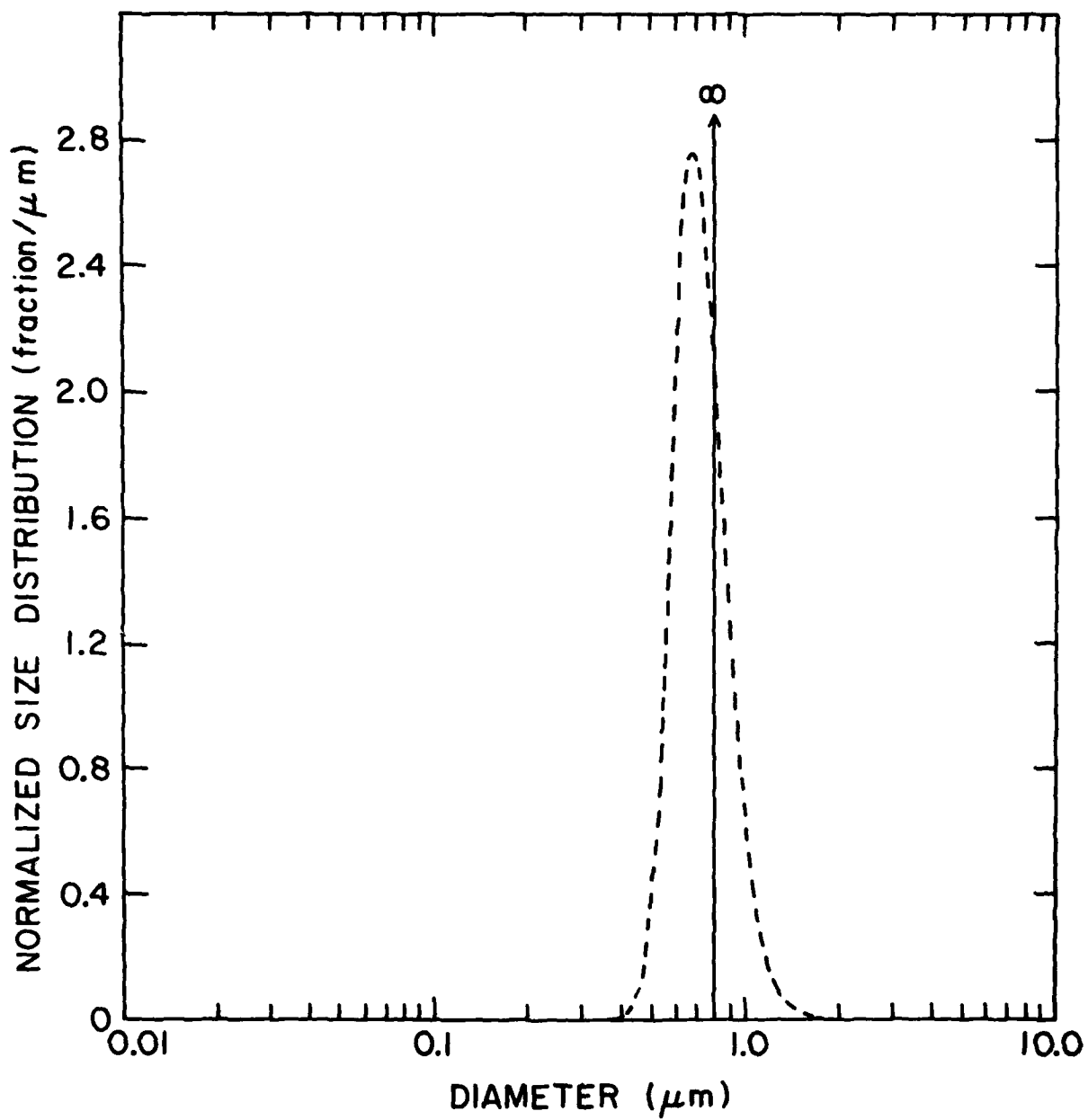


Fig. 13



U.S. GOVERNMENT PRINTING OFFICE: 1962-361-426/1479

Fig. 14